

GOBLITS TO OMG: 3D FABRICATION TECHNIQUES FOR AN OPTO-MECHANICAL GYROSCOPE

A Dissertation

Presented to the Faculty of the Graduate School
of Cornell University

in Partial Fulfillment of the Requirements for the Degree of
Doctor of Philosophy

by

Laura Fegely

January 2014

© 2014 Laura Fegely
ALL RIGHTS RESERVED

GOBLITS TO OMG: 3D FABRICATION TECHNIQUES FOR AN
OPTO-MECHANICAL GYROSCOPE

Laura Fegely, Ph.D.

Cornell University 2014

The scope of this dissertation is to discuss the concept and design considerations of a micro-scale mass manufacturable opto-mechanical gyroscope, as well as the considerable fabrication challenges faced in creating a mass manufacturable hemispherical shell resonator that meets all required design constraints. Intensive studies of HNA isotropic etching of Si, and alternative masking schemes were undertaken to reduce anisotropy and roughness. Dopant Enhanced Oxidation schemes are discussed, and toroidal-lip silicon oxide devices for improved optical quality factor are fabricated. Optical sensing of mechanical resonances is seen in air, and verified with Laser Doppler Vibrometry (LDV).

BIOGRAPHICAL SKETCH

Laura Fegely received her bachelor's degree in electrical engineering from Drexel University in 2008. With experience in research from internships at Oak Ridge National Laboratory, and Tohoku University in Sendai, Japan, as well as industrial internships at Dupont deNemours & Co and a small design firm, she joined the OxideMEMS group at Cornell University as an M.S./Ph.D. student.

At Cornell she received the Jacobs Fellowship, and was subsequently supported on project grants through the Defense Advanced Research Projects Agency (DARPA). She also worked as a teaching assistant for the Electrical and Computer Engineering Department, and interned as a Product Engineer in the Consumer Gyroscope group at Analog Devices in Wilmington, MA, where she will continue working after graduation.

She presented work at the 16th International Conference on Solid-State Sensors, Actuators, and Microsystems (Transducers '11), and will be submitting work for the 2014 Hilton Head Solid-State Sensors, Actuators and Microsystems Workshop. She is also in the process of writing a journal submission with the intention of submitting it for review for the Journal of Microelectromechanical Systems (JMEMS).

Dr. Fegely's dissertation, OMG: An Opto-Mechanical Gyroscope, was supervised by Dr. Sunil Bhave.

To my dad, who always took the time to show an interest in my work, and my mom, who preferred to take an interest in me. I couldn't have done it without either of you.

ACKNOWLEDGEMENTS

I'd like to take this space to acknowledge the help and support of several people. First and foremost is my advisor, Prof. Sunil Bhave, who was always there to motivate, support, inspire, and edit conference abstract submissions at 5 in the morning. I've gotten help from all the members of the OxideMEMS Lab research group, but am especially indebted to Ajay Bhat and David Hutchison, both of whom have contributed quite substantially to my research efforts. Erdal Yilmaz, a Ph.D. student working with Prof. David Bindel in the CS department here at Cornell has also been a huge help and great sounding board for various ideas. CNF staff have provided amazing tool support services over the years, in particular Noah Clay, who was even willing to help out at 1am on a Sunday morning before a deadline. Seriously. Thanks.

Analog Devices Incorporated not only gave me an internship, and eventually a job, but also allowed use of their own optical systems for device measurement verification and access to my advisor while he was on sabbatical.

And last, but certainly not least, this research could not have been accomplished without the funding of DARPA's MTO μ PNT MRIG program. (Defense Advanced Research Projects Agency's - Microsystems Technology Office - Micro-Technology for Positioning, Navigation and Timing - Microscale Rate Integrating Gyroscope Program). Without them we couldn't have afforded the paper necessary to expand those abbreviations to their full form.

On a more personal note, I really couldn't have finished my dissertation work without the support of great friends and family - thank you for being understanding through all the stress, work avoidance, deadline cramming, and complaining. Mom, Dad, Mike, Erin, Akina, Ariel, Albert, Mike, Marsha, Dan - you guys keep me sane.

And God's help has been pretty much the basis of my life.

TABLE OF CONTENTS

Biographical Sketch	iii
Dedication	iv
Acknowledgements	v
Table of Contents	vi
List of Tables	viii
List of Figures	ix
1 Motivation	1
1.1 Gyroscopes	1
1.1.1 Mechanical Gyroscopes	5
1.1.2 Optical Gyroscopes	6
1.1.3 Vibratory Gyroscopes	9
1.2 Target Device	28
1.2.1 GOBLiT	35
I Fabrication Considerations	42
2 Bulk Etching	43
2.1 HNA Etching Design of Experiment	49
2.1.1 Results	51
2.1.2 Masking Issues	56
2.2 Conclusion	59
3 Etch Masking	60
3.1 Dynamic Masking	60
3.1.1 Results	64
3.2 Compensation Masking	66
3.2.1 Orientation Alignment Marks	66
3.2.2 Results	68
3.3 Conclusion	70
4 Device Fabrication	71
4.1 Dopant Enhanced Oxidation Structures - DEOS	74
4.2 Toroidal-Lip GOBLiT	77
4.3 Conclusion	79
II Device Considerations	81
5 Simulation	82
5.1 Mechanical Modeling	82
5.1.1 Basic Shape	82

5.1.2	Toroidal Lip Shape	91
5.2	Optical Modeling	94
5.3	Conclusion	96
6	Experimental Results	97
6.1	Optical Transmission	97
6.2	Pump-probe	101
6.3	LDV	105
6.3.1	Air vs. Vacuum	106
6.3.2	2D Maps	109
6.4	Opto-Mechanical Pick-off	109
6.5	Conclusion	114
7	Future Work	116
7.1	Fabrication Work	116
7.2	Device Work	117
	Appendices	118
	A Coriolis Force Derivation	118
	B Optical Spring Effect	121
	Bibliography	128

LIST OF TABLES

1.1	PSD and Allan Deviation of Various Noise Sources	25
1.2	Expected HRG Scaling Performance	36
6.1	Summary of Pump-Probe Data	104

LIST OF FIGURES

1.1	Image of a typical gimbal-mounted gyroscope.	2
1.2	Free-body diagram for Foucault’s Pendulum.	3
1.3	Path of a Foucault pendulum	4
1.4	Orientation of Foucault pendulum on Earth	4
1.5	Diagram of RLG	7
1.6	Diagram explaining Sagnac effect	7
1.7	Diagram of FOG	9
1.8	Diagram of Basic Resonance Model	10
1.9	Spectral Analysis of Basic Resonance Model	11
1.10	Whole Angle vs. Rate Gyroscopes	12
1.11	Working principle of a Vibratory Gyro	13
1.12	Frequency Spectra of non-Mode Matched Spectra	19
1.13	Random Walk of Integrated Signals	20
1.14	Allan Deviation of a Rate Gyro	24
1.15	Hemispherical Resonator Gyro	26
1.16	Rotation Response of Wineglass Modes	27
1.17	Target Structure Design Flow	29
1.18	Radiation Pressure and Optical Gradient Forces	33
1.19	The GOBLiT	35
1.20	Diagram for Opto-Mechanical Modeling	37
1.21	Optical Spectrum for Various Q_{opt}	39
1.22	Optical Spectrum for Various Q_{mech}	40
1.23	Basic GOBLiT Process Flow	41
2.1	Anisotropy Archetypes of Isotropic Etches	44
2.2	SEM of HNA Anisotropy	45
2.3	SEM of XeF_2 Etched Mold	46
2.4	Anisotropy of HNA etching	47
2.5	SEMs of HNA Profiles	48
2.6	HNA Etch Chemical Ratios	50
2.7	Anisotropy Vs. Chemical Ratio	52
2.8	Anisotropy Vs. Etched Radius	52
2.9	Anisotropy Vs. Normalized Etched Radius	53
2.10	Etched Radius Vs. Temperature	54
2.11	SEMs of Etch Roughness	55
2.12	Nitride Cracking over Wafer	56
2.13	SEM of Large Radius Etch Profile	56
2.14	Mask Trench Layout for Relieving Nitride Cracking	58
2.15	Graph of Nitride Selectivity	58
3.1	Progression of Dynamic Masking Etch	61
3.2	Point Approximation for Initial Topology	63

3.3	Various Release Ring Layouts	64
3.4	SEMs Comparing Dynamic and Regular Masking	65
3.5	SEM of Dynamic Masking for 2 Minute Etch	65
3.6	Initial Designs for Compensation Masking	66
3.7	Diagram of Orientation Alignment Marks	67
3.8	Orientation Alignment Marks after KOH Etch	67
3.9	Resulting Compensation Masking Etches	69
3.10	Resulting Compensation Masking Etches: Final Iteration	69
4.1	SEM of First GOBLiT	72
4.2	SEM of Cracked Nitride GOBLiT	72
4.3	Optical Qs for BOE Etched Oxide GOBLiTs	73
4.4	DEO Simulation of Oxide Thickness Variations	75
4.5	DEO Simulation of 2 Stage Doping	76
4.6	DEOS Process Flow	76
4.7	Process Flow for Toroidal-Lip GOBLiTs	78
4.8	SEM of Toroidal-Lip GOBLiT	79
5.1	COMSOL: Basic HSR, $m=2$	84
5.2	COMSOL: Basic HSR, $m=3$	85
5.3	Eigenfrequency Differences between Theory and FEM vs. Radius	85
5.4	Eigenfrequency Scaled Differences vs. Radius	86
5.5	COMSOL Simulated Wineglass Modes with Lip	87
5.6	Effect of Lip Width on Mechanical Frequency	87
5.7	Effect of Lip Thickness on Mechanical Frequency	88
5.8	Log Plot of Frequency over Varied Dimensions	88
5.9	Log Plot of Frequency over Varied Dimension Ratio	89
5.10	SEM of Toroidal Lip GOBLiT with Dimensions	92
5.11	Simulated Spectrum of Toroidal Lip GOBLiT	92
5.12	Simulated Spectrum of TorLiT for Reduced Lip Width	93
5.13	Simulated Spectrum of TorLiT for Reduced Stem Radius	93
5.14	Simulated Optical Mode Cross-sections for Various Radii and Lip Thickness	94
5.15	Simulated Optical Mode Spreading into Bowl	95
5.16	Index Matching for Taper and Waveguide	95
6.1	Setup for Optical Transmission Testing	97
6.2	Diagram of Tapered Fiber	98
6.3	Picture of a Pulled Taper Fiber	98
6.4	High Q Measurement of Nitride Device	99
6.5	High Q Measurement of Oxide GOBLiT from Under Lip	100
6.6	Optical Q Measurement of Toroidal Lip GOBLiT	101
6.7	Diagram of Setup for Pump-Probe Measurements	102
6.8	Pump-Probe Measurement of $M = 2$ Wineglass Mode	103

6.9	Pump-Probe Measurement of $M = 3$ Wineglass Mode	103
6.10	Diagram of LDV Setup	106
6.11	LDV Measurements of Oxide GOBLiT in Vacuum and Air	107
6.12	LDV Measurements of Same Interrogation Point in Vacuum and Air	108
6.13	SEM of SF_6 Etched Device Roughness	108
6.14	LDV Spectrum for Toroidal Lipped GOBLiT	109
6.15	2D LDV Scan of $M = 2$ Wineglass Mode for TorLiT	110
6.16	2D LDV Scan of $M = 2$ Wineglass Mode for TorLiT	110
6.17	2D LDV Scan of $M = 3$ Lip Flapping Mode for TorLiT	111
6.18	2D LDV Scan of $M = 4$ Lip Flapping Mode for TorLiT	111
6.19	Schematic of Setup for Opto-Mechanical Measurements	112
6.20	Opto-Mechanical for TorLiT Structure	113
6.21	Comparison of Mechanical Measurements for TorLiT Structure . .	113
A.1	A point defined in rotating and inertial frames of reference	118

CHAPTER 1

MOTIVATION

In the following chapter I will introduce some of the basic concepts necessary to understand the motivation and design of an opto-mechanical gyroscope.

1.1 Gyroscopes

Put simply, a gyroscope is a device that measures how much rotation the device it is mounted on has experienced. Historically, gyroscopes consisted of large, gimbal-mounted rotors which made use of angular momentum to allow them to maintain their orientation without heeding the rotation of the system they were mounted on. The measurement of the system could then be determined by the movement of the gimbals with respect to the rotor. In fact, this is the method that French scientist Jean Bernard Leon Foucault used in 1852 to confirm the 24-hour period of rotation for the earth, and it was Foucault who coined the term gyroscope.

However, gyroscopes of this type require that there be no external torque (i.e. frictionless bearings) in order for angular momentum to be conserved. For large rotors, such an approximation can be used, but eventually the friction losses will win out and the rotor will be unable to maintain its orientation. Foucault ran into this issue while attempting to measure the rotation of the Earth with his gyroscope, and as an alternate means of making this measurement, came up with what is now known as the Foucault pendulum.

This is merely a large mass placed on the end of a very long string or wire. If the mass is set swinging, conservation of linear momentum will keep the pendulum

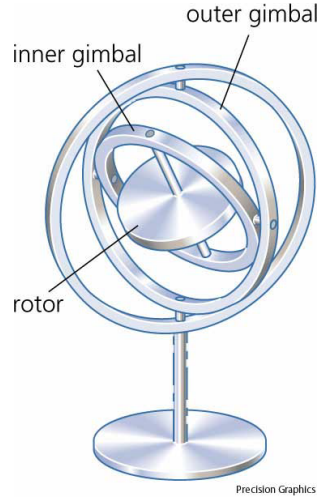


Figure 1.1: Image of a typical gimbal-mounted gyroscope. Taken from <http://www.answers.com/gimbal>

swinging in the same plane it started in while the earth rotates underneath it. Intuitively, this concept makes sense. However, the mathematics can become quite complicated due to the coordinate system of the earth moving in relation to the pendulum. Systems of this nature are more easily described mathematically by using fictitious forces. Fictitious forces are those forces which are defined to explain the observed behavior of an object in a secondary frame of reference from the point of view of the first. In particular, we can use the Coriolis force:

$$\mathbf{F}_c = -2\boldsymbol{\Omega} \times m\mathbf{v} \quad (1.1)$$

This force describes the apparent force seen by an observer on a reference frame undergoing a rotation $\boldsymbol{\Omega}$ on an object moving with linear momentum $m\mathbf{v}$. A more in depth derivation of the Coriolis force can be found in Appendix A.

Using the Coriolis force, the system equation for the Foucault pendulum can be written:

$$m\ddot{\mathbf{r}} = m\mathbf{g} + \mathbf{T} - 2m\boldsymbol{\Omega} \times \dot{\mathbf{r}} \quad (1.2)$$

where m is approximated as the large mass (the mass of the string is assumed

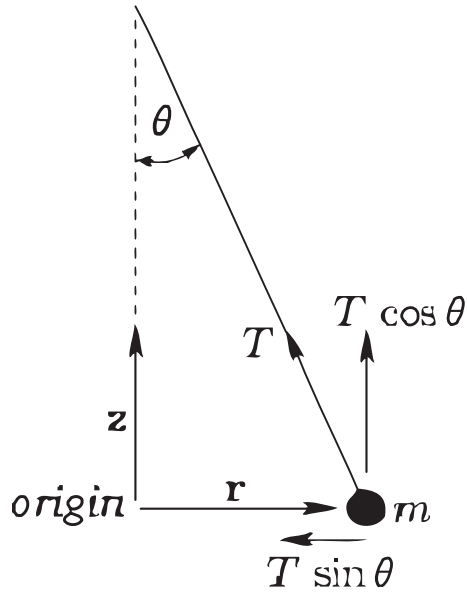


Figure 1.2: Free-body diagram for Foucault's Pendulum.

negligible), \mathbf{T} is the vector giving the tension due to the string, and \mathbf{r} is the vector giving the position of the (center) of the mass, with coordinates as shown in Fig. 1.2.

We see from Eq. 1.2 that if there is a rotation counterclockwise about the \mathbf{z} axis, a Coriolis force will be seen which is directed out of the page when \mathbf{r} is directed to the right and into the page when \mathbf{r} is directed to the left. For a system in which the rotation speed is only slightly slower than the cycle of the pendulum's swing, the path traced out by the mass, when viewed from above, would be something like Fig. 1.3 [1].

Of course the period of rotation for the Earth is much longer than the period of the pendulum's swing for any realistically sized pendulum. Additionally, we must remember that, unless we are at the North or South poles the axes of the gravity vector and the rotation vector for the Earth's rotation do not actually align, so the rotation through which the pendulum will precess in one day will not be 360° ,

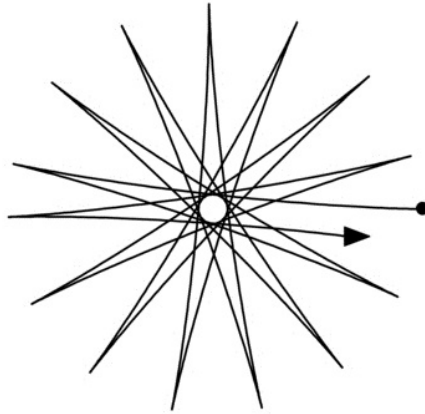


Figure 1.3: Path of a Foucault pendulum for a system rotating counterclockwise, where the period of rotation is longer than period of pendulum swing. The mass is released from $(1,0)$, shown by the dot. Reprinted from [1].

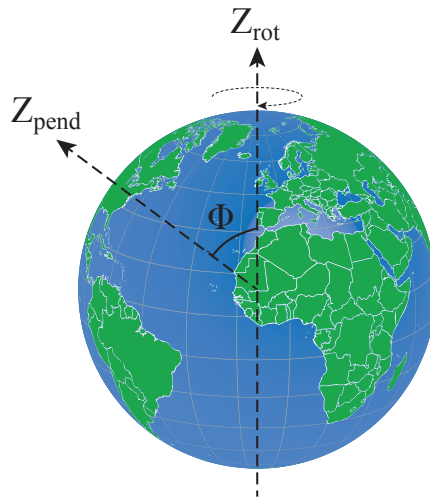


Figure 1.4: Depending on the latitude of the pendulum, it may not precess through 360° in one day, due to gravity and the axis of rotation not being coaxial.

but instead $360^\circ \times \cos \Phi$, as defined in Fig. 1.4.

The Foucault pendulum is a fascinating experiment in basic physics, but as a gyroscope it is rather pointless: it would be almost impossible to measure rotation in any system in which the gravity vector does not stay fixed with respect to the axis of rotation. So what are some realistic gyroscope structures?

1.1.1 Mechanical Gyroscopes

As mentioned previously, gyroscopes of this type use angular momentum as the basis for measuring rotation. There are then two ways to measure the rotation: (1) by allowing the rotor to move freely and measure the rotation through the relative position of the rotor to the system, or (2) to constrain, or ‘strapdown’, the rotor to move with the rotating object and measure the torque applied to the rotor to achieve this.

In the second case, the gyroscope is free to move in the two orthogonal axes perpendicular to the axis of rotation. Then, a rotation about one of these axes (the ‘input’ axis) will result in a torque in the other (sense axis), due to the cross product shown below:

$$\tau = \frac{d\mathbf{L}}{dt} = \frac{d(I\boldsymbol{\Omega}_{rot})}{dt} = \boldsymbol{\Omega}_{input} \times \mathbf{L} \quad (1.3)$$

τ is the torque, \mathbf{L} is the angular momentum, I is the moment of inertia, $\boldsymbol{\Omega}_{rot}$ the angular velocity of the rotor and $\boldsymbol{\Omega}_{input}$ is the input rotation. Since the axes of \mathbf{L} and $\boldsymbol{\Omega}_{input}$ are orthogonal, the τ produced is seen on the sense axis. Then the movement of the sense axis is measured, and a signal is sent to a motor in the input axis to apply a counteracting torque to the input to cancel the precession. Since

torque is proportional to angular acceleration, by applying a known torque over a known time interval, the angular rate of the input rotation can be found. From that point, the rate must be integrated to find the actual rotation experienced by the system.

These type of gyroscopes can be quite accurate, and aren't as sensitive to shock or vibration as other gyroscopes we will look at, but they simply don't scale down in size. As size is reduced, angular momentum reduces much faster than the friction forces in the bearings, and the actual machining of such a system would be an art form.

1.1.2 Optical Gyroscopes

In addition to the mechanical phenomena of angular momentum or Coriolis force, there is an optical effect called the Sagnac effect which has been used to make optical gyroscopes. In a Sagnac effect based gyro, a coherent light beam is split to propagate in opposite directions along a path that then loops back to the splitter, where both light signals are sent to a detector. If the system is undergoing a rotation, a phase difference between the two signals will result in interference fringes seen at the detector. Such a system is shown in Fig. 1.5.

This phenomena is easiest to understand by looking at a circular path as shown in Fig. 1.6. For a system undergoing a rotation Ω_{rot} , in the time that it takes the light to travel around the loop and back to the beam splitter, the beam splitter itself will have moved a distance ΔL . The light that is traveling in the same direction as the rotation will see the beam splitter move away, and will therefore take a longer time to return. Similarly, the light traveling in the opposite direction

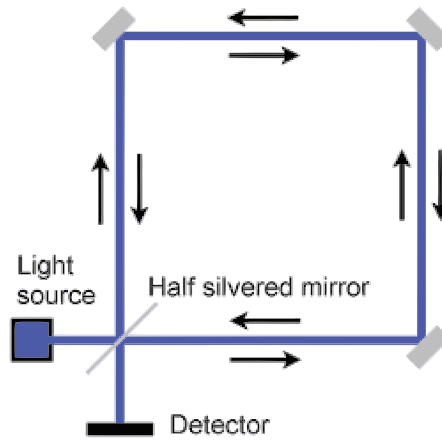


Figure 1.5: Diagram of a Ring Laser Gyroscope, which makes use of the Sagnac effect to determine rotation.

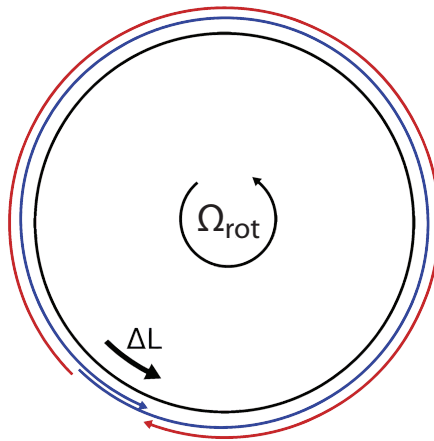


Figure 1.6: Diagram explaining Sagnac effect. Ω_{rot} is the rotation rate of the system, ΔL the arclength traveled by the beam splitter in the time it takes for the light to travel the length of the loop.

will take less time to return. For a circular loop of radius R :

$$t_{ccw} = \frac{2\pi R + \Delta L}{c} \quad (1.4a)$$

$$t_{cw} = \frac{2\pi R - \Delta L}{c} \quad (1.4b)$$

where ΔL is defined as $R\Omega_{rot}t_{ccw}$ for Eq. 1.4a and $R\Omega_{rot}t_{cw}$ for Eq. 1.4b. Substituting these values and solving for t_{ccw} and t_{cw} , we can find the time difference between the arrivals of each light wave as:

$$\Delta t_{total} = t_{ccw} - t_{cw} = \frac{4\pi R^2 \Omega_{rot}}{c^2 - R^2 \Omega_{rot}^2} \quad (1.5)$$

Since, for most cases, the tangential speed of the beam splitter as it rotates is much smaller than the speed of light ($R\Omega_{rot} \ll c$), this is reduced to:

$$\Delta t_{total} = \frac{4\pi R^2 \Omega_{rot}}{c^2} = \frac{4A\Omega_{rot}}{c^2} \quad (1.6)$$

This time difference will result in a phase shift which will be shown as interference fringes at the detector.

$$\Delta p = \frac{2\pi c \Delta t_{total}}{\lambda} = \frac{8\pi c A \Omega_{rot}}{c^2 \lambda} \quad (1.7)$$

where λ is the wavelength of the light.

As shown in Fig. 1.5, some implementations of optical gyros use mirrors and free space optics in their design. However, these Ring Laser gyroscopes, or RLGs, tend to be expensive, heavy, require precision machining and have high power consumption.

Alternate designs using optical fiber for the optical path, such as the Fiber Optical Gyroscope (FOG) shown in Fig. 1.7, are lower cost, lighter, last longer, can be made more compact, and digital forms are even able to increase the dynamic range and improve scale factor corrections. However, increasing sensitivity in these

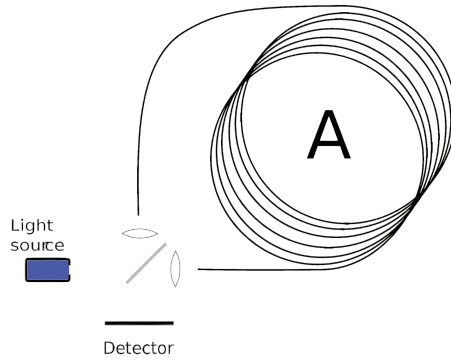


Figure 1.7: Diagram of a Fiber Optic Gyroscope. The gyroscope can easily be made more sensitive by adding more length to the path in the form of more coils of fiber. Effectively, $A = N * A$ in Eq. 1.6, where N is the number of loops.

gyros requires longer cavities, which are by nature more sensitive to temperature variation and vibration, and even the best FOGs are several orders of magnitude behind the top RLGs in performance. From the point of view of integration with electronics, however, these gyros simply cannot be made small enough while retaining the necessary path length, nevermind the required additional light source and detector.

1.1.3 Vibratory Gyroscopes

The term vibratory gyroscope refers to those gyroscopes which make use of a vibrating body to generate Coriolis force and measure rotation. Since the mass of the gyroscope must have some linear velocity for the Coriolis force to be generated, the easiest way to achieve this is to set the mass vibrating. To understand vibratory gyroscopes, let us first define a basic resonance model, as in Fig. 1.8. For a mass, M , which is connected to it's rotating frame by a spring with spring constant k

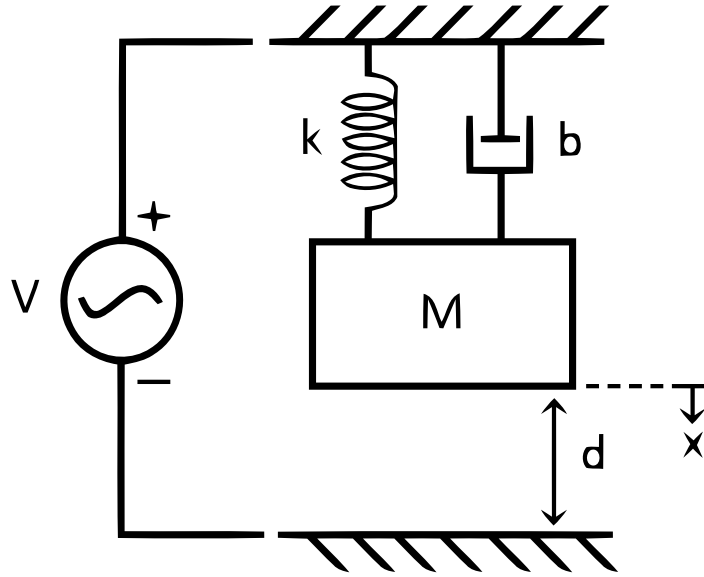


Figure 1.8: Diagram of a basic resonance model. In many cases electrostatic gap-closing actuation is used to induce motion.

and damping b , we have:

$$M\ddot{x} + b\dot{x} + kx = -\omega^2 Mx - j\omega bx + kx = F(t) \quad (1.8)$$

where $F(t)$ is the forcing function. As this equation suggests, spectral analysis will show that at a resonance frequency defined by $\omega_n = \sqrt{k/m}$ the displacement will be maximum for a given force, or conversely, the force required is minimized for a given displacement. Fig. 1.9 shows that at lower frequencies we are dominated by the spring constant, limited by the Q at resonance, and then fall off at -40dB/dec after resonance, as expected from our $-\omega^2 M$ term. This -40dB/dec roll-off means that any attempts to force the mass at frequencies much higher than resonance result in very little displacement. Once in vibration, the gyroscope can be operated in one of two modes: Whole Angle (Rate Integrating) Mode, or Rate Mode. Those gyroscopes which directly measure an angular rotation are called whole angle, rate-integrating, or Type I gyroscopes. Those that measure angular rate, which then

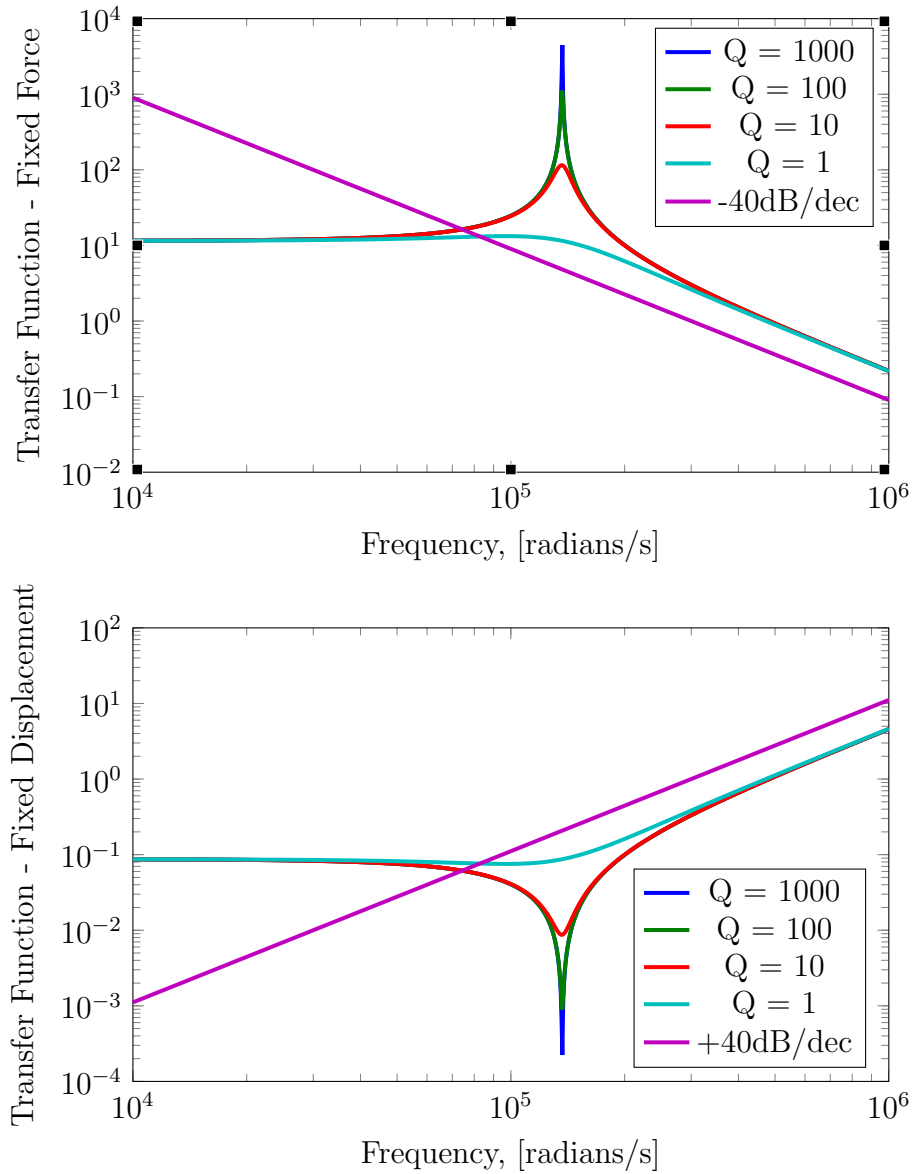


Figure 1.9: Spectral analysis of a basic resonance model, plotted for both constant force and constant displacement.

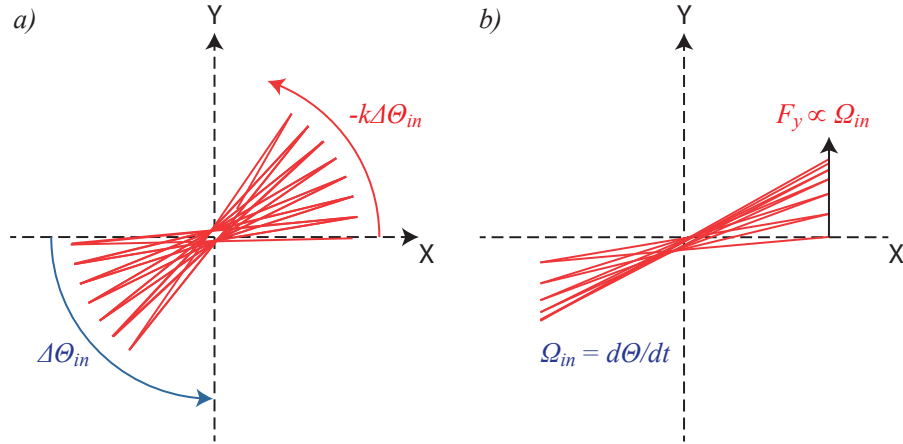


Figure 1.10: Graphs of the motion of a vibrating mass for a) whole angle gyros and b) rate gyros.

must be integrated to find the rotation angle that has been passed through, are called rate or Type II gyroscopes. These two types are visually summarized in Fig. 1.10. It can be seen clearly from this figure that for whole angle gyros the energy, $U = KE + PE$, is kept constant, while for rate gyros one axis is forced to keep its displacement, x , constant.

Equations of Motion

Let's take a quick look at the physics of a vibratory gyroscope. Let us assume that we have a mass, m , which is vibrating in the x axis with some speed \vec{v} , as shown in Fig. 1.11. If the vibrating mass then undergoes some rotation, $\vec{\Omega}_z$, the Coriolis effect will result in a force in the negative y direction. As we derived in Appendix A, a mass rotating at a constant angular velocity can be described in its rotating coordinate system by:

$$m \frac{d^2 \mathbf{r}}{dt^2} = \mathbf{F} - m\boldsymbol{\Omega} \times (\boldsymbol{\Omega} \times \mathbf{r}) - 2m\boldsymbol{\Omega} \times \frac{d\mathbf{r}}{dt} \quad (1.9)$$

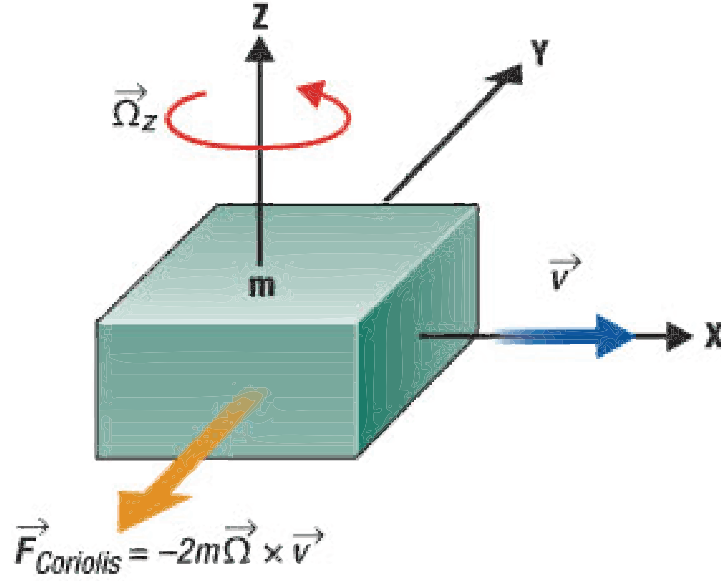


Figure 1.11: Working principle of a vibratory gyro.

Looking at each axis separately, we can use this general equation to find the equations of motion in the XY plane.

$$m\ddot{x}\hat{\mathbf{i}} = F_x\hat{\mathbf{i}} - m\Omega^2x\hat{\mathbf{i}} + 2m\Omega\dot{x}\hat{\mathbf{j}} \quad (1.10a)$$

$$m\ddot{y}\hat{\mathbf{j}} = F_y\hat{\mathbf{j}} - m\Omega^2y\hat{\mathbf{j}} - 2m\Omega\dot{y}\hat{\mathbf{i}} \quad (1.10b)$$

Let us then assume that there is some spring with spring constant $k_{x,y}$ in each axis which supports the vibratory motion with some damping factor $c_{x,y}$, and that an external force is inducing motion in each axis. Rearranging the terms of Eqns 1.10a and 1.10b to look at the motional dynamics in each axis, we get:

$$m\ddot{x} = -b_x\dot{x} - k_x x + m(\Omega^2x + 2\Omega\dot{y}) + F_{ext,x} \quad (1.11a)$$

$$m\ddot{y} = -b_y\dot{y} - k_y y + m(\Omega^2y - 2\Omega\dot{x}) + F_{ext,y} \quad (1.11b)$$

Often it is easier to describe systems in terms of resonance frequency and the quality factor of the resonance; defining $\omega_x = \sqrt{k_x/m}$, $\omega_y = \sqrt{k_y/m}$ and $Q_x =$

ω_x/b_x , $Q_y = \omega_y/b_y$, we can rewrite Eqns 1.11a and 1.11b as:

$$\ddot{x} + \frac{\omega_x}{Q}\dot{x} + (\omega_x^2 - \Omega^2)x - 2\Omega\dot{y} = \frac{F_{ext,x}}{m} \quad (1.12a)$$

$$\ddot{y} + \frac{\omega_y}{Q}\dot{y} + (\omega_y^2 - \Omega^2)y + 2\Omega\dot{x} = \frac{F_{ext,y}}{m} \quad (1.12b)$$

We can now modify Eqns 1.12a and 1.12b for whole angle or rate mode operation.

Whole Angle Operation In the case of whole angle operation, it is assumed that the damping factor is very small such that without any external forces being applied, the mass will vibrate for a long time (this time will determine the operation time of the gyro, after which it will effectively need to be ‘reset’). For this case, the equations of motion become:

$$\ddot{x} + (\omega_x^2 - \Omega^2)x - 2\Omega\dot{y} = 0 \quad (1.13a)$$

$$\ddot{y} + \frac{\omega_y}{Q}\dot{y} + (\omega_y^2 - \Omega^2)y + 2\Omega\dot{x} = \frac{F_{ext,y}}{m} \quad (1.13b)$$

The quality factors of the mechanical resonance need to be very high in order for the gyro to have a long ring down time, and any finite ring down time will require the gyroscope to be ‘re-pinged’ periodically. One possible solution to avoid this would be to use a parametric excitation to pump energy into the system to counteract any losses. As long as this excitation can be achieved isotropically, the apparent phase between the x and y axes (and thus the reading of the angle the gyro has passed through) will not be affected by the addition of energy to the system.

However, in both these cases, the stiffness and damping of the mass must be isotropic at all angles of rotation. In the case that it is not, the mass will not precess linearly with an input rotation, but will instead be a function of each of these parameters at each angle. Novel designs such as that of the Quadruple

Mass Gyroscope (QMG)[2] use multiple masses vibrating in orthogonal axes with levers to synchronize the phase in order to achieve the required isotropy using conventional 2D micro-fabrication techniques. More complex control systems, such as that demonstrated in [3] use PLLs and separate frequency tuning and damping compensation channels for each resonance mode to allow operation as a whole angle gyro.

Rate Operation There are multiple modes of operation for a rate gyro: open-loop, partially closed-loop, force-to-rebalance, and frequency or phase modulation. However the defining characteristic of vibratory rate gyros is that they designate one axis as the drive and one axis as the sense. Thus, for an open-loop system, a periodic forcing function is applied to the drive, and the resulting amplitude of displacement in the sense axis is used to determine the Coriolis force, and thus angular rate, experienced. The system equations, assuming the x-axis to be the drive and y-axis to be the sense for a rotation in the z-axis are written:

$$\ddot{x} + \frac{\omega_x}{Q}\dot{x} + (\omega_x^2 - \Omega^2)x - 2\Omega\dot{y} = \frac{f \sin(\omega_d t)}{m} \quad (1.14a)$$

$$\ddot{y} + \frac{\omega_y}{Q}\dot{y} + (\omega_y^2 - \Omega^2)y + 2\Omega\dot{x} = 0 \quad (1.14b)$$

Assuming x-axis velocity of the mass is known, the amplitude of the displacement in the y-axis will give the angular rate. However, manufacturing inconsistencies and operational conditions such as temperature can affect the drive-mode velocity through various phenomena.

This is why many gyros employ closed-loop operation for the drive-mode using automated gain control. Using a PLL to lock the frequency of oscillations in the drive and automated gain control to set the amplitude of displacement for the

drive simplifies Eq. 1.14a to:

$$x = \sin(\omega_d t) \quad (1.15a)$$

$$\ddot{y} + \frac{\omega_y}{Q}\dot{y} + (\omega_y^2 - \Omega^2)y + 2\Omega\dot{x} = 0 \quad (1.15b)$$

With the displacement and frequency constrained, the velocity of the drive mode is completely determined. Some systems do use direct measurement and control of the velocity signal, and though this voids the need for a PLL, jitter and noise are typically increased[4].

The force-to-rebalance mode of operation is very similar to the operation of the strap-down angular momentum gyro. In the case of the strap-down gyro, a closed loop system was used keep the angular momentum vector of the mass pointed the same direction while measurement of the torque applied to do so lead to the angular rate. In the same way, force-to-rebalance vibratory gyros apply a force to keep the velocity vector pointing in the same direction and use the measure of this force to determine the angular rate from the Coriolis force equation. (Though in this case the force is applied directly at the sense axis, since vibrating masses are at highest velocity when the restoring force is zero, and thus the sense axis displacement is by definition 90° out of phase with drive signal.)

The last mode of operation for rate gyros is frequency modulation, such as that shown in [5]. Though most of the cases discussed above worked under the assumption that either the resonant frequency was fixed through a PLL based control or that Ω was negligibly small compared to ω_x or ω_y , FM based gyros take the centrifugal force and cross-axis coupling into account when determining the frequency of the resonator under rotation. In the case where the axes are initially

mode matched ($\omega_x = \omega_y$ for $\Omega = 0$), this leads to:

$$\omega_x = \omega_0 + \Omega \quad (1.16a)$$

$$\omega_y = \omega_0 - \Omega \quad (1.16b)$$

Thus the rotation rate can be found simply from the differential of the dynamic resonant frequencies of each axis. This phenomena can be attributed to the dynamic cross-coupling of the Coriolis force: if the x-axis is driven to resonance, and then set to rotate, it will transfer energy to the y-axis. The y-axis in vibration will then lead to a force term in the -x direction, reducing the force and appearing as spring stiffening, or resonance increase. (It is important to note that which axis increases in frequency and which reduces will depend not only on the rotation direction, but also the phase relationship between the defined x and y directions. The above equations are valid for the standard $\boldsymbol{\Omega} \times \mathbf{x} = \mathbf{y}$ defined axes, where Ω is defined as a positive rotation.)

The above equations can be arrived at in a simplified derivation for the mode-matched case by looking at the motion equations where both Coriolis and centrifugal forces are taken into account. It is quite easy to see that for a non-coupled system with centrifugal force, the resonance is found to be $\omega_0 = \sqrt{\omega_n^2 - \Omega^2}$ where ω_n is the natural resonance frequency of the mass given by $\sqrt{k/m}$ by finding the solution of:

$$\ddot{x} + (\omega_n^2 - \Omega^2) x = 0 \quad (1.17)$$

Then for the coupled equations

$$\ddot{x} + \omega_0^2 x = 2\Omega \dot{y} \quad (1.18a)$$

$$\ddot{y} + \omega_0^2 y = -2\Omega \dot{x} \quad (1.18b)$$

the solution can be found

$$\beta = \Omega \pm \sqrt{\omega_0^2 + \Omega^2} \quad (1.19)$$

In the case that $\omega_0^2 = \omega_n^2 - \Omega^2$ this simplifies to Eq. 1.16.

Specifications and Figures of Merit

To understand the constraints in the fabrication of a vibratory gyroscope, the specs and FOMs must be clearly defined. The typical specifications designated for a gyroscope are:

- Scale Factor, Scale Factor Stability
- Noise Floor, Resolution
- Dynamic Range, Bandwidth, Linearity
- Bias Drift/Stability
- Angle Random Walk/Rate Random Walk

Scale Factor, Scale Factor Stability This is simply the output response for a given input. For a whole angle gyro, it would be the sensed angle, Θ_{out} (most likely in the form of the ratio of displacements between two sensors), for a given input rotation angle, Θ_{in} . The scale factor of a rate gyro it is typically given as the displacement in the sense axis for a given input rate. For example:

$$SF = \frac{x_s}{\Omega} = \frac{2\omega_d x_d m \mathbb{H}}{k_s} = \frac{2x_d \omega_d \mathbb{H}}{\omega_s^2} \quad (1.20)$$

where \mathbb{H} is the spectral transfer function from drive to sense. This brings to light an important aspect of the design of a gyroscope: mode-matching. Fig. 1.12 shows in the case in which the resonance frequencies of the drive and sense modes are not matched: thus even for a large displacement on the drive, the mass will not move very much on the sense axis, reducing the sensitivity of the gyro. However, it is sometimes desirable to trade off this sensitivity for the bandwidth, fabrication

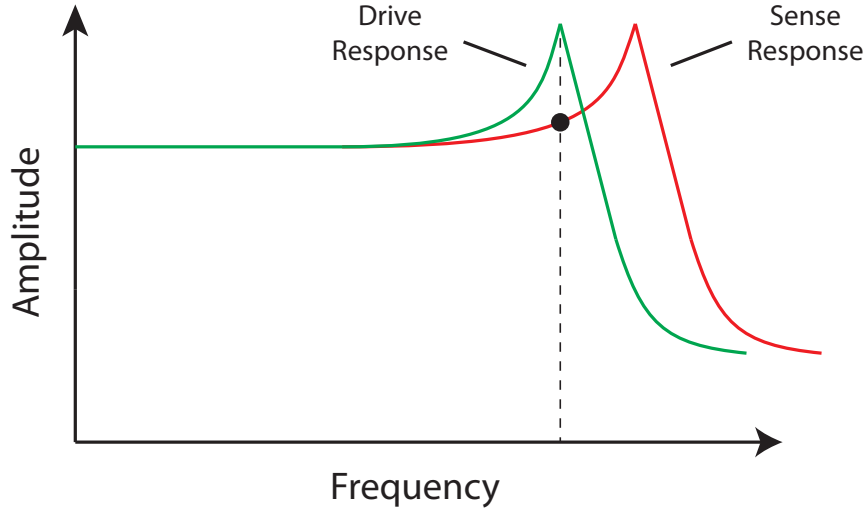


Figure 1.12: Frequency spectra of amplitude response for non-mode matched drive and sense. The black dot represents the value of the transfer function as specified by \mathbb{H} in Eq. 1.20.

tolerance, and thermal stability gained by intentionally offsetting the resonances. Scale factor stability refers to the ability of the gyro scale factor to stay the same under various operating conditions, and over time. Temperature compensation especially can be important in keeping the scale factor stable.

Noise Floor, Resolution The noise floor in combination with the scale factor will determine the resolution of the gyroscope. Though in the past amplifier noise was the dominant noise source, as electronics have improved, sensor noise is commonly dominant. If we assume that brownian motion - the white noise motion caused by random impinging of gas molecules on the structure - is the dominant noise source, and that the brownian noise force is given by:

$$\bar{F}_{bn} = \sqrt{4k_B T b_s} \cdot \sqrt{BW} \quad (1.21)$$

For a rate gyro, we are limited by the linearity of the sensor to small input rates, and thus assume that any brownian noise on the drive axis would not be significant

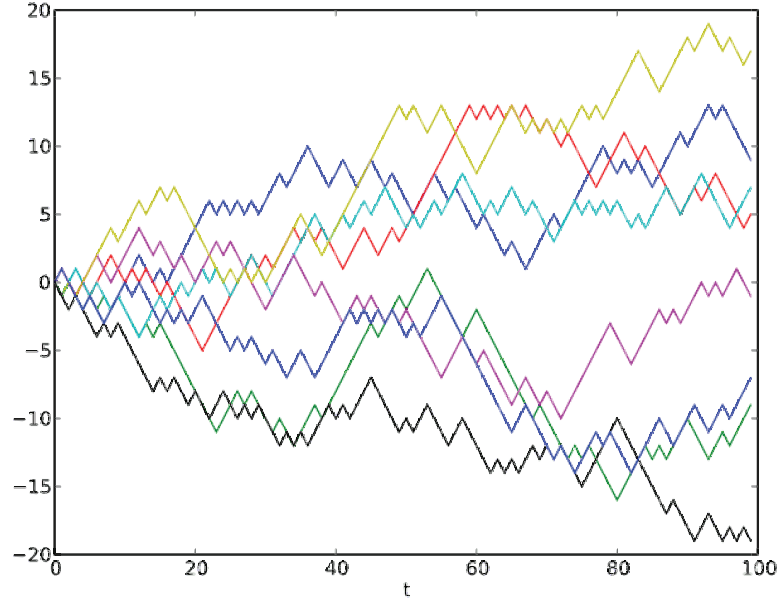


Figure 1.13: Random walk of integrated signals. For the case of the rate gyros, this leads an important FOM: Angle Random Walk.

compared to the noise coming directly from the sense axis. Our Coriolis force is given by

$$F_{Cor} = 2m\omega_d x_d \Omega_{in} \quad (1.22)$$

Setting these two equal, we can find the minimum detectable signal, or resolution, of the sensor:

$$\frac{\Omega_{min}}{\sqrt{BW}} = \frac{1}{x_d} \sqrt{\frac{k_B T \omega_s}{m \omega_d^2 Q_s}} \quad (1.23)$$

Clearly, higher Q's, more mass, and more drive displacement will all lead to a lower minimum detectable signal, but they also lead to non-linear regimes. Increasing the resonant frequency does not cause this problem, but it will reduce the displacement of the sensor. However, it is important to note that we are only detecting the angular rate here; the signal needs to be integrated to see the angle that has been rotated through. Integration of the signal means that both sensor and electronic noise will be integrated as well, leading to a random 'walking' of the detected angle

away from it's actual value.

What about the whole angle case? This is slightly different, in that we will need to figure out the actual displacement caused by the brownian noise and refer it back to the calculation of the angle. Assuming that there are two sensors, one on the x-axis and one on the y-axis, the rotation angle can be calculated from $\tan \phi = \frac{x}{y}$. However, the sensitivity of the \tan^{-1} function to variations in each of the displacements will change based on the angle the mass is currently resonating at. For instance, if the mass is mostly resonating along the x-axis, the \tan^{-1} function is at it's minimum slope, and the minimum detectable signal would be lowest. However, when it is vibrating mostly along the y-axis, the \tan^{-1} slope is essentially maximum. Assuming a smart circuit designer would flip his definition of the angle being read when the orbital passes 45° , the minimum detectable signal can be found by looking at the effect of brownian noise displacement on the angle read out when the mass is resonating along the 45° axis. Additionally, since the calculation of the angle is based on a ratio of displacements, it is pointless to look at a system where there is only brownian noise; in that case brownian noise could dictate any angle, rather than some small noise equivalent rate as seen above. Instead, we must determine the minimum detectable angle for a given displacement. For example, for the case in which the free vibrations of the mass are only twice the brownian noise displacement, the minimum detectable signal would be given by:

$$\tan \phi = \frac{x + \bar{x}_n}{y - \bar{y}_n} = \frac{3}{1} \Rightarrow \phi = 71.565^\circ \quad (1.24)$$

This is a pretty bad number! Let us now look at the case in which the free vibrations are 100 times the brownian noise displacement:

$$\tan \phi = \frac{x + \bar{x}_n}{y - \bar{y}_n} = \frac{101}{99} \Rightarrow \phi = 45.573^\circ \quad (1.25)$$

A ratio of 1000/1 improves to 45.057° .

Dynamic Range, Bandwidth, Linearity Dynamic range is defined as the ratio of the maximum value of the measurand to meet a given accuracy spec divided by the minimum measurable value. For a rate gyro, as we have talked about previously, maintaining linearity in the device will limit the input rotation rate, while the minimum measurable value will be given by the noise floor. The BW of a rate gyro is typically given as $\frac{\omega_n}{2Q}$, and will determine the time it takes for the rate gyro to settle on the expected output value. Rate gyros with very high Q, and thus a very low noise floor will have very small BW, and can take as much as minutes to settle on the expected output value for high resolution systems. Whole angle gyros, on the other hand, due to free precession, have essentially unlimited bandwidth, and as long as $\Omega \ll \omega_n$, the rotation angle will be measurable.

Bias Drift/Stability The bias of a gyro is the angle that is output for a zero input rotation rate or angle. Systematic errors, such as fabrication imperfections that cause the drive axis forcing function to induce motion in the sense axis (known as quadrature error), as well as operational conditions such as temperature can affect this. Quadrature error, known as such because it is 90° out of phase with the sensed Coriolis signal, can be detected and compensated for via its phase. Temperature compensation or matching of the drive and sense thermal response is often put into effect to account for thermal changes. Oftentimes, the startup of a gyro will have a certain heating/settling time, and the term bias drift can refer specifically to that. Bias stability, on the other hand, is a spec that refers to the minimum achievable signal variance assuming averaging over an optimal time period. This value is found using an analysis technique called Allan variance, or Allan deviation, which I will talk about more in the next section.

Angle Random Walk/Rate Random Walk Angle random walk (ARW) is a term that was coined for rate gyros, and refers to the fact that as white noise in integrated over time, as must be done to find the rotated angle from the angular rate, the output measured angle will have a tendency to randomly ‘walk off’ in different directions, causing either positive or negative angle error values whose statistical variance increases with time. Since this is a white noise issue, averaging will help, but at some point bias drift errors, which are more long term, will begin to dominate. This is the point designated by the bias stability term, and determines the integration period of averaging. Meanwhile, the inherent mechanical integration of whole angle gyros allows for a natural averaging of brownian noise effects and no electronic integration need be performed.

Rate random walk refers to noise sources which are even more long term than bias drift, and directly affect the rate being read out. Just as the bias drift is defined by an output angle for zero input rate, rate random walk refers to drift in the output rate for a given input rate. This is then doubly integrated, leading to a noise source whose PSD has a $1/f^2$ dependence, and meaning that while we want to average over as long a period as possible to get rid of white noise errors, if we average for too long, drift in the rate itself will dominate the variance of the signal.

Bias drift, angle random walk, rate random walk, not to mention quantization noise are all terms that will affect the best usage of a gyro, and their characterization is important for setting the averaging parameters used. A statistical method of analyzing the effect of various noise sources on the variance of the output angle, called the Allan variance, is used to do this.

Allan deviation, $\sigma(\tau)$, is effectively the average variance between successive

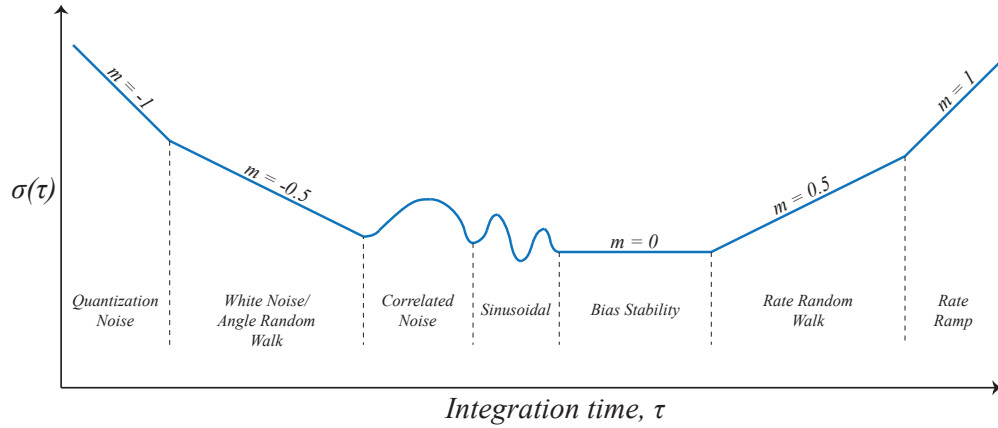


Figure 1.14: Allan deviation of a rate gyro. The variance of the output angle term is shown on the $\sigma(\tau)$ axis. τ is the averaging integration time, or binning time.

chunks, or bins, of averaged data, defined by:

$$\sigma^2(\tau) = \frac{1}{2(n-1)} \sum_i (a_\theta(\tau)_{i+1} - a_\theta(\tau)_i)^2 \quad (1.26)$$

To understand the impact of a given noise source, it may be more illustrative to look at the affect of frequency dependence of a noise source on the slope of the Allan deviation. If the order of the frequency dependence for the PSD of a noise source is given by α , then:

$$PSD(f) \propto f^\alpha \quad (1.27a)$$

$$\sigma(\tau) \propto \tau^{-(\alpha+1)/2} \quad (1.27b)$$

We see from the above set of equations that the slopes shown in Fig. 1.14 match up for:

Table 1.1: PSD and Allan Deviation of various noise sources

Noise Source	PSD $\propto f^\alpha$	$\sigma(\tau) \propto \tau^{-(\alpha+1)/2}$
Quantization Noise	$\propto f^1$	$\propto \tau^{-1}$
White Noise	$\propto f^0$	$\propto \tau^{-1/2}$
Bias Stability	$\propto f^{-1}$	$\propto \tau^0$
Rate Random Walk	$\propto f^{-2}$	$\propto \tau^{1/2}$
Rate Ramp	$\propto f^{-3}$	$\propto \tau^1$

The rate ramp value given in the table and in Fig. 1.14 is a deterministic noise source with $\frac{1}{f^3}$ frequency behavior[6].

Hemispherical Resonator Gyroscope

Among vibratory gyroscopes available today, there is one structure which stands out in terms of performance: the Hemispherical Resonator Gyroscope. We will take a quick look at the operating principle of that device.

Fig. 1.15 shows a Hemispherical Resonator Gyroscope (HRG) produced by Northrop Grumman. These gyroscopes not only have very high performance, but are also low noise, relatively small, have long lifetimes, and are naturally radiation hard. It is for these reasons that HRGs are often chosen for the guidance systems of spacecraft and satellites, and Northrop Grumman boasts that its HRG has over 25 million hours in space without a single mission failure [7].

The operating principle behind the HRG is based off a paper written in 1890 by Mr. G.H. Bryan called ‘On the beats in the vibrations of a revolving cylinder or bell’. Mr. Bryan explained the observed affect of beats heard when rotating

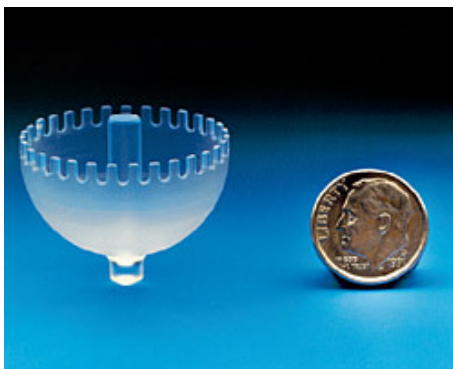


Figure 1.15: The Hemispherical Resonator Gyroscope by Northrop Grumman. The tines on the edge of the device are for frequency tuning/balancing of the gyro.

a ringing wineglass, or when the observer them self is rotating with a ringing wineglass. The fact that beats are heard in both cases indicates that whatever acoustic mode causes the initial ringing does rotate, but not at the same angular rate as the rotation.

If we think about the acoustic mode set up in the wineglass structure as shown in Fig. 1.16 having some momentum, then it makes sense that the acoustic wave would want stay stationary in the inertial frame of reference. This would explain the case of some one rotating with a ringing wineglass hearing beats. However, the case of hearing beats when only the wineglass is rotating infers that the acoustic wave does rotate as the wineglass does. A simplified explanation of why the wineglass mode does not stay fixed is that not all of the momentum of the resonating mode is translational; the portion that is rotational has its vector component along the same axis as the rotation, and thus the Coriolis force term yields no force on these nodal portions of the structure[8]. As the wave transfers around the wineglass, it will end up traveling at a speed proportional to the ratio of angular to

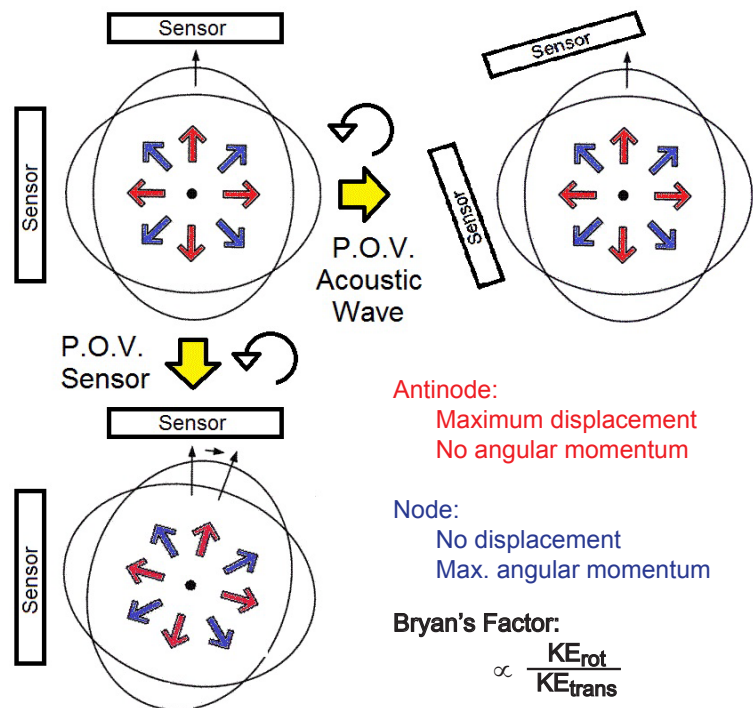


Figure 1.16: Response of wineglass modes of vibration to input rotation. The scale factor between the angular rate of rotation of the acoustic wave and the rate of the rotation is defined as the Bryan's factor, BF.

translational kinetic energy, defining the Bryan's factor:

$$BF = \frac{\text{angular rate of acoustic wave}}{\text{angular rate of structure}} \propto \frac{KE_{rot}}{KE_{trans}} \quad (1.28)$$

For a hemispherical shell, $BF \approx 0.3$. As we saw previously, for the Foucault pendulum, $BF = 1$, which we would expect from the fact that all momentum is translational.

The HRG uses a hemispherical shell resonator formed out of quartz, with individual precision trimming for balancing and frequency matching, and can be run either in whole angle or rate gyro mode. However, it costs upwards of \$10,000 for a single axis gyro, and is still quite large.

1.2 Target Device

The previous sections were quite a long introduction to gyroscopes, especially considering this dissertation's topic is on the fabrication of a gyroscope structure rather than the actual gyroscope characterization itself. However, in addition to being an introduction to terms, I hope that the preceding information has impressed upon you 1) that vibratory gyroscopes are the prime candidate for micro-scale gyros, and 2) that whole angle operation of a high Q, mode-matched gyro is advantageous.

The criteria used in the design process for our target device were these:

- Micro-scale
- Mass manufacturable
- Capable of whole angle operation
- Navigation grade

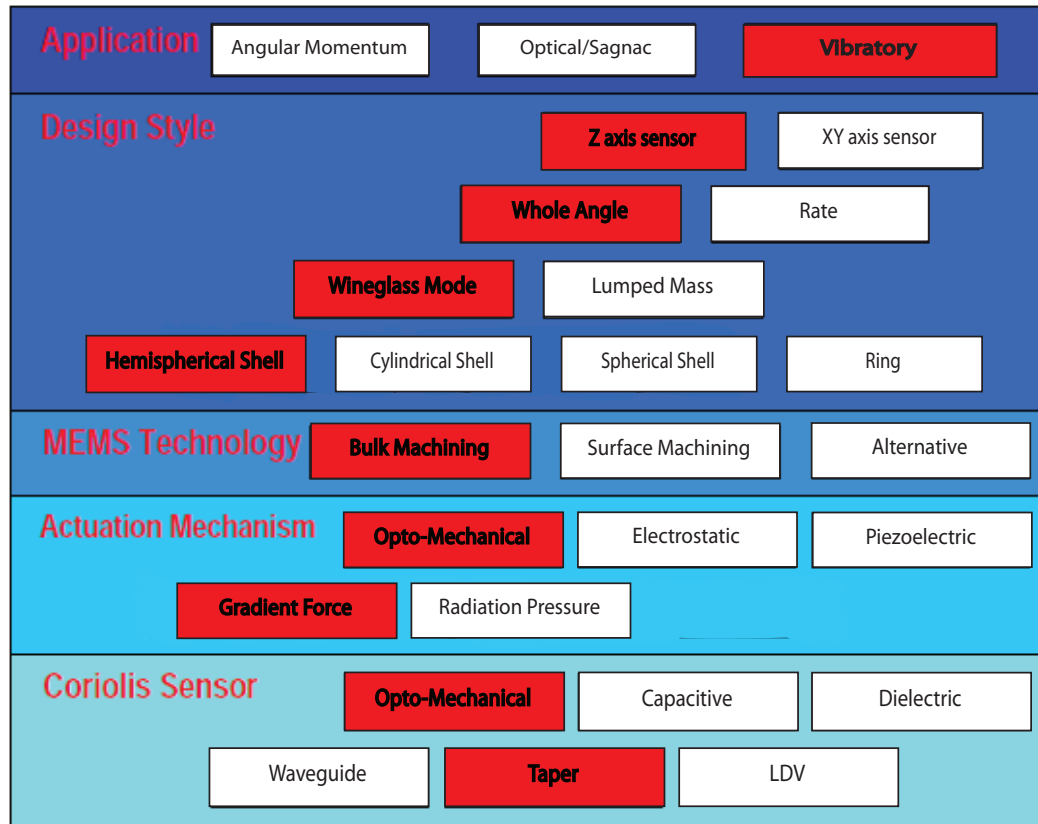


Figure 1.17: Design flow for target structure.

By following these design criteria, we hope to create a chip-scale integrable gyro which has the capability of being used for inertial navigation systems, an ideal desirable to both industry and military applications.

Fig. 1.17 shows the choices made in the design of the target structure.

Application As mentioned previously, neither the low friction bearings nor the necessary path length required for angular momentum or Sagnac effect based gyros scale well to the chip-scale level. For this reason, a vibratory gyroscope is chosen.

Design Style Some gyros are designed to measure not only one axis, but by using multiple masses with coupled behavior or a mass which ‘swings’ in its plane of motion, dual-axis rotation measurements can be made. However, accomplishing such dual-axis measurement while in a whole angle measurement mode would require freedom of motion along all three axes, as well as sensing in 3 dimensions. To simplify the gyro and computing power necessary to run it, our gyro is designed for a single axis measurement.

We have already stated that operation as a whole angle gyro is one of our design criteria, though seeing as the difference between whole angle and rate operation as explained thus far seems to be only in the forcing conditions, it is unclear as to how such a criteria affects the sensor design. However, up until this point we have been assuming the ability to perfectly match the resonance frequencies and damping of orthogonal axes at any point along the precession of the mass. Due to fabrication inconsistencies and lithographic limitations this is actually very difficult to achieve. Locking of the mode frequency requires continuous forcing, and thus most vibratory gyros are rate gyros. However, the improvements in BW, angle random walk, and relaxing of the tradeoff between high Q and linearity make whole angle operation ideal.

We have mentioned the QMG, which makes use of multiple masses to achieve whole angle operation. This is certainly a viable option, and fits all of the design criteria we have specified above. However, the sensitivity of devices such as the QMG to shock, vibration, and linear accelerations has not been published; such parameters are essential to the gyro, particularly for military applications. Wine-glass modes, which often use 3 dimensional rather than planar geometries, tend to be more resistant to out of plane shocks.

Such planar responses to shock are reduced for 3D geometries, and thus we exclude the idea of using a ring for our structure. Cylinder shapes tend to have large anchor losses and are also removed. Fully spherical shapes, such as those fabricated in [9] are novel, but it is difficult to reduce anchor size without distorting the shape, and [9] shows an improved Q for spheres that have been cut into hemispherical shell resonators in any case. The birdbath resonator shown in the same reference achieves a small stem, but individual release of each device with a 3D laser ablation system would not meet the mass manufacturability requirement. Thus we choose the hemispherical shell resonator for our structure.

MEMS Technology The various fabrication techniques for MEMS devices tend to fall into two categories: bulk micro-machined or surface micro-machined. Bulk micro-machined are those where the structure is built out of the wafer material. Surface micro-machining uses the wafer as a holder and builds upon the surface. Obviously, building up a hemispherical shape would be very difficult to do with standard fabrication processes. However, using bulk manufacturing, a hemispherical shape can be etched out in the wafer surface, and the device layer can then be grown or deposited within that mold. Alternative fabrication such as the glass-blowing techniques shown in [9] show low frequency splitting between modes and good smoothness, but again, reduction of stem size is difficult to achieve.

Actuation Mechanism Up until this point I have largely ignored considerations of the actual actuation mechanism, merely assuming that force can be applied directionally to the mass. Almost all vibratory gyroscopes use electrostatic, or capacitive transduction. This is the transduction type shown in the basic resonance model of Fig. 1.8. There are also other electrostatic actuation mechanisms, such

as comb drives, which use interdigitated fingers and energy minimization principles to actuate. However, electrostatic actuation assumes the ability to control the voltage on the mass, thus limiting usable device materials and requiring routing electrical lines to the mass. Such routing can be especially difficult for 3D devices, and any metals laid onto vibrating portions of the structure will lead to extra damping that cannot be afforded. Dielectric transduction [10] makes use of the fact that a dielectric in an inhomogenous field will be pulled toward the higher intensity. Though the force of such a system is not strong, it allows dielectric materials, which typically have better mechanical properties, to be used. However, such a system requires extensive routing and decoupling of the drive and sense for an all dielectric transduction scheme requires the drive to parametrically pump the system - great for a whole angle gyro case, but rate operation would be limited. Opto-mechanical actuation through the gradient force works on basically the same principle, but since wavelengths do not interact with each other, the drive and sense can be decoupled simply through use of different wavelengths of light. A diagram of radiation pressure vs. optical gradient forces is shown in Fig. 1.18. Optical actuation allows us to use both at once. Radiation pressure relies on momentum being imparted by photons impinging on the cavity walls, and since one photon will impart the same momentum for one lap around a small radius as around a large, this force falls off as $1/R$ for a circular cavity. Optical gradient force is the photonic equivalent of the dielectric transduction method mentioned earlier, and will actually have a slightly increased interaction area for larger radius devices. Combined with the fact that the spring stiffness for a hemispherical shell falls off as $1/R^2$, we expect gradient force effects to dominate a large radius hemispherical shell actuated by opto-mechanical force.

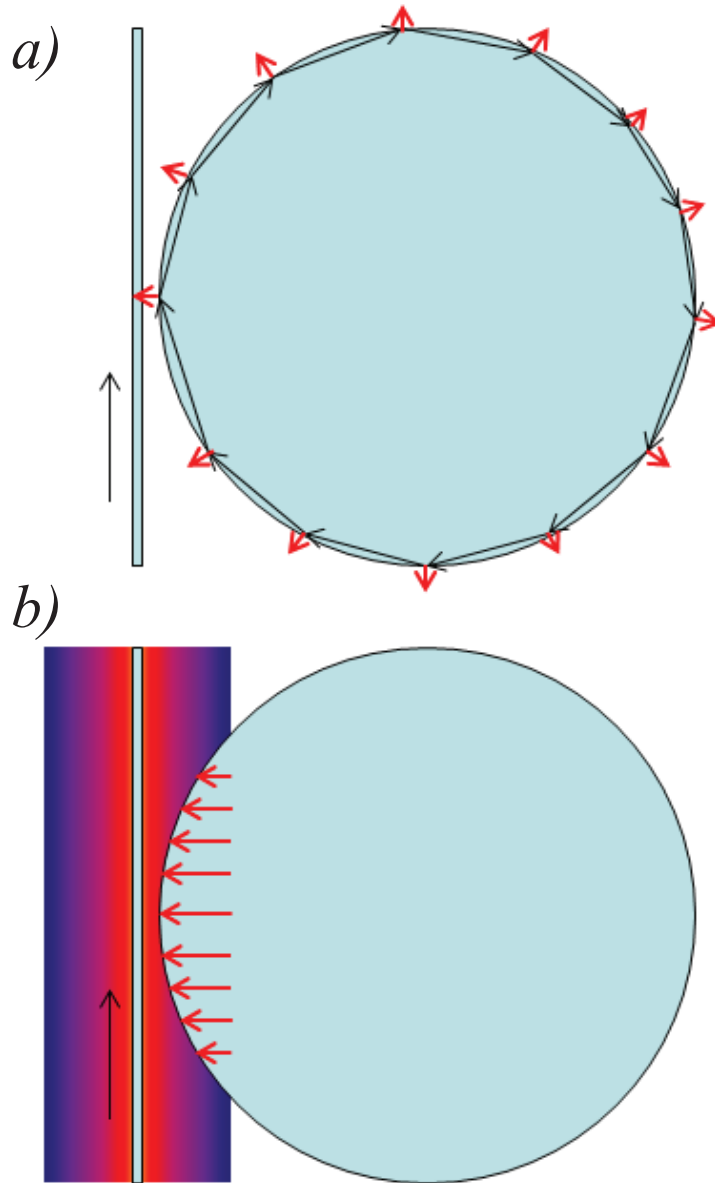


Figure 1.18: Radiation pressure and optical gradient opto-mechanical forces. Radiation pressure (a) allows parametric pumping while gradient forces (b) can be used to induce directional forces.

Coriolis Sensor In the same way, we choose opto-mechanics for the sensing mechanism. We must now answer the question of how we will apply the force and where we will sense the displacement. Obviously, the most integrated approach, and the end goal of the design for an opto-mechanical gyro is to use waveguides that are co-fabricated with the sensor. However, at this point the focus is on the sensor design, and the additional fabrication of waveguides would cause unnecessary complexity in our study, and unduly increase the fabrication time for each process run. Instead, we can make use of an optical taper, a heated and thinned length of optical fiber as in [11]. This allows for fast prototyping while at the same time providing a platform for the actuation of the sensor. Laser doppler vibrometry, which is a technique that uses free space lasers to measure the velocity of a resonating device via relative doppler shifts in reflected light, is a commonly used prototyping technique. However, it does not provide the necessary infrastructure for the actuation, and instead would require a piezoelectric to be glued to the base of the sample to actuate motion.



Figure 1.19: The target structure for this dissertation: the GOBLiT.

1.2.1 GOBLiT

With all our design decisions made, we present the structure shown in Fig. 1.19 as the target structure for this dissertation. We call this structure the GOBLiT:

Giant
Opto-mechanical
Bulk-machined
Light
Transducer

Giant refers to the fact that in designing for use as a gyroscope, we want to maximize mass, and thus optimize for a large device. Before we move on to the fabrication of such a device, let us look at a last few considerations of our design choices.

Table 1.2: Expected HRG scaling performance[12]

Specification	Scaling Law
Natural frequency, ω_n	$\propto \frac{t}{R^2}$
Quality factor, Q	$\propto \omega_n R^2 \propto t$
Damping time constant, τ	$\propto R^2$
Q mismatch, $\Delta (1/Q)$	$\propto \frac{1}{\omega_n R^3} \propto \frac{1}{Rt}$
Damping nonuniformity drift, Ω_d	$\propto \Delta (1/\tau) \propto \frac{1}{R^3}$

Structure Scaling

The device structure we have chosen is essentially a scaled-down version of the HRG, with the exception of transduction method. The HRG has proven excellent performance, but what type of performance can we expect as the hemispherical shell resonator is reduced? Researchers at Northrop Grumman have done a study of the expected scaling effects with the results shown in Table 1.2, where R refers to the radius of the hemisphere and t to the height. Noticeably missing from this table are the expected scaling effects on frequency mismatch. Though the ideal perfectly hemispherical shell would resonate degenerately, i.e. at the same frequency along any rotation about the z axis, any imperfection will cause a splitting of the frequencies of the eigenmodes solved for in finding the resonance. The modal separation will be defined by the azimuthal wave number of the wineglass mode, m , as $90^\circ/m$. The degree of this separation is largely fabrication dependent, and will directly affect the ability of the wineglass mode to linearly precess about the hemispherical shell. Northrup Grumman gets around this issue by balancing the HRG, incrementally removing small amounts of material until the frequencies have regained degeneracy, but this negates mass manufacturability and skyrockets cost.

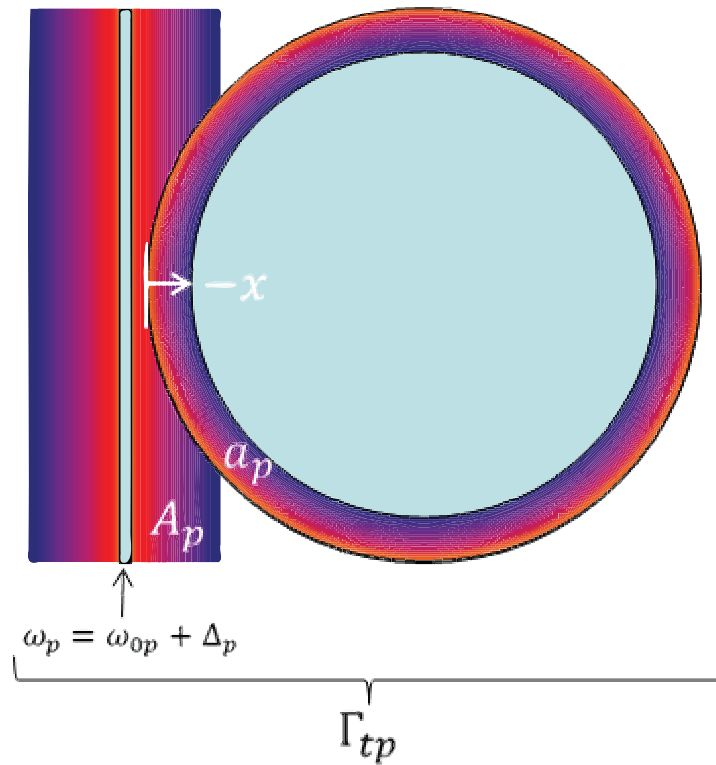


Figure 1.20: Diagram for opto-mechanical modeling.

We see from Table 1.2 that we want a thick device with large radius - i.e. we don't really want to scale down. Essentially, we want to make the largest wafer manufacturable hemispherical shell resonator possible.

Optical Considerations

What is the impact of opto-mechanical actuation and sensing on the fabrication of our device? To answer that question, let us take a closer look at the physics of such a transduction scheme.

For an optical cavity such as that shown in Fig. 1.20, we can define the rate of

change of the intracavity field as:

$$\frac{da_p}{dt} = \left(-i\Delta_p - \frac{\Gamma_{tp}}{2}\right)a_p - ig_{OM}xa_p + i\gamma|a_p|^2a_p + i\sqrt{\Gamma_{ep}}A_p \quad (1.29)$$

It will be clearer for reference to explain each of these terms in a list:

- a_p The light field inside the cavity, where the intracavity energy is given by $U_p = |a_p|^2$.
- Δ_p The detuning between the frequency of the input light and the resonance frequency of the optical cavity, defined as $\Delta_p = \omega_{p0} - \omega_p$, where ω_{p0} is the frequency of the optical resonance of interest and ω_p is the frequency of the input light.
- Γ_{tp} The photon decay rate of the loaded cavity for optical resonance of interest, defined as $\Gamma_{tp} = \frac{\omega_{0p}}{Q_{opt}}$.
- g_{OM} The optomechanical coupling factor, defined as $d\omega_{0p}/dx$. This effectively states how sensitive the optical resonance frequency is to mechanical displacements, and will vary for different mechanical modes of resonance.
- x The mechanical displacement of the cavity structure, a function of time.
- γ A term describing the self-phase modulation introduced by the Kerr non-linearity of silicon dioxide. Please see [13] for more information. We will assume it negligible for our device in comparison to other terms.
- $\sqrt{\Gamma_{ep}}$ The photon escape rate of the external field (i.e. the escape rate from the taper or waveguide).
- A_p The input field of the light wave, which is traveling in the taper or waveguide, and for which the power of the field is given by $P_p = |A_p|^2$.

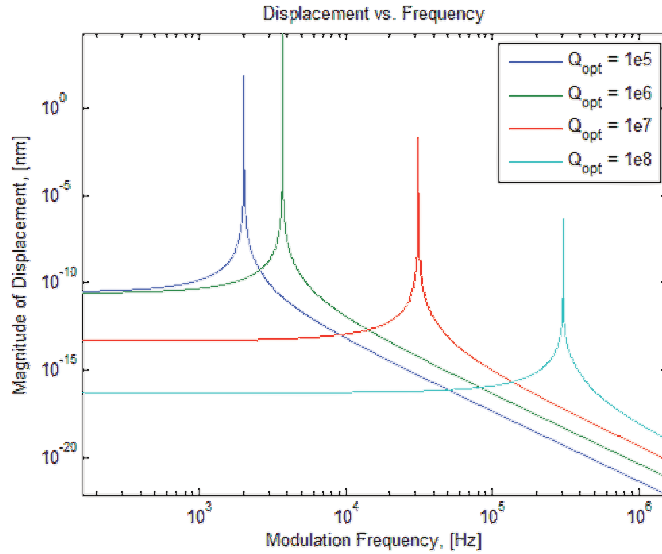


Figure 1.21: Optical spectrum for various Q_{opt} . Clear optical spring effect is seen. Height differences between the first two peaks are due to Matlab plot resolution, not optical effects.

What are these terms really saying? The Δ_p term characterizes the field build up for a given detuning between input and cavity resonance wavelengths. The Γ_{tp} term gives the decay of the field due to total optical losses. The g_{OM} term explains how the intracavity field changes due to mechanical motion of the structure. The last term characterizes the intracavity field increase due to coupling from the taper.

Thus we see that opto-mechanical transduction gives us a major displacement boost due to high optical quality factors. However, just as electrostatic transducers have an electrical spring effect, optical cavities have an optical spring effect. Unfortunately for us, though the electrostatic spring is a softening effect, as we derive in Appendix B, the optical spring effect leads to stiffening. However, considering that the displacement over which optical actuation and sensing can interact with the sensor is extremely limited compared to electrostatic schemes, this may be beneficial. Indeed, adding mass to the structure in such a way as to significantly increase the stiffness without substantially losing momentum, and thus sensitiv-

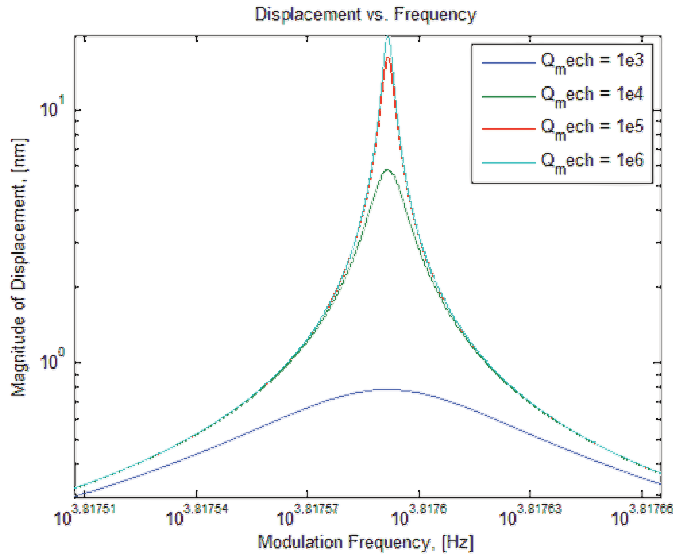


Figure 1.22: Optical spectrum for various Q_{mech} . Q_{mech} displacement enhancement is preserved in the optical model.

ity, may be a beneficial trade off in an optically transduced gyro. One way to do this would be to add a planar lip to the hemispherical shell shape, which gives the additional benefits of providing a well defined optical cavity to the device and reducing fabrication complexity, though at the expense of adding parasitic modes. Fig. 1.21 shows the optical spring effect for various values of Q_{opt} .

Process Flow

A basic process flow for the GOBLiT is shown in Fig. 1.23. After laying down a masking layer and patterning etch windows, an isotropic etch results in the device mold. After removing the masking layer and depositing the device layer, the rim of the lip is patterned and etched. The last step is to perform a second isotropic etch to release the device and create the stem.

Now we come to the real question: What is possible with current fabrication

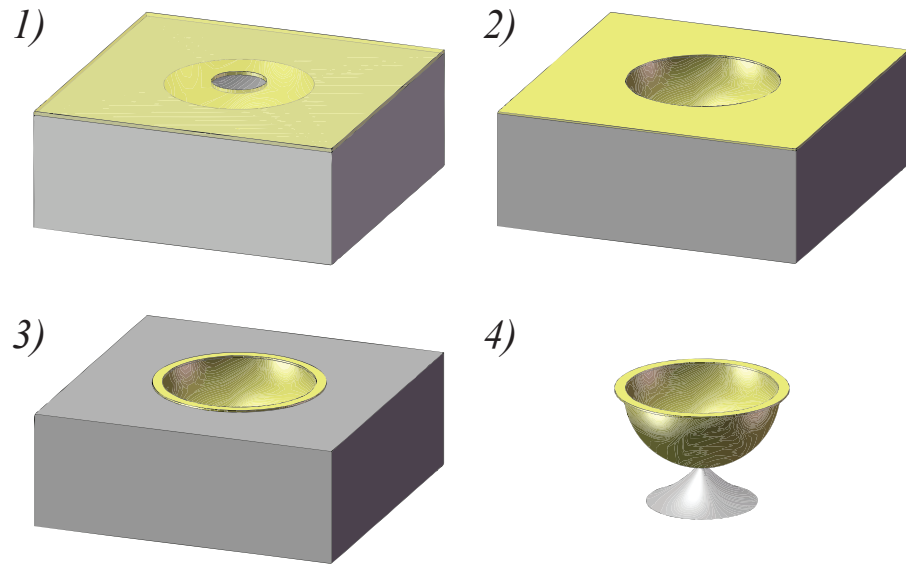


Figure 1.23: Basic GOBLiT process flow.

technology?

Part I

Fabrication Considerations

CHAPTER 2

BULK ETCHING

Our designed process flow requires the initial isotropic etch to be very isotropic and very smooth. The three candidates we have for isotropic etching of a silicon wafer are HNA, XeF_2 , and SF_6 . The XeF_2 and SF_6 etches are dry etches, while HNA is a wet etch. Dry etches would be preferable for fabrication uniformity considerations, but both XeF_2 and SF_6 are known to be rather rough etches. Additionally, the etching conditions required for an isotropic SF_6 etch were not available to us at the CNF, though an appropriate ICP etcher is shortly to be installed.

XeF_2 is a gas phase etch which isotropically etches Si with extremely high selectivity to oxide, and good selectivity to nitride. The reaction equation is given by:



XeF_2 etching roughness can be improved by reducing the XeF_2 gas pressure, or adding N_2 buffer gas, but at the cost of significant reduction in etch rates.

HNA is short for HF, Nitric, Ascetic, and refers to the three acids typically mixed to create this isotropic Si wet etch. Since CNF does not allow the mixing of these three acids due to waste disposal issues, we instead replace the ascetic acid with deionized water. Such etch mixtures have been studied, and the main difference is due to the larger dielectric constant of water causing more dissociation of the nitric species in the HNW mixture. From this point on in the text, we will refer to the HNW mixture as HNA. The main components of the etch are the HF and Nitric acid. Nitric acid is a very strong oxidizer, and thus the first part of the

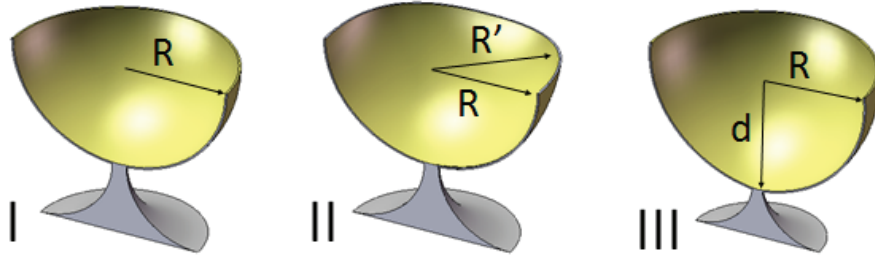
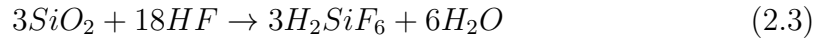


Figure 2.1: Anisotropy archetypes of isotropic etches

HNA reaction proceeds as:



HF is then used to etch away the silicon dioxide that has been formed as:



Though it seems straightforward, HNA is actually a quite complex etch, which is exothermic, temperature dependent, and has autocatalytic properties. References such as [14] have done studies of the effects of etch volume, etch mass, and etchant volume on HNA etch rates, but chemistry papers still debate the exact nature of the reaction.

It is clear that optimization of the device geometry will depend largely on the isotropic mold etch. Fig. 2.1 shows archetypes of common anisotropic patterns seen in isotropic etching. I shows an isotropic etch, II an etch with what we will refer to as XY anisotropy, and III shows Z anisotropy. XY anisotropy will have major effects on the frequency splitting, and is thus the main anisotropy addressed. Z anisotropy will have some effect on shock and acceleration rejection, as well as anchor loss. Smoothness of the etch will directly affect the mechanical quality factor, and thus the ring down time, of the gyro.

For verification of the smoothness achievable with XeF_2 and HNA, we performed some initial test etches. Figs. 2.2 and 2.3 show the results of those etches.

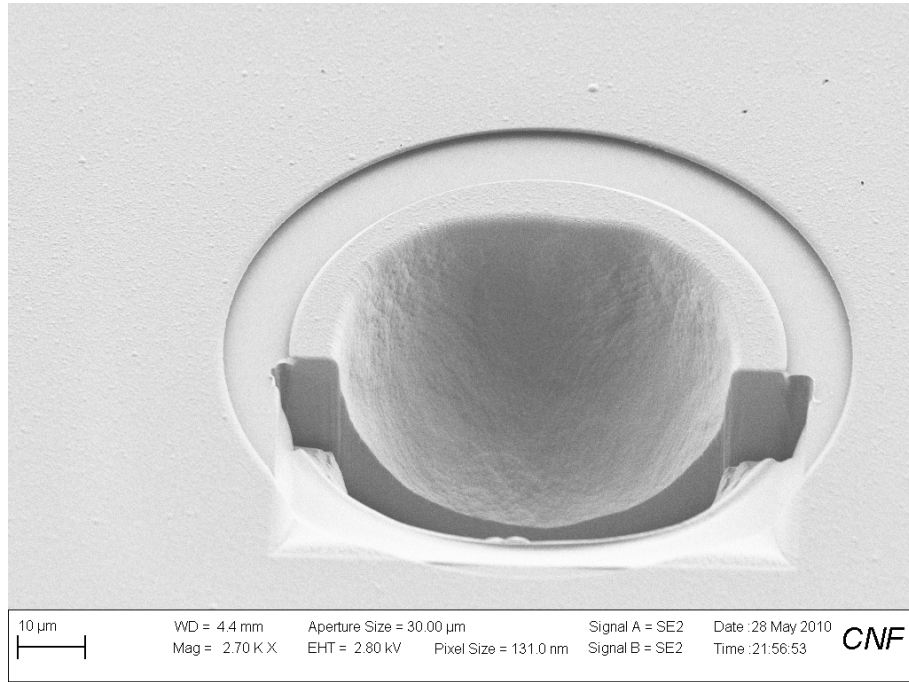


Figure 2.2: SEM of HNA anisotropy. FIB was used to define a perfect circle, which accentuates the XY anisotropy.

Though neither was spectacularly smooth or isotropic, the HNA etch showed more promise in that it was smoother and the shallowing of the etch in the Z direction could be avoided by agitation during the etch. Literature also suggested that regimes could be found where much smoother etches were possible[15]. Some attempts by other researchers have been made to improve smoothness of rough etches by oxidizing and removing the oxide layers or using very smooth HNA etches after rougher XeF_2 or SF_6 etches, but these were always limited by larger feature roughness [ref?].

The anisotropy of an HNA etch had been well documented for the $\langle 100 \rangle$ and $\langle 110 \rangle$ silicon case in [16]. However, we theorized the $\langle 111 \rangle$ may have better HNA etching anisotropy, since the crystallographic planes of the slowest to fastest etching directions form a hexagon in the XY plane, which better approximates a

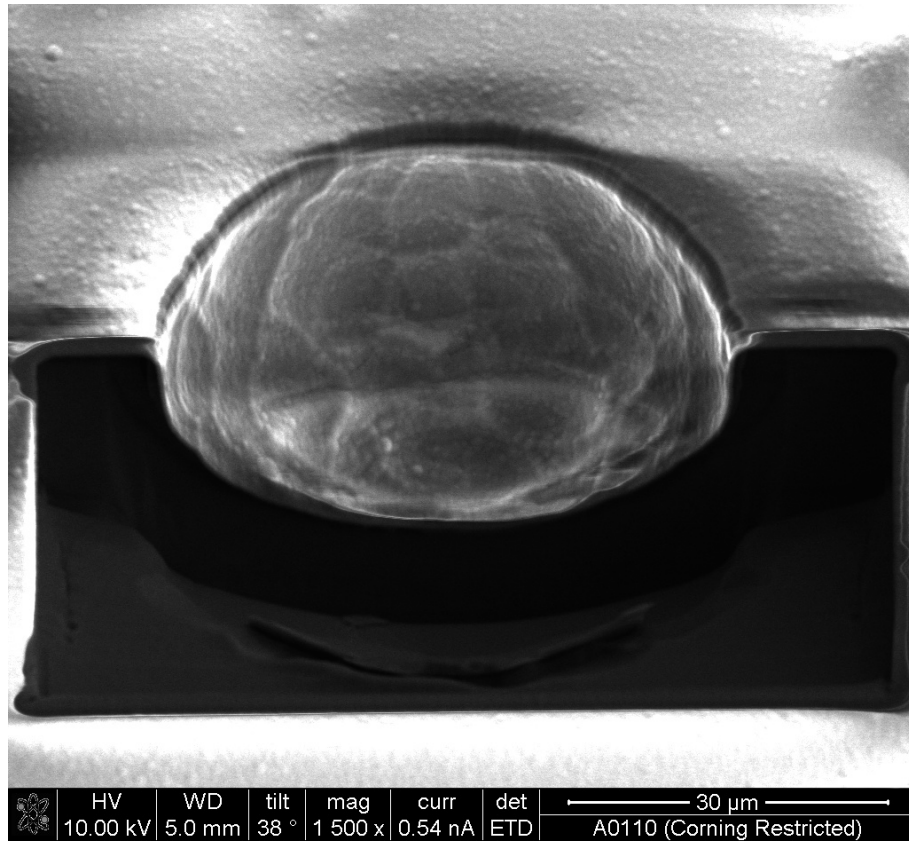


Figure 2.3: SEM of XeF_2 etched mold. Though anisotropy is improved, shallowing and roughness are unacceptable.

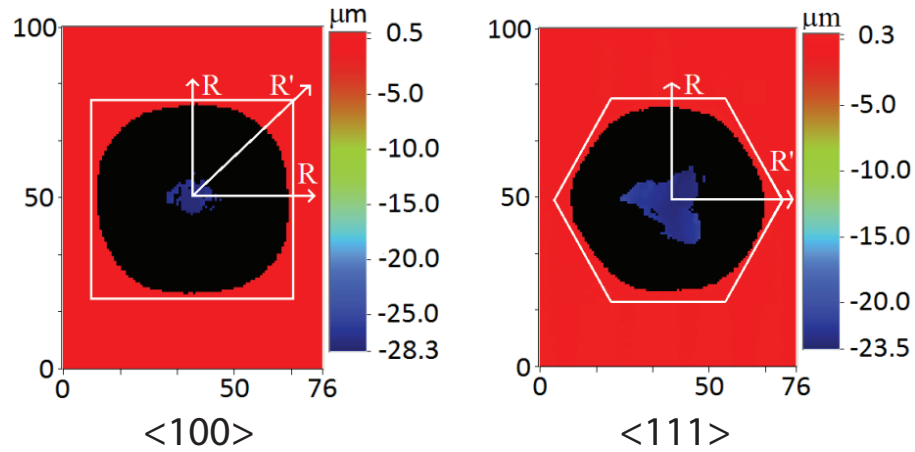


Figure 2.4: Optical profilometer data showing anisotropy of HNA etch for <100> and <111> Si. Radii for defining preferential etching are shown.

circle. However, a study on the HNA etching of <111> Si had not been performed.

The initial etches performed, shown in Fig. 2.4 show the expected XY anisotropy. SEMs of <111> and <100> Si etched with and without agitation of the sample are shown in Fig. 2.5. The <111> samples do seem to show a small z anisotropy on the left hand side.

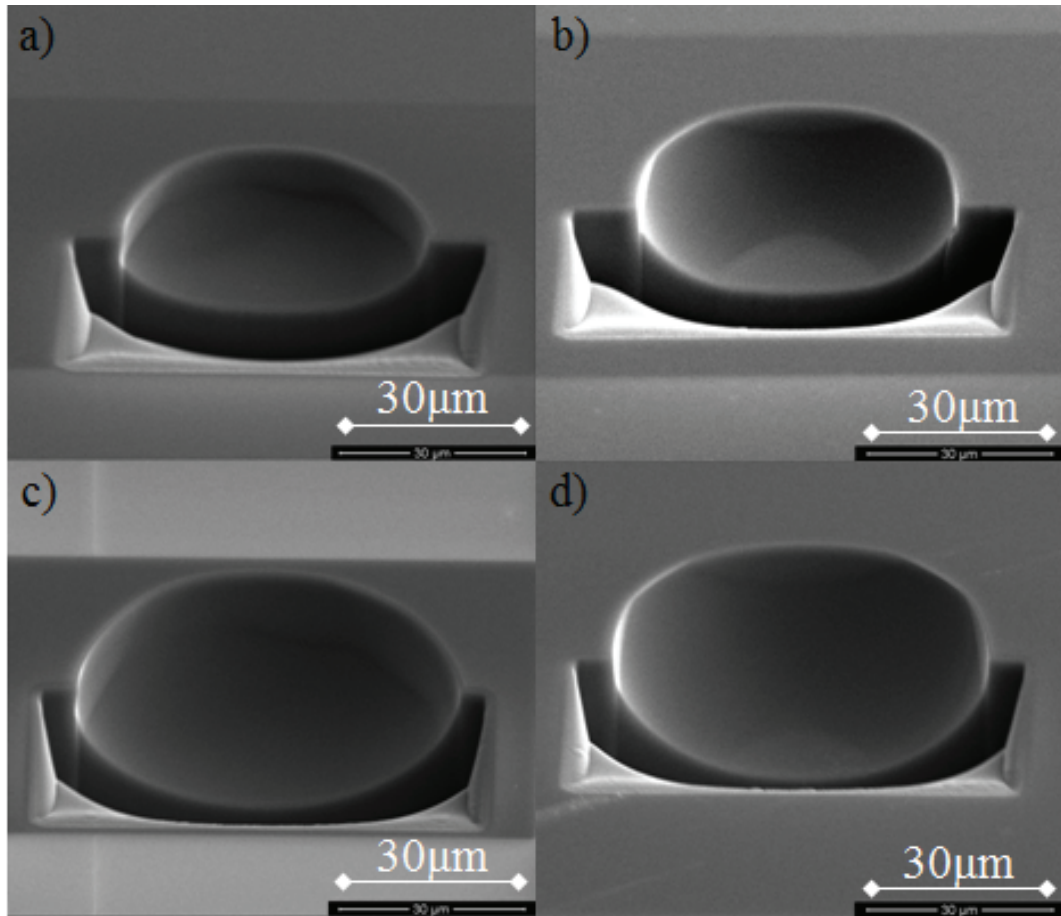


Figure 2.5: SEMs of HNA profiles with cross-sectional cut performed on FIB. Top(a,b): without agitation, Bottom(c,d): ultrasonic bath; Left(a,c): $\langle 111 \rangle$ Si, Right(b,d): $\langle 100 \rangle$ Si.

2.1 HNA Etching Design of Experiment

A full study of the side-by-side HNA etching of $\langle 100 \rangle$ and $\langle 111 \rangle$ single crystal silicon was performed, with the following etch parameters:

Si orientation	$\langle 100 \rangle$, $\langle 111 \rangle$
Etch window, d	20 μm , 30 μm , 40 μm , 50 μm
Chemical ratio	1:2:0, 1:1:0, 2:1:0, 3:1:0, 4:1:0, 2:1:1, 2:1:2, 2:1:4, 4:2:1, 8:2:1 ($HF : HNO_3 : H_2O$)
Agitation	None, random (by hand), ultrasonic bath
Temperature	RT, 40°C, 50°C, 60°C

This is obviously an enormous variable space. It was somewhat reduced by first performing the etch experiment without the temperature variable. The second design space, with the temperature variable was then performed for only hand agitated samples, and without the 2:1:2 and 2:1:4 chemical ratio etches, which were too slow to show any appreciable etching in the previous stage. The chemical ratios tested are shown in Fig. 2.6 by the red dots.

The etching experiments were carried out by first depositing a LPCVD stoichiometric nitride mask on $\langle 100 \rangle$ and $\langle 111 \rangle$ single crystal silicon wafers, patterning etch windows and dicing the wafers into equally sized samples. One large batch of each chemical ratio mixture was then made up, and samples of each orientation were duly agitated in new batches of 100mL of etchant for each sample for 2 minutes etching time.

When the heating of the etchant was characterized some additional changes were made. Automated stirring of the solution was included for etchant uniformity

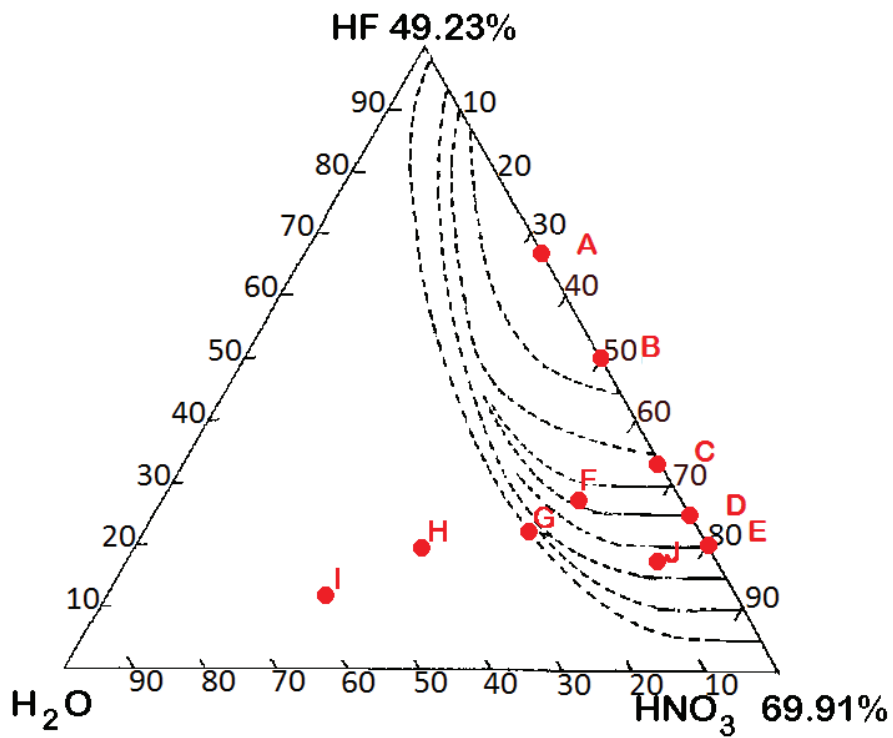


Figure 2.6: HNA etch chemical ratios. Dotted lines show iso-etch curves (constant etch rate paths), red dots are chemical ratios tested. Innermost curve represents highest etch rates.

and thicker nitride masking layers of $\approx 350\text{nm}$ were used. Since HF obviously cannot be contained in a Pyrex vessel, and putting Teflon directly on a hot plate would be an extremely bad idea, heating of the etchant was accomplished by heating a bath of DI water on a hot plate and submersing a Teflon container in the bath.

2.1.1 Results

Results of the etches, in terms of anisotropy and roughness were measured using optical profilometry and SEM respectively. The radii defined in Fig. 2.4 were used to determine a percent preferential etching:

$$\%_{PE} = \left(\frac{R'}{R_{avg}} - 1 \right) \times 100 \quad (2.4)$$

Fig. 2.7 shows the $\%_{PE}$ for increasing nitric acid concentration at room temperature. Not only do we clearly see better isotropy for $\langle 111 \rangle$ Si, but we see that the high HF concentration etchants have less preferential etching.

Fig. 2.8 shows a trend where increasing size of the etched mold shows less anisotropy. Since all etches were done for 2 minutes, this suggests that more diffusion limited etches have higher anisotropy.

We saw that some of the etched samples, particularly those without stirring, had random samples that etched much faster than the others, experiencing ‘run-away’ etching due to the autocatalytic nature of the etch as noted in [14]. Thus, we look at the preferential etching trend for the etched radius (measured average diameter - etch window diameter divided by 2) normalized by etch window diameter. We see that the ‘runaway’ etch samples tend to have lower preferential

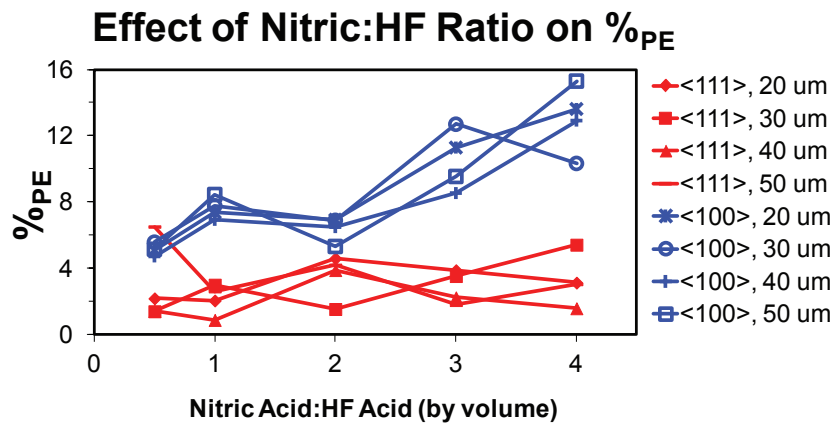


Figure 2.7: Anisotropy Vs. Chemical Ratio for HNA on <100> and <111> Silicon. Preferential etching, %PE defined as in Eq. 2.4.

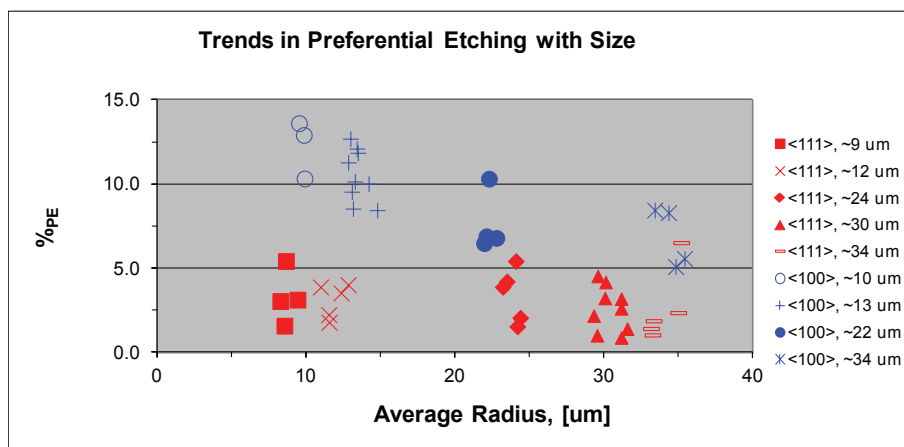


Figure 2.8: Anisotropy vs. various etched radii, where etched radii refers to (average diameter - etch window diameter)/2

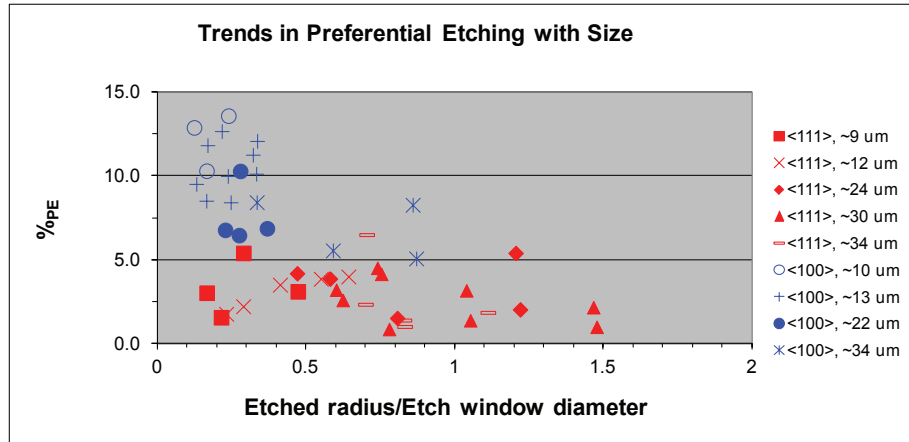


Figure 2.9: Anisotropy vs. etched radius normalized by window size

etching, and that more of these samples were seen in <111> Si. This likely has to do with the bonds seen on the different crystal planes and the required activation energy of the etch in starting the autocatalytic process. Both this and Fig. 2.7 seem to suggest less preferential etching for faster etch rates. The spread of these normalized etched radius values demonstrates the range of etch rates that we are seeing at this size scale.

Finally, temperature dependence of the etch rate was characterized in Fig. 2.10. Though mostly linear, some non-linearity was seen in the 1:2 $HF : HNO_3$ etch. However, the variance of these values is not far enough outside the expected range to be statistically significant, due to non-uniformity of the HNA etch rate over a sample.

SEMs focusing on the roughness of the HNA etch are shown in Fig. 2.11. The discrepancies between the etch window sizes and etched radii show samples that have ‘runaway’, and these samples show much smoother etching. This may partially be due to the very small etch windows used in these initial test etches severely limiting the propagation of etchant species to the etching surface.

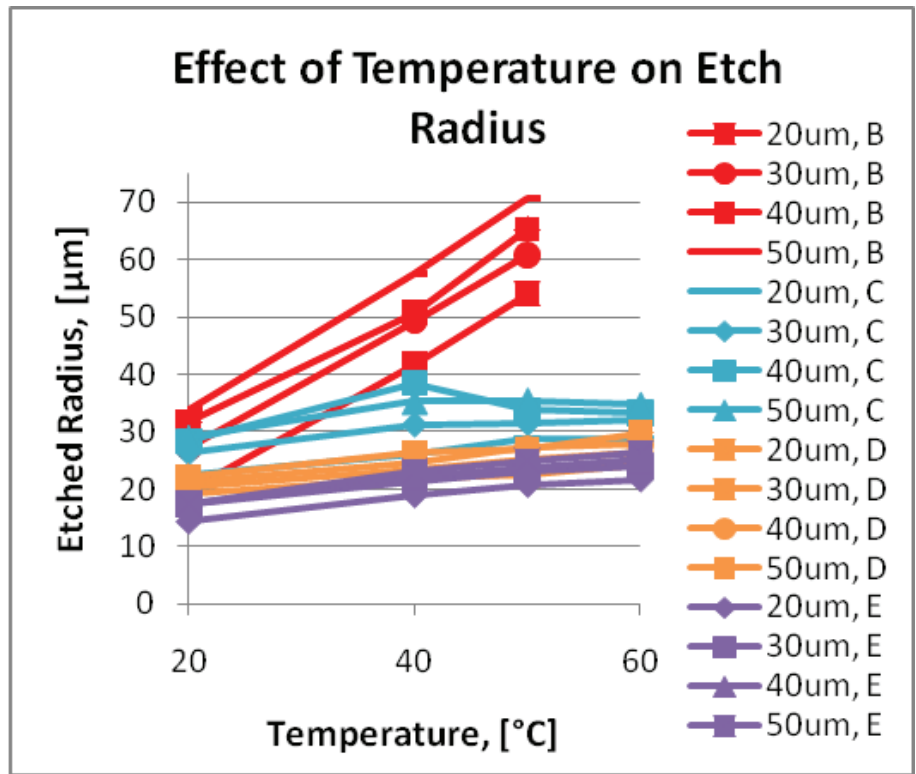


Figure 2.10: Etched radius vs. temperature on $\langle 111 \rangle$ Si samples, for etchants B-E as shown on Fig. 2.6.

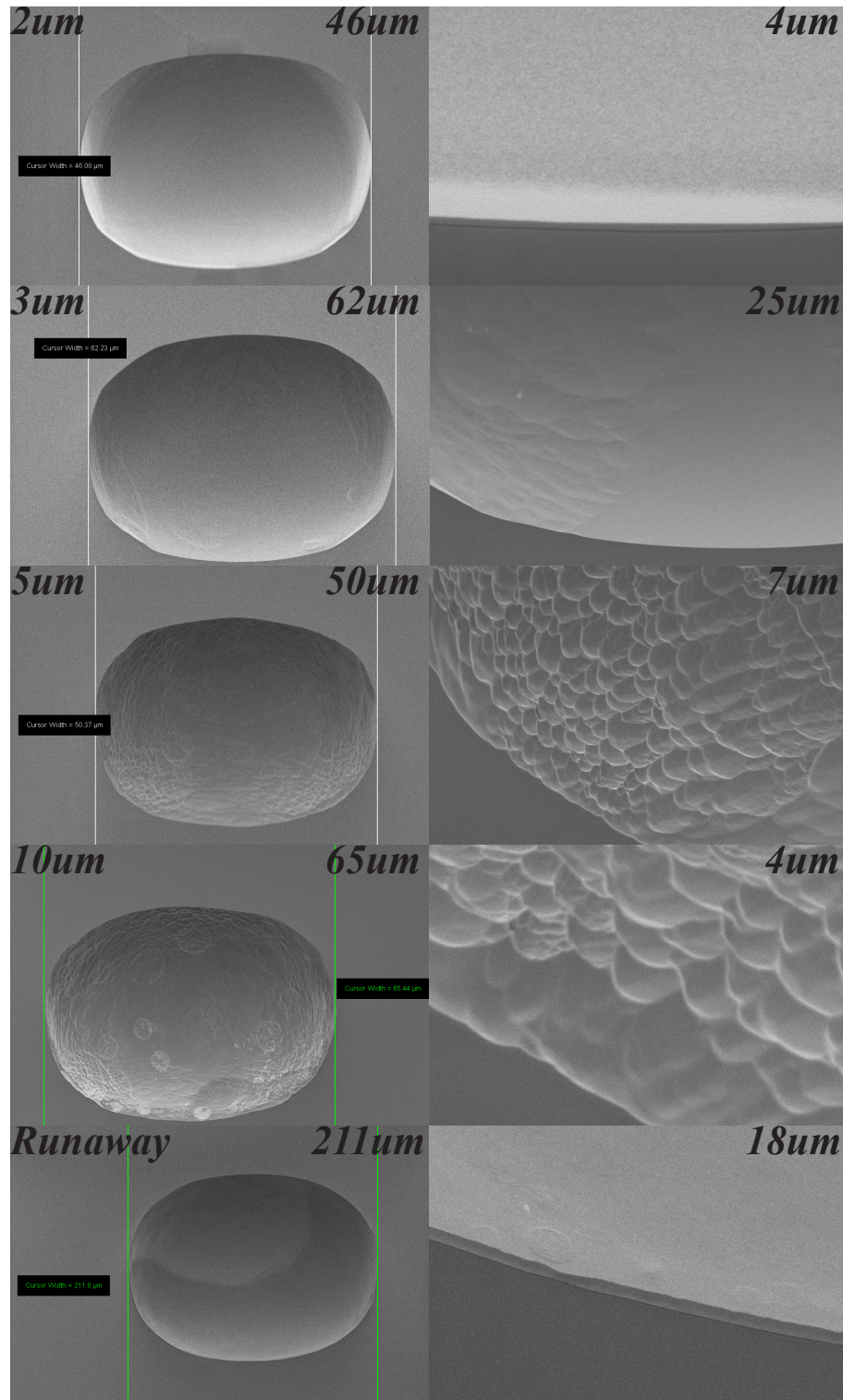


Figure 2.11: SEMs of etch roughness. Left-most dimension is etch window diameter, middle is etched radius, right is approx. width of right-hand image.

2.1.2 Masking Issues

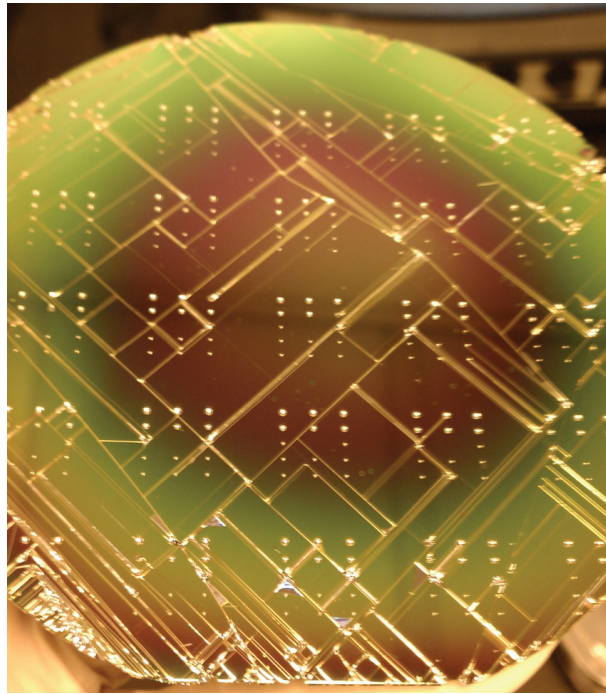


Figure 2.12: Picture of 100mm wafer with severe cracking after HNA etch.

As we moved up to doing HNA etching of entire wafers, rather than small samples, we began to see extreme cracking of the nitride mask during HNA etching, as shown in Fig. 2.12. The high tensile stress of stoichiometric silicon nitride is well

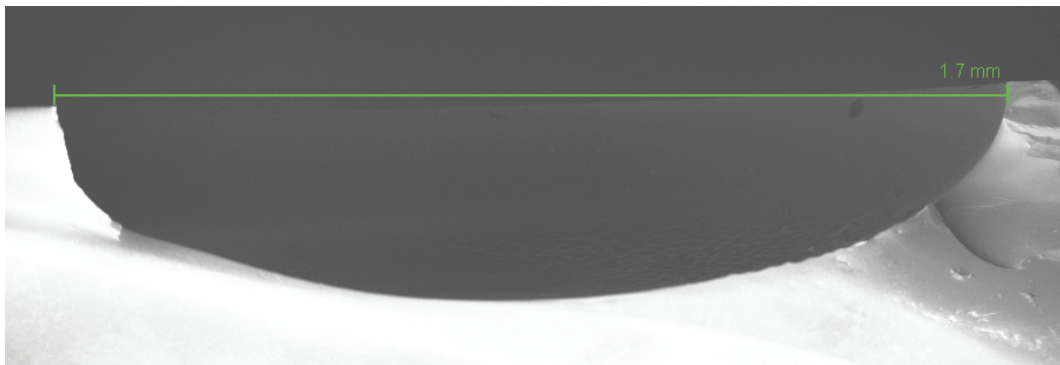


Figure 2.13: SEM of large radius etch profile. Masking selectivity and cracking issues limit depth.

known, and some nitride recipes do relieve stress, but they accomplish this by increasing the ratio of silicon to nitrogen in the LPCVD deposition. These silicon-rich nitride layers have much lower selectivity to silicon in HNA etches, and will limit the depth achievable on larger radius hemispherical molds, as shown in Fig. 2.13.

One method we implemented to get around this was to pattern trenches in the nitride mask layer around the perimeter of each sample, as shown in Fig. 2.14. This way, not only was the nitride tensile stress somewhat locally relieved by the break, but any cracks that do occur will not propagate across the entire wafer.

Not only does cracking limit the etch time, but also the finite etch rate of stoichiometric silicon nitride in HNA. The selectivity of the etch based on chemical ratio was tested by depositing a nitride layer on a test wafer and measuring the initial film thickness using spectral reflectometry. The nitrided wafer was then diced into equal size samples along with a plain Si wafer. After using calipers to measure the initial thickness of the plain silicon pieces, the nitrided and plain pieces were etched together in each of the etchant solutions, with varying number of plain silicon ‘catalyst’ pieces. The nitride and silicon thicknesses were then measured again, resulting in the selectivities shown in Fig. 2.15. A clear improvement in selectivity is seen for high HF content etchants. Though it might be assumed that the single Si catalyst piece would be the most analogous to samples being etched with small etching windows, and thus small exposed Si surfaces, the heating of etchant in this case will occur largely locally constrained to the etch window, and assuming a lower selectivity may be more appropriate.

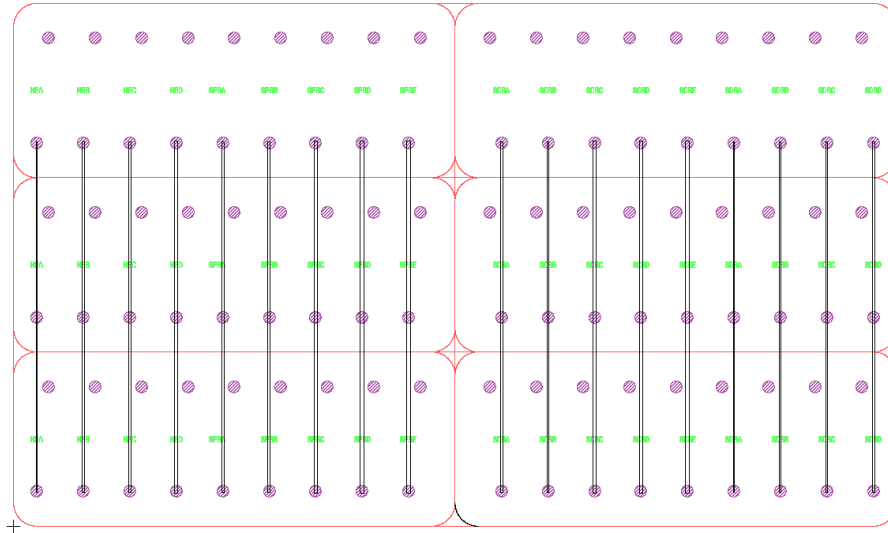


Figure 2.14: Mask trench layout for relieving nitride cracking.

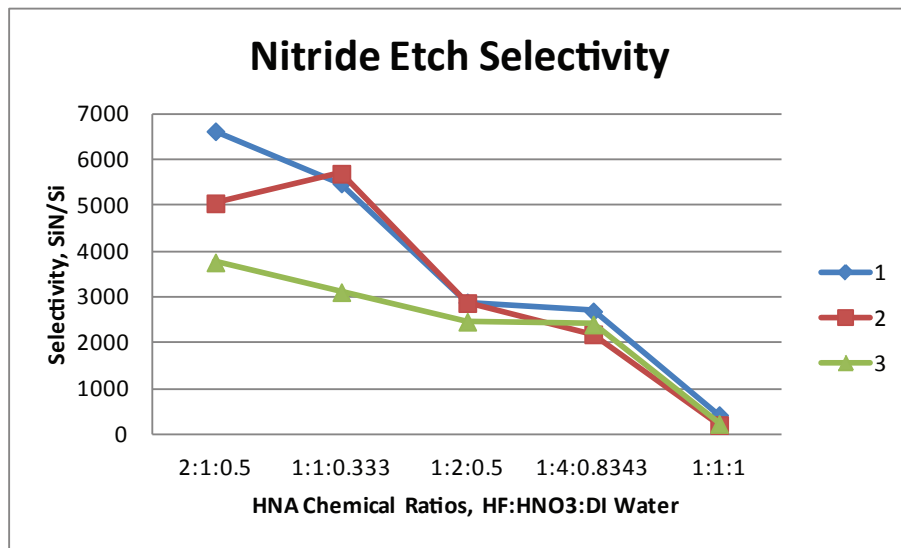


Figure 2.15: Nitride selectivity for various chemical ratios. Numbers in legend refer to number of silicon pieces co-etched with nitride masked sample.

2.2 Conclusion

In this chapter we attempted to find the smoothest and most hemispherical mold we could make based on optimization of the hemispherical mold etchant. Removing other etchants from the running for not being smooth enough, $\langle 111 \rangle$ Si was found to give the most isotropic hemispherical mold for HNA etchant. It also has the additional advantage of having odd-order azimuthal anisotropy, leading to small frequency splits for the desired $m = 2$ mode shape. However, the limits of HNA were found, and selectivity and cracking constraints require additional engineering to reach larger radii.

CHAPTER 3

ETCH MASKING

We saw in the previous chapter that we want an HNA etch which has a relatively high $HF : HNO_3$ ratio to improve selectivity to the nitride mask, as well as increasing etch rate and having improved anisotropy. However, anisotropy is still significant and poor masking selectivity compared to the amount of material we need to etch, as well as mask cracking, is limiting the etch depths we are able to achieve.

The fact that etch chemistries with faster etch rates tend to have lower XY anisotropy supports the idea that diffusion-limited etch regimes significantly increase preferential etching. If we can find a way to extend the amount of time we spend in the reaction-rate limited regime, we theorize that we can improve both anisotropy and smoothness. The specific nature of the HNA etch allows us to use what we have deemed ‘Dynamic Masking’.

3.1 Dynamic Masking

Dynamic masking makes use of two aspects of HNA etching: 1) that it is a wet etch, and 2) that H_2 gas is a by-product of the etching reaction. By fabricating concentric rings which are successively undercut by the progression of the etch, and subsequently ‘pop-off’ due to H_2 gas pressure, we can widen the etch windows to increase etchant diffusion and stay in the reaction-rate limited regime. This process is shown in Fig. 3.1. The continuous release of H_2 from the etch window openings ensures that released rings will not land back inside a mold.

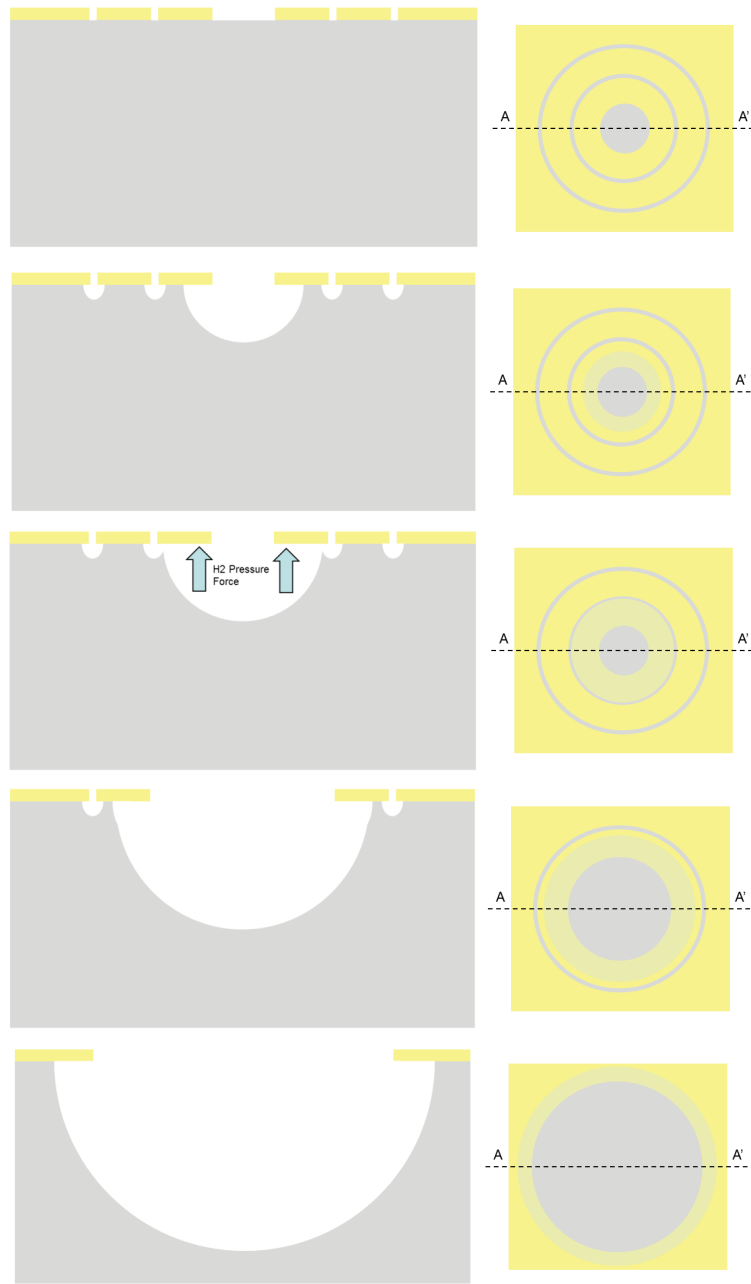


Figure 3.1: Progression of dynamic masking etch. As the silicon is etched, the undercut rings pop-off due to the H_2 gas byproduct of the etch.

Another way to think of this process is as a way to change the initial conditions of the etch. For a circular window opened on a planar surface to etch a hemispherical mold, we are attempting to approximate that planar circle to a point, and assume the depth of the etch behaves as:

$$\lim_{\frac{r}{r_{ew}} \rightarrow +\infty} \frac{r}{d} = 1 \quad (3.1)$$

where r is the radius of the etch, r_{ew} the radius of the etch window, and d is the depth of the etch. In reality, such a model is oversimplified, and fluid dynamics of the etchant and average diffusion path statistics will lead to faster vertical etch rates and a lowering of hemisphere equator into the bulk of the silicon. However, in the case of release rings, we can view the etching before a given ring is released as a pre-etch to modify the topology of the etch surface such that the initial shape after the ring is released more closely approximates a point, as shown in Fig. 3.2. Thus we are essentially making the etch window more closely resemble a pinpoint while simultaneously increasing etch rate and reducing anisotropy. Fig. 3.3 shows some examples of release ring designs. Due to the complexity of the HNA etch, it would be very difficult to calculate a best design based on diffusion lengths; instead we experimentally find the best design through an iterative process of test variables including the number of rings, the center etch window size, the ring width, and the gap width. This idea assumes that the etch rate in the center of the design is much higher than the ring gaps, and thus we suspect that a design with a large central etch window and small gap widths will be optimal.

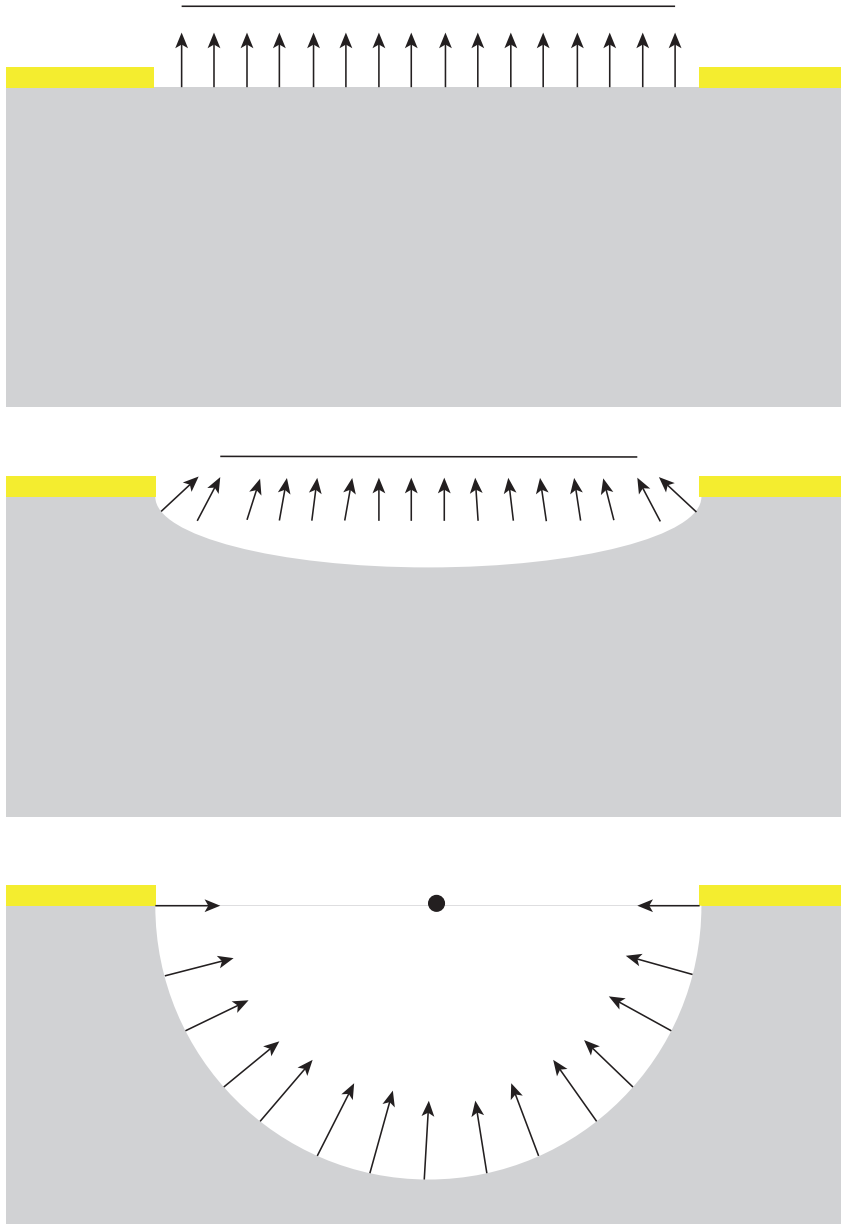


Figure 3.2: Point approximation for initial topology.

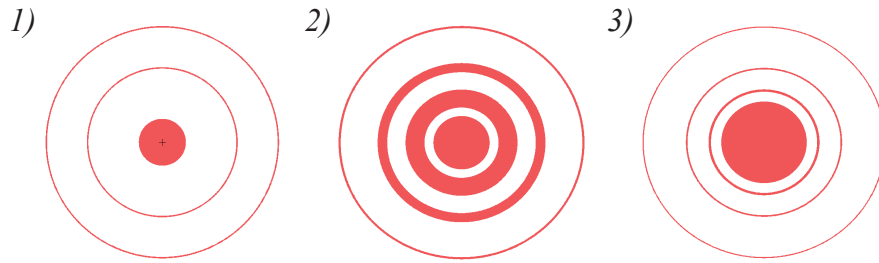


Figure 3.3: Various release ring layouts. If 1) designates a standard layout, we investigate 2) gap variations and 3) ring width variations, as well as the effect of the number of rings.

3.1.1 Results

Fig. 3.4 shows SEMs of dynamic masking (top) vs. the standard circular etch windows (bottom). We see that even though the dynamic etches were much larger, they show markedly less anisotropy and are very smooth. Unfortunately, with the designs we tried we were unable to achieve good depth, and the etches remained quite shallow. If we look at Fig. 3.5, we can see that the ring gaps used here are not limiting the etch rate enough, and thus the etch is moving laterally too quickly. This design is using $2\mu m$ gaps, which is fairly close to the resolution of the lithographic tool being used. Though the diffusion dependence might change if we use a slower etch, we will just end up trading off selectivity. If we use smaller outer radius ring designs, and etch longer after the final ring is released we may achieve depth, but will be going back into the diffusion-limited regime, and return to XY anisotropy issues. Instead, we will look at another masking technique which we call compensation masking.

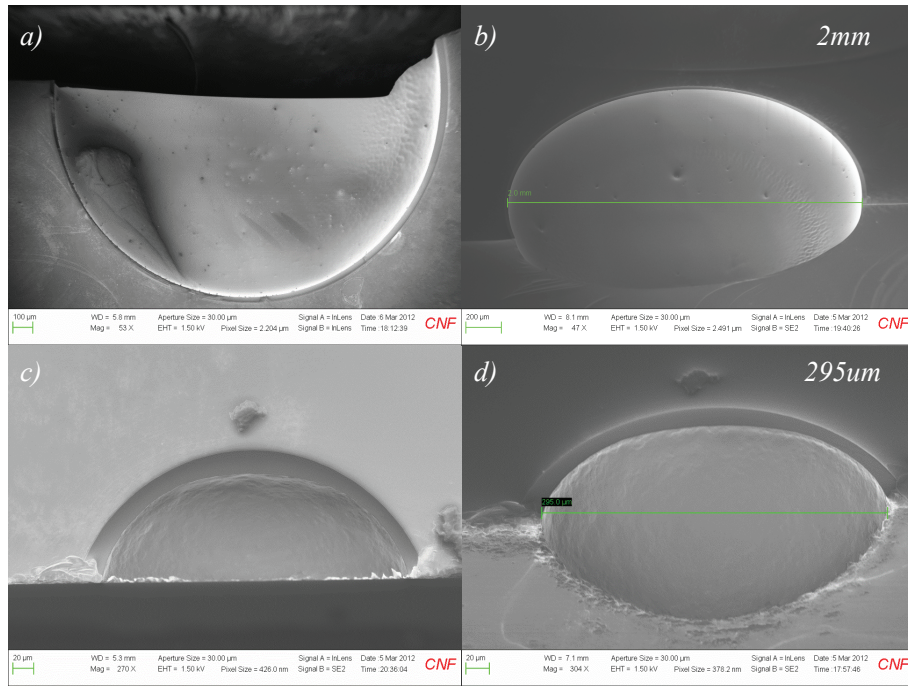


Figure 3.4: SEMs comparing dynamic and regular masking. a) and b) show dynamic masking results, c) and d) show standard circular mask etch results.



Figure 3.5: SEM of dynamic masking for 2 minute etch in 1:9 $HF : HNO_3$. Release ring design used shown in upper right.

3.2 Compensation Masking

The anisotropy of the HNA etch is dependent on the crystallographic planes, and thus is a deterministic error. If we know what the end anisotropy will be, we can remove it by compensating for it in the mask design.

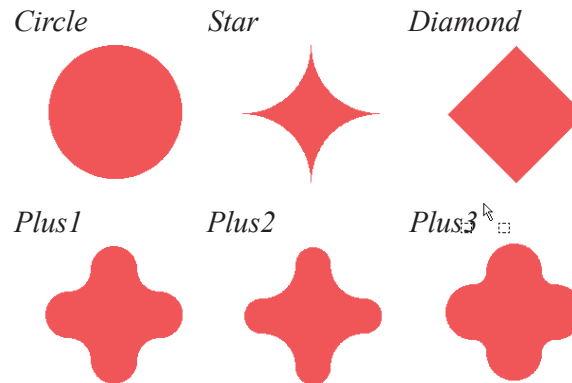


Figure 3.6: Initial designs for compensation masking. Circular masks included for baselining.

By finding and aligning our mask to the crystallographic planes in the wafer, creating mask designs such as those shown in Fig. 3.6, we can find a mask which will give an isotropically circular XY etch profile for a given radius. The continued effect of the mask shape on the diffusion lengths will tend to counteract the preferential etch rates and relax the determination of the appropriate etch radius for a given mask design.

3.2.1 Orientation Alignment Marks

Aligning to the crystallographic planes is a simple process of growing an oxide mask, etching successively rotated rectangles along the edge of the wafer, and then

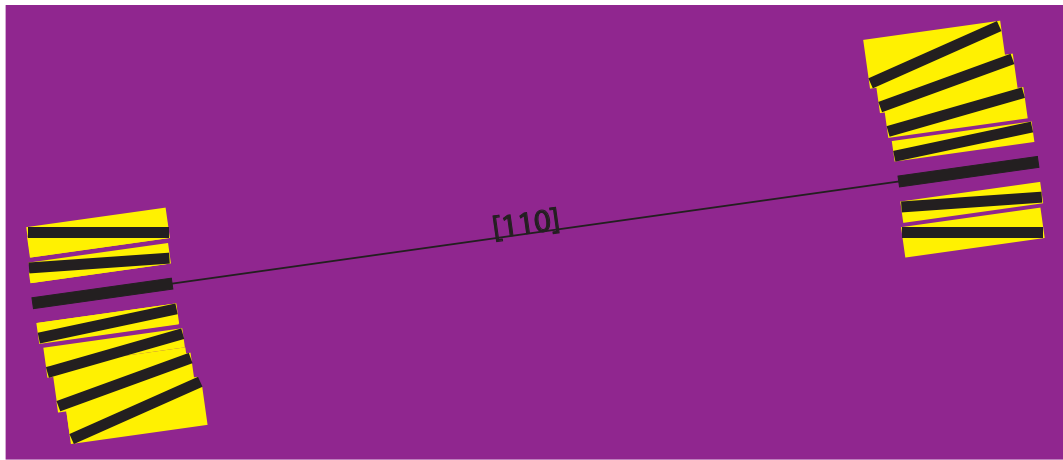


Figure 3.7: Diagram of orientation alignment mark concept. Yellow areas denote undercut oxide mask.

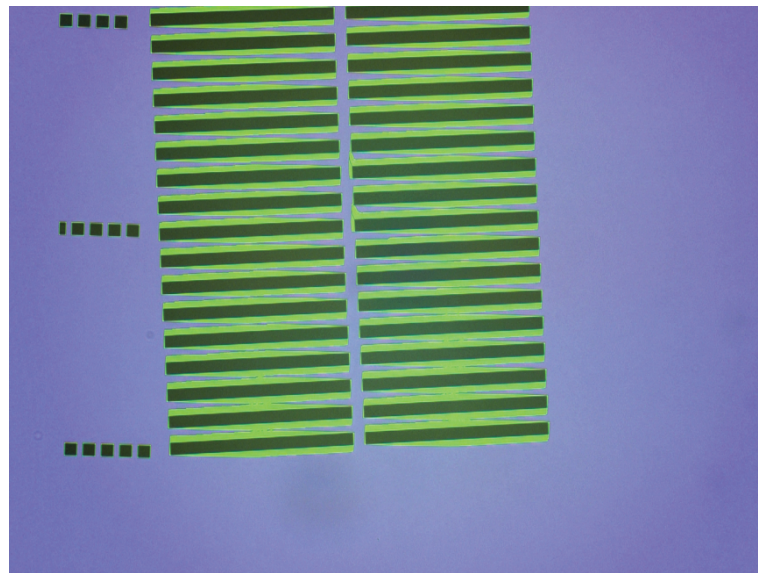


Figure 3.8: Orientation alignment marks after 20 minute KOH etch at 78°C.

etching in KOH. The set of rectangles with the smallest etched footprint will then denote the [100] axis, as shown in Fig. 3.7. An example of such etched alignment marks is shown in Fig. 3.8. We see that the difference between successively rotated rectangles is rather difficult to derive. Though the difference in rotation angles for this case is only 0.0625° , a non-zero aligned underetch made it impossible to determine the crystallographic orientation down to such a degree, and the resolution was instead limited to approximately 0.25° . This could be improved by use of a differential scheme, such as that used in [17]. While this process is not compatible with $\langle 111 \rangle$ Si due to the inability to etch the orientation alignment marks, this is no loss since the XY anisotropy is removed anyway and $\langle 100 \rangle$ Si has better Z anisotropy.

3.2.2 Results

Fig. 3.9 shows the etching results for the initial compensation mask designs from Fig. 3.6. We see that the nitride tensile stress is again causing issues, and as we would expect, cracking was an issue for any mask which had smaller positive radius of curvature than negative.

Using this to design the next group of compensation mask designs, we were able to achieve masking with a 0% incidence of critical mask cracking over 18 samples, each with 5 etch windows. Optical profilometer measurements of these designs are shown in Fig. 3.10.

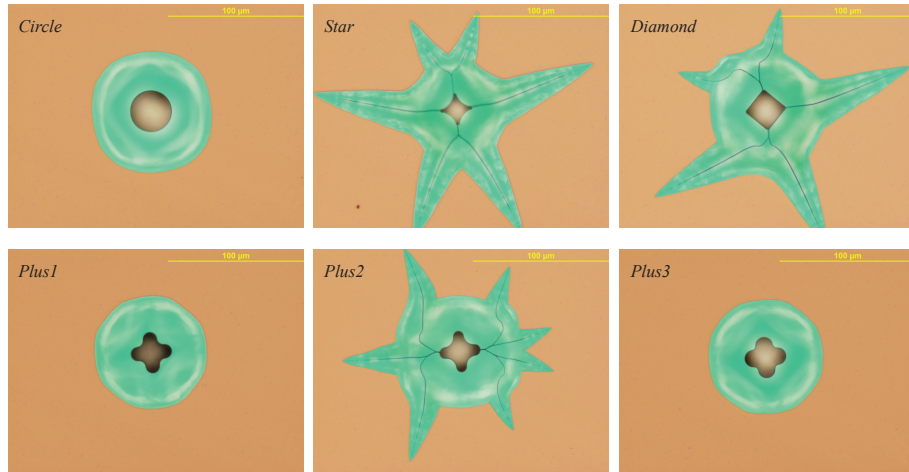


Figure 3.9: Resulting compensation masking etches. Green areas denote areas of undercut nitride mask.

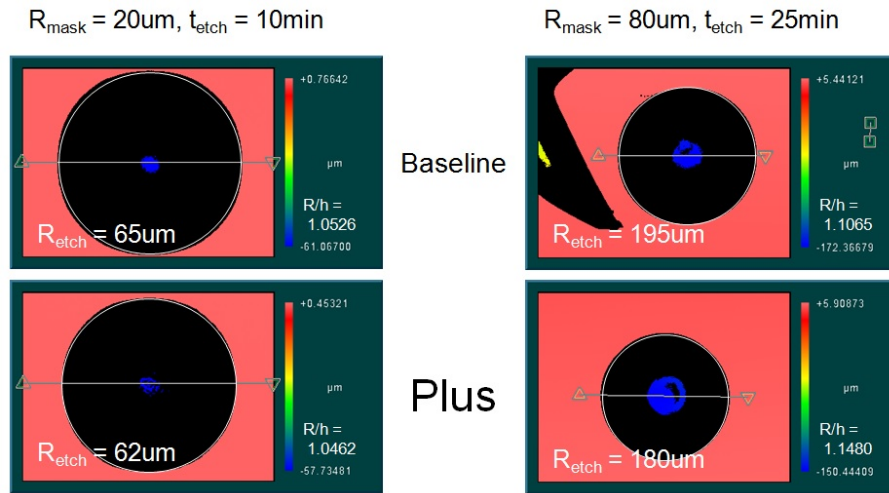


Figure 3.10: Resulting compensation masking etches for the final mask iteration measured with optical profilometer. White circles are used to elucidate anisotropy.

3.3 Conclusion

In this chapter we looked at methods of modifying our mask design to improve achievable radius and isotropicity of the hemispherical mold etched with HNA. Dynamic masking allowed us to get small improvements in the size of devices created and their XY anisotropy, but leads to a natural trade off between depth and anisotropy. Compensation masking allows us to get very isotropic hemispherical molds, and by designing masks which relieve the tensile stress of the nitride masking material, very smooth, very isotropic molds for radii up to, and not limited to, $180\mu\text{m}$ have been etched.

CHAPTER 4

DEVICE FABRICATION

We now have a hemispherical mold with low anisotropy and good smoothness. The next step is to deposit our device material, pattern the lip and release our device.

Our initial choice for the device material was another LPCVD deposition of stoichiometric silicon nitride. It has both excellent mechanical and optical properties, and is readily available in most fabs. Our initial devices, those of small radius as shown in Fig. 4.1, were successfully fabricated, and were some of the first ever microfabricated hemispherical shell resonators. However, there were two main reasons that we migrated to a new material: 1) as the radius of the shell increased, we began to see cracking inside the shell, as in Fig. 4.2, and 2) more fundamentally, the HF component of the HNA etch used to release the devices degraded the optical properties of the nitride in proportion to the etch time. Other release etches were tried, such as XeF_2 or KOH, but the selectivity was not high enough to nitride.

The smaller hemispherical shell devices were tested, as covered in the following chapter on experimental results, but these devices were more a proof of concept than our goal; we still needed larger radius devices with lower resonance frequencies. We thus switched to a thermal oxide device layer. These device have exceptionally high selectivity to XeF_2 , and though optical and mechanical properties are not quite as high as stoichiometric silicon nitride, they are still higher than polysilicon or other competing materials.

Initial oxide devices still had some issues obtaining a high enough optical quality factor; theorizing that it was related to the roughness of the etch on the rim of

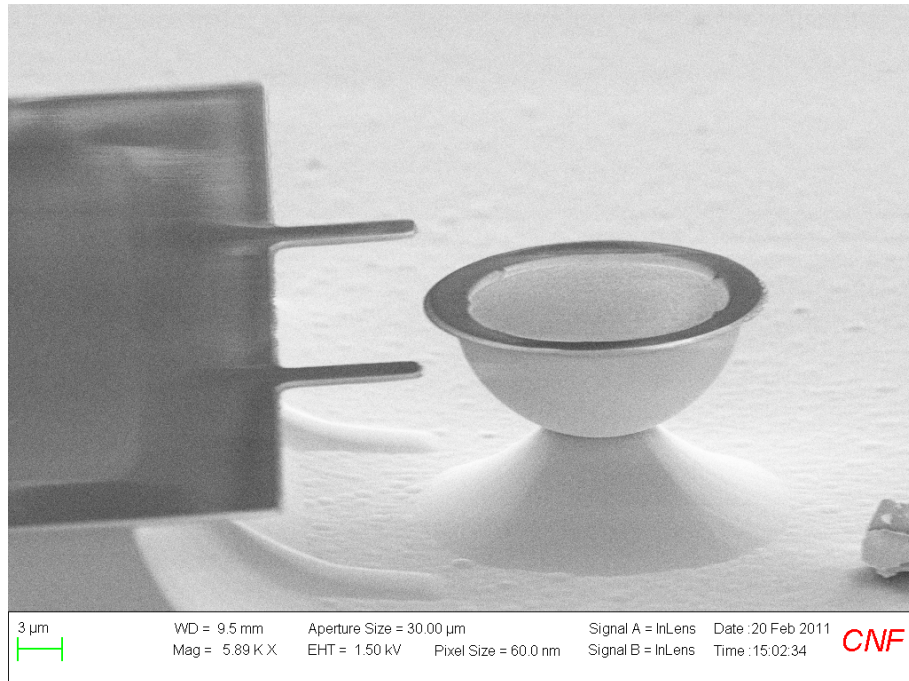


Figure 4.1: SEM of first GOBLiT. Device diameter is $\approx 20\mu\text{m}$, platform is for taper stabilization.

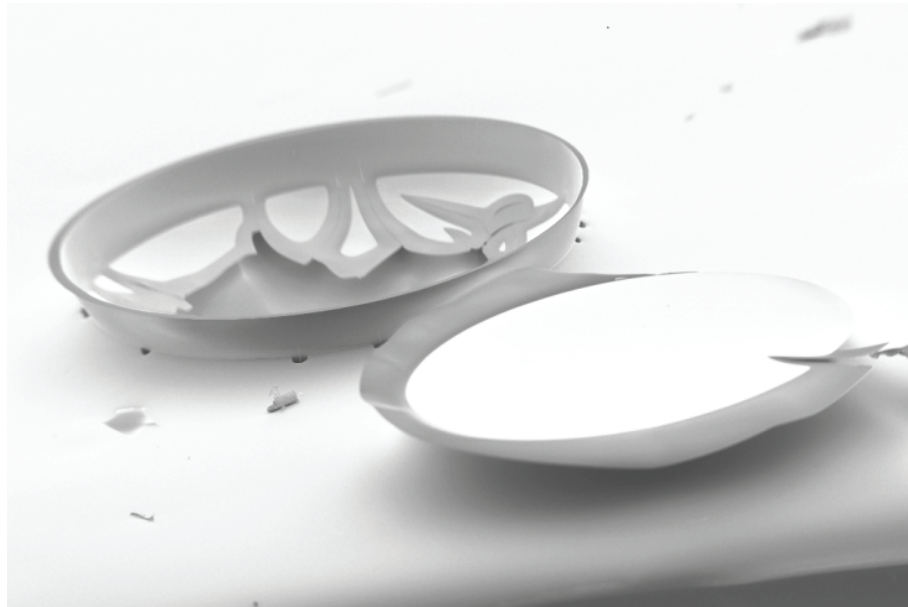


Figure 4.2: SEM of cracked nitride GOBLiT. Device diameter is $\approx 1000\mu\text{m}$.

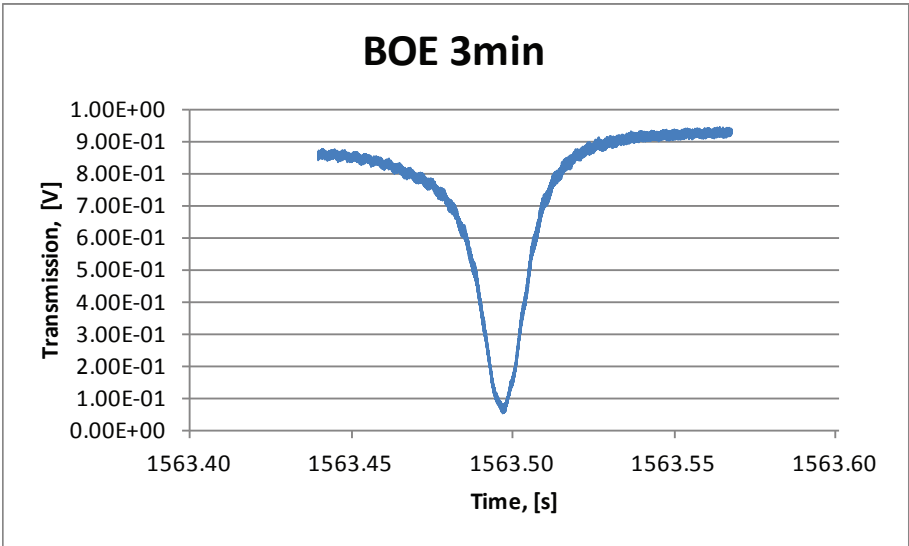
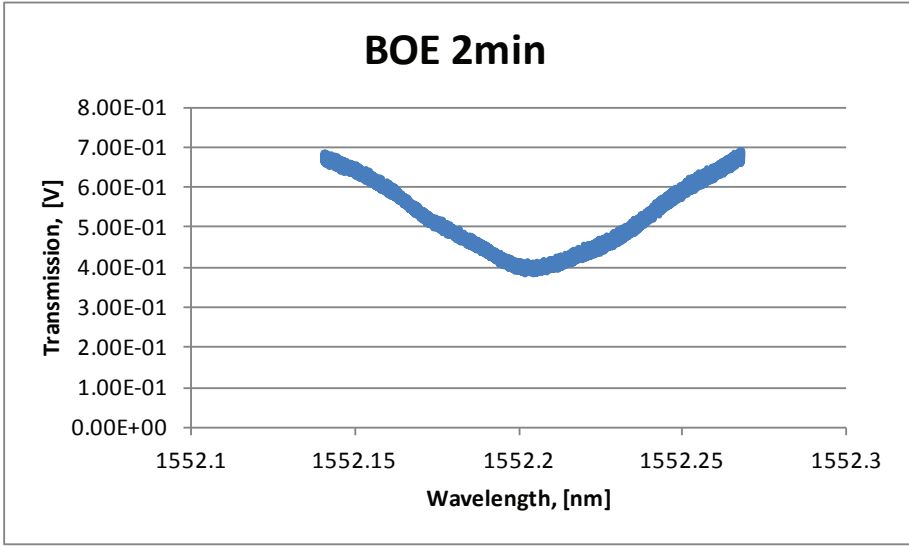


Figure 4.3: Optical Qs for BOE etched oxide GOBLiTs. $R \approx 150 \mu m$

the device where the optical mode sits, a BOE smoothing etch was performed on devices for 2 and 3 minutes before releasing them in XeF_2 ; the resulting improved Q_{opt} is shown in Fig. 4.3.

This improvement was not as radical as we might hope, and as mentioned before in relation to the smoothing of rough hemispherical molds, a limit will be reached beyond which little improvement is seen with successive etch times. Thus we began to think about other fabrication techniques that might allow us to improve the surface smoothness of the GOBLiT lip.

4.1 Dopant Enhanced Oxidation Structures - DEOS

Our initial idea was to use a concept called dopant enhanced oxidation. This is a technique which allows the oxidation rate of silicon to be increased by as much as a factor of 3 by highly doping the silicon and then performing a thermal oxidation. The impurities and defects caused by the extreme high doping create vacancy pairs which allow the oxygen atoms to diffuse more quickly through the silicon. The oxidation rate is then increased as:

$$\frac{x_0^2}{B} + \frac{x_0}{B/A} = t + \tau \quad (4.1)$$

where x_0 is the oxide thickness, B is the parabolic rate constant, B/A is the linear rate constant, t is the oxidation time, and τ is simply a term to correct t for an initial oxide film thickness. It is the B/A term which shows a dependence on Si/SiO_2 interface reaction rate and leads to the increased oxidation rate[18].

To improve the smoothness of our lip, we proposed to use the DEO effect to define a cavity for the optical signal; by using the process flow shown in Fig. 4.6,

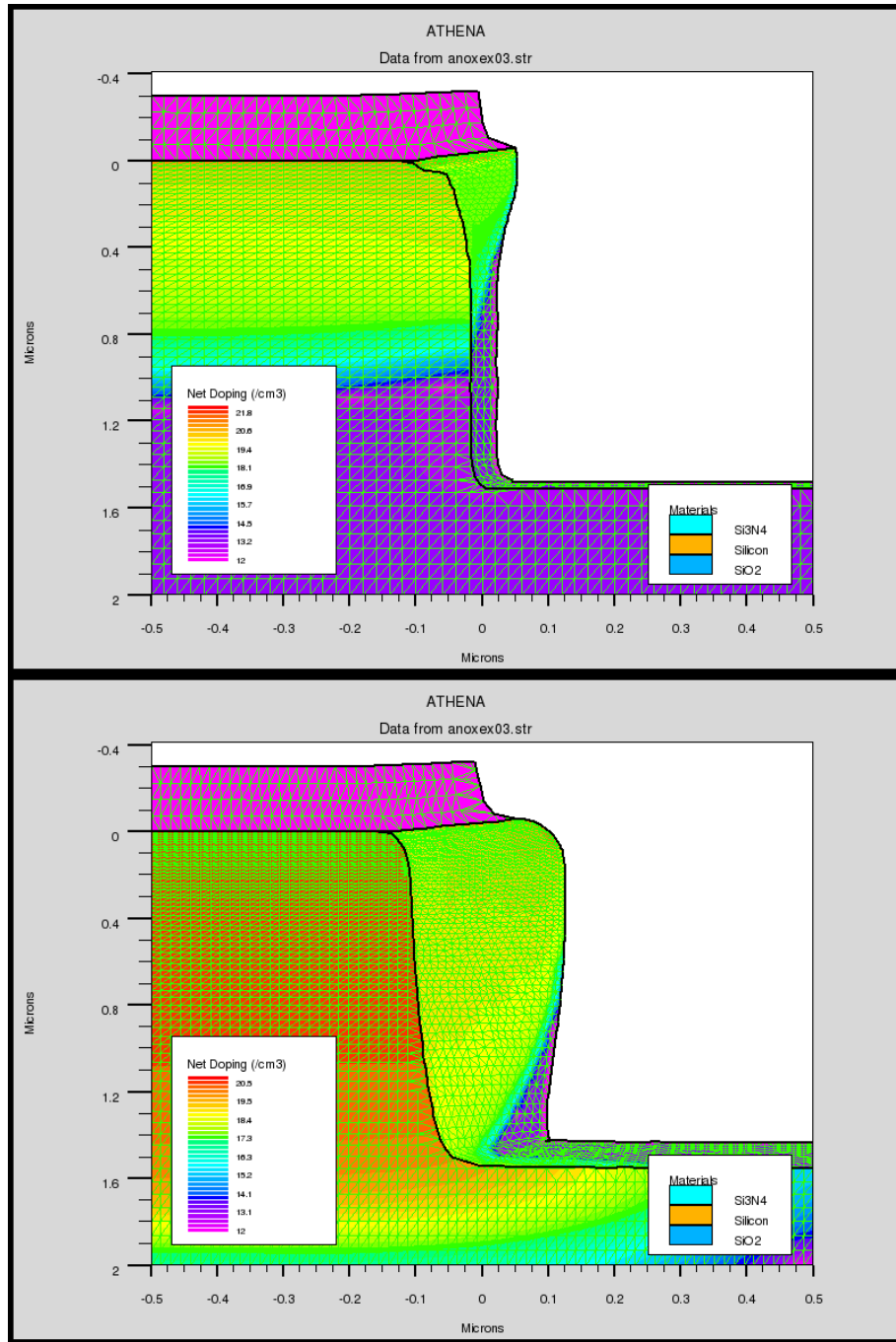


Figure 4.4: DEO simulation of oxide thickness variations in Silvaco ATHENA. Top: 900°C, Bottom: 1000°C.

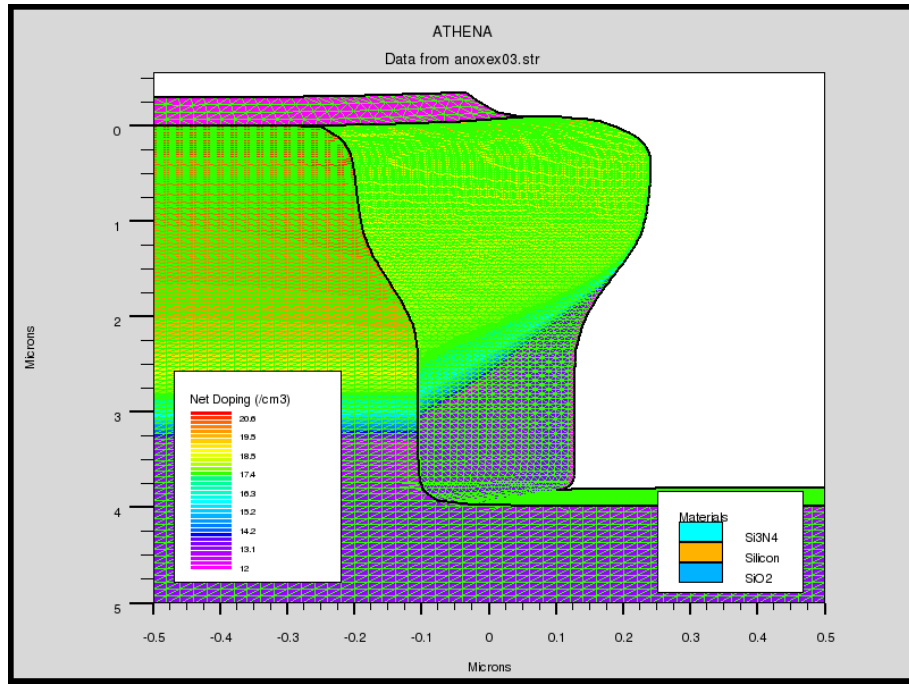


Figure 4.5: DEO simulation of 2 stage doping in Silvaco ATHENA. Stage 1: $3e^{16}P$, $1100^{\circ}C$, 20min Stage 2: $1e^{16}P$, $900^{\circ}C$, 80min

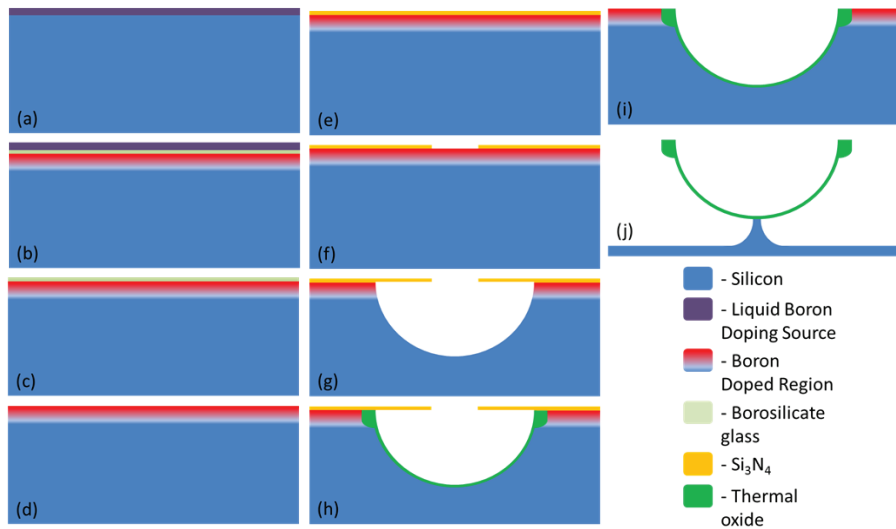


Figure 4.6: DEOS process flow. a) Spin-on dopant source, b) Heat in furnace, c) Remove dopant source, d) Remove glass by-product, e) Deposit LPCVD nitride, f) Pattern nitride for hemispherical mold etch, g) HNA isotropic etch, h) Oxidize i) Remove nitride mask, j) Release in XeF_2 .

we can achieve an optical cavity which is define by a diffusion process, and thus very smooth. However, modeling of the dopant enhanced oxidation in Silvaco process modeling software showed that the parabolic rate constant dominates the enhanced oxidation rate of the linear rate constant for any oxide growth thicker than a few hundred nanometers, Fig. 4.4. Additionally, the nitride oxidation mask needed to keep the entire surface from oxidizing requires $\approx 800^\circ\text{C}$ temperatures for deposition. This means that any sharp doping profile attempted will diffuse during the nitridization, reducing the ability to contain the optical mode in the lip. Some success was found in overcoming this by using a two step doping process: 1) a first very high concentration doping is performed and then annealed such that the first few microns of the silicon surface are doped just below the onset of oxidation enhancement, and 2) a second sharply profiled ion implantation is performed, after which the nitride layer is deposited. This method reduces the diffusion gradient, and thus the spread of the doping profile to achieve oxide profiles such as that shown in Fig. 4.5.

Though this process flow has merit, and may work well with some extensive tweaking of parameters, we decided to pursue a different process flow with more guaranteed feasibility and quicker turnaround time: the Toroidal-Lip GOBLiT.

4.2 Toroidal-Lip GOBLiT

This process is quite simple, and one of the advantages to using an oxide device layer. Since common CO_2 lasers operate at wavelengths for which oxide is highly absorptive, researchers have been able to undercut oxide disks and then lase them with a defocused CO_2 laser melt the rim into a toroidal shape[19]. This provides

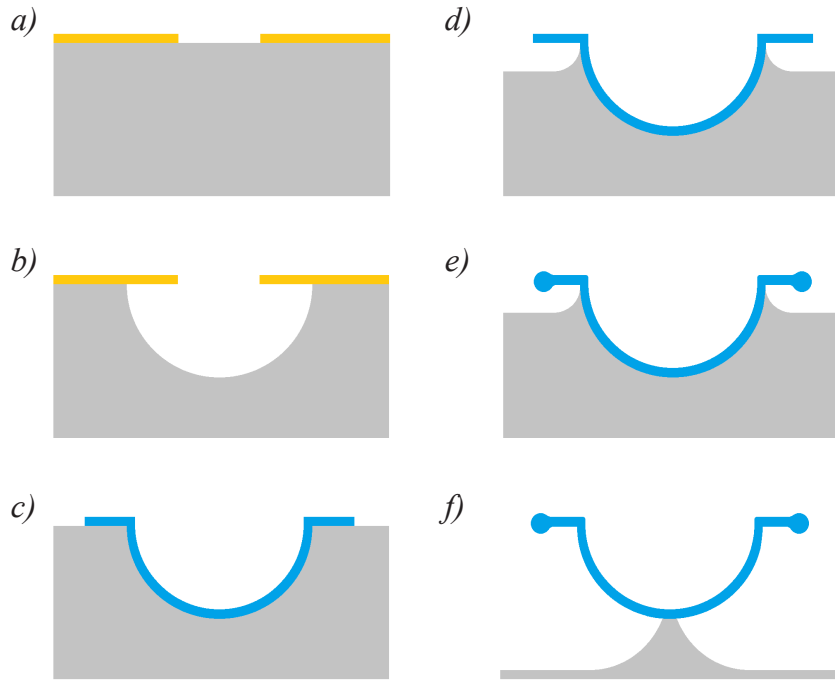


Figure 4.7: Process flow for toroidal-lip GOBLiTs. Modification to basic process flow are steps d) partial release, e) laser reflow

a very smooth surface with low scattering losses into which to couple the optical signal.

We can apply the same process to our GOBLiTs, shown in the process flow in Fig. 4.7. By undercutting up to the edge of the bowl, we can melt the toroid down close to edge of the bowl, and then further release the GOBLiT using a second XeF_2 etch. We experimentally found that allowing the undercut to progress all the way to the vertical walls of the bowl is inadvised; the melting of the toroidal shape is very sensitive to any changes in thermal path length, and any slight misalignment between the centering of the bowl and the lip to be melted can cause large thermal path length differences. This results in an unevenly melted lip, and low optical quality factor. The best achieved toroid is shown in Fig. 4.8.

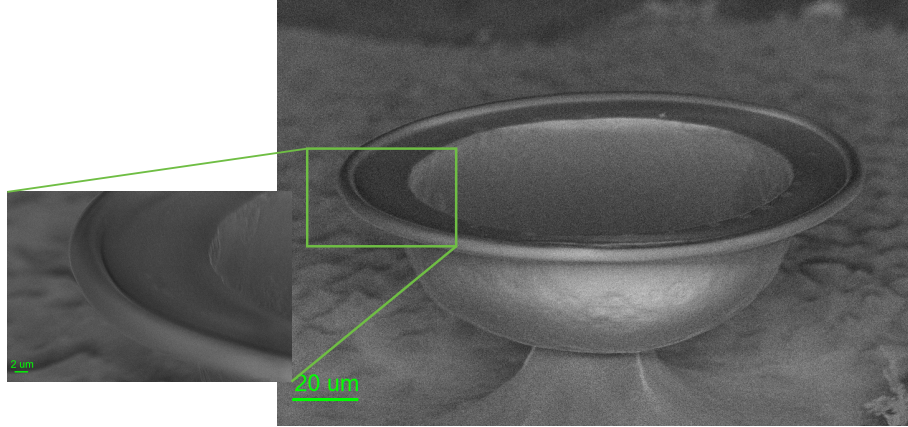


Figure 4.8: SEM of toroidal-lip GOBLiT. Inset shows very smooth lip.

One aspect of this process flow to consider is the achievable radius - even melting of the toroid requires defocusing the laser to evenly heat and melt the oxide. As the radius of the oxide device increases, the laser must be more defocused to avoid local heating. At the same time, longer path lengths around the lip for the same lip width mean that the area to be melted is much less thermally coupled, and local heating is more likely.

Looking at the device from a mechanical point of view, the melting will occur very isotropically, and will increase the stiffness of the lip out of plane. It is possible that this may actually increase frequency splitting of degenerate wineglass modes for a given anisotropy, but will need to be verified.

4.3 Conclusion

In this chapter we showed the resulting devices created from the molds optimized in the first two chapters. The need to move to oxide devices was seen due to degradation of the optical properties of nitride during the release etch. Improvement

of optical quality factors after smoothing etches in BOE lead to the attempt to modify the fabrication process to improve lip smoothness. Though simulations of a dopant enhanced oxidation based structure were not reaching the desired shape, an alternative method of smoothing the lip through laser reflow of the oxide was proposed. These toroidal-lipped GOBLiTs were successfully fabricated, and further studied in the following chapters.

Part II

Device Considerations

CHAPTER 5

SIMULATION

In most theses, the simulation chapter is placed prior to any fabrication, and is the basis for the fabricated design. However, in our case, the basic mechanical and optical models were well known and the fabrication challenges had to be overcome before structural design parameters could be controlled to the desired design parameters. A collaborative effort on the part of Prof. David Bindel and his student Erdal Yilmaz provided simulations on the effects of known fabrication tolerances for our devices, and thus the simulations shown here will be mainly those used to gain intuition into the details of the fabricated devices.

5.1 Mechanical Modeling

We will first take a look at the modeling of our structure as a mechanical resonator.

5.1.1 Basic Shape

The basic shape we are looking to achieve is a hemispherical shell: the analytical eigenfrequency calculations of such a geometry has been a topic of interest since the 1940's and 50's when it was investigated by Lord Rayleigh, Love-Federhofer-Naghdi, and Mushtari-Vlasov[20]. The particular modes of vibration that we are interested in are the wineglass modes; they are given in [21] as:

$$\omega_m^2 = \frac{2}{3}m^2 (m^2 - 1)^2 \frac{E}{2(1 + \nu)\rho} t^2 R^4 \frac{I(m)}{J(m)} \quad (5.1)$$

with

$$I(m) = \int_{\phi_a}^{\phi_f} \frac{\tan^{2m}(\phi/2)}{\sin^3 \phi} d\phi \quad (5.2a)$$

$$J(m) = \int_{\phi_a}^{\phi_f} (m^2 + 1 + \sin^2 \phi + 2m \cos \phi) \sin \phi \tan^{2m}(\phi/2) d\phi \quad (5.2b)$$

where

ω_m	mechanical resonance frequency [rad/s]
\mathbf{m}	azimuthal wavenumber
\mathbf{E}	Young's modulus
ν	Poisson ratio
ρ	density
\mathbf{t}	thickness of shell
\mathbf{R}	radius of shell
ϕ_a	longitudinal angle denoting anchor point (edge of stem)
ϕ_f	longitudinal angle denoting top edge of hemispherical shell

There is clear intuition gained from this equation in terms of the effect of geometric and material parameters on the frequency. Further, the $\frac{1}{R^2}$ dependence of frequency makes it clear why the focus of fabrication work was on perfecting the etching of a hemispherical mold: even small radial differences can lead to significant frequency splits with such a dependence.

The above equation is quite simple, and while good for providing intuition, the more complex Niordson[22] analysis of thin spherical shells was the basis for a Matlab scripted calculation of the resonance frequency, as well as calculation of

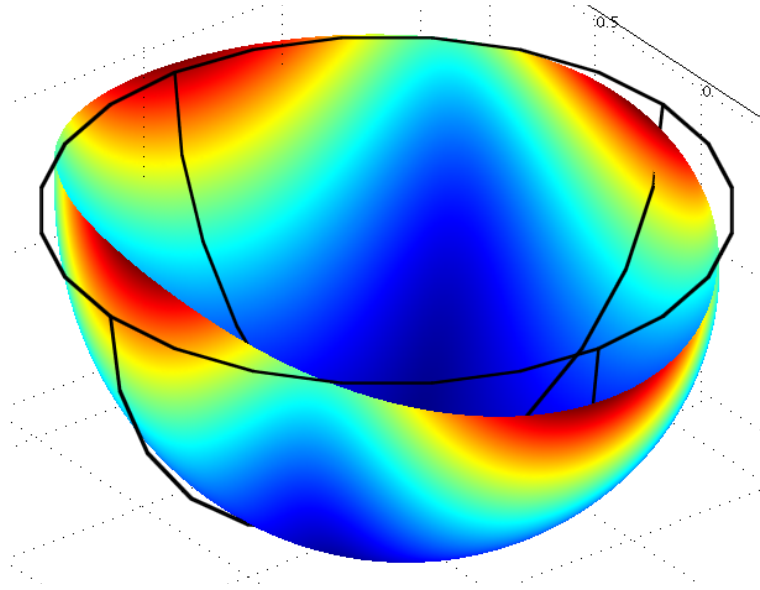


Figure 5.1: Displacement map of HSR for eigenfrequency with azimuthal wavenumber 2 as simulated in COMSOL. Finite element size leads to non-degenerate eigenfrequencies, with spacing of nodal positions = 45° , or $90^\circ/m$, and frequency spacing dependent on mesh element size and geometry.

the Bryan's factor, provided by our collaborators in the Bindel group. As a third check, finite element modeling (FEM) was done in COMSOL to check the validity of our basic analyses.

Maps of the displacement of the shell in the $m = 2$ and $m = 3$ wineglass modes as generated by COMSOL are shown in Figs. 5.1 and 5.2. It is interesting to note that finite element size of the mesh will lead to splitting of frequency values for the eigenfrequencies of a given wineglass mode. In the case of the $m = 2$ wineglass mode, this will lead to a second eigenfrequency with a nodal pattern shifted by 45° , or $90^\circ/m$, around the rim of the hemisphere. Similarly the degenerate mode for the $m = 3$ wineglass mode will be shifted by $90^\circ/3 = 30^\circ$.

Fig. 5.3 shows the difference in eigenfrequency values between the COMSOL FEM simulation and the two theoretical models used. Radii were varied as plotted,

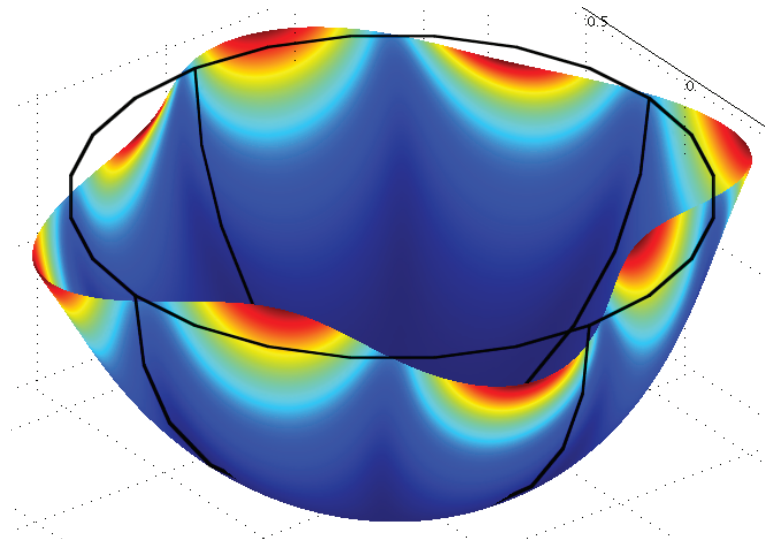


Figure 5.2: Displacement map of HSR for eigenfrequency with azimuthal wavenumber 3 as simulated in COMSOL. Finite element size leads to non-degenerate eigenfrequencies, with spacing of nodal positions = 30° , or $90^\circ/m$, and frequency spacing dependent on mesh element size and geometry.

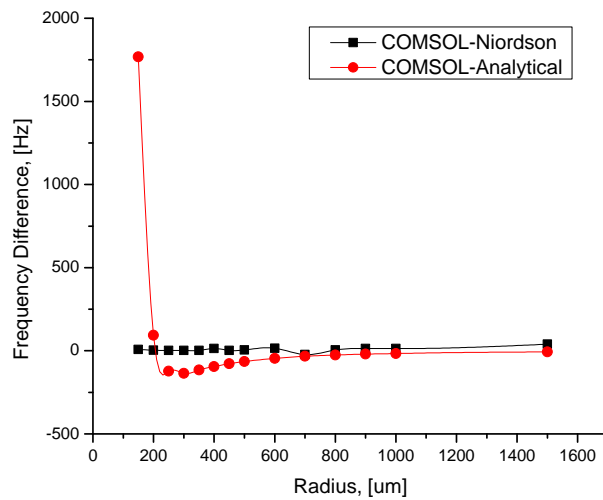


Figure 5.3: Plot of eigenfrequency differences between FEM and Niordson shell analysis (black) and between FEM and analytical expression given in Eqn. 5.1 (red) for various radii. FEM eigenfrequency is determined as the average of modeled degenerate modes.

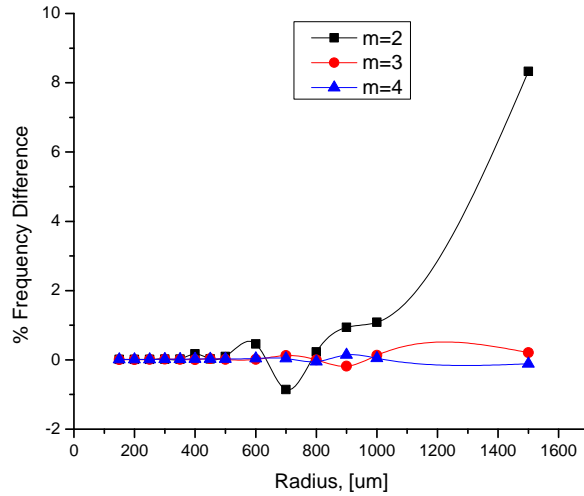


Figure 5.4: Plot of eigenfrequency differences between FEM and Niordson model for the first three wineglass modes normalized by average eigenfrequency for various radii. FEM eigenfrequency is determined as the average of the modeled degenerate modes.

while shell thickness remained 250nm: it is clear from this chart that the analytical expression given in Eqn. 5.1 breaks down at higher thickness:radius ratios, due to a thin shell approximation. The Niordson based analysis shows a better correlation to the FEM simulation, though Fig. 5.4 shows the deviation from FEM as radius is increased. This is due to decreasing resolution of the FEM simulation as computation constraints required rougher meshing.

However, this basic HSR model does not account for the lip of the GOBLiT. The lip will add mass loading and increase stiffness at the rim of the hemisphere, and needs to be simulated using FEM. Simulations of the first three wineglass modes for a GOBLiT are shown in Fig. 5.5.

The bending mode of a beam is known to have an $x^{1.5}$ dependence on the dimension in the plane of bending, and a square root dependence on the perpen-

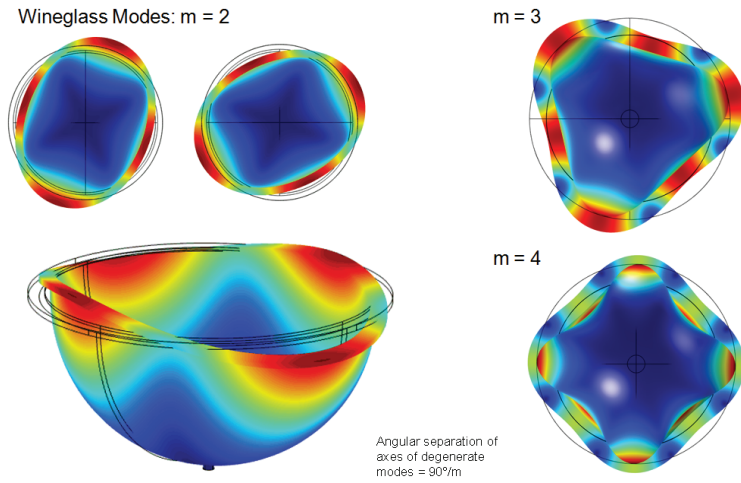


Figure 5.5: First three wineglass modes for a GOBLiT with a planar lip. Isometric view shows there is some vertical displacement of the lip as well as horizontal.

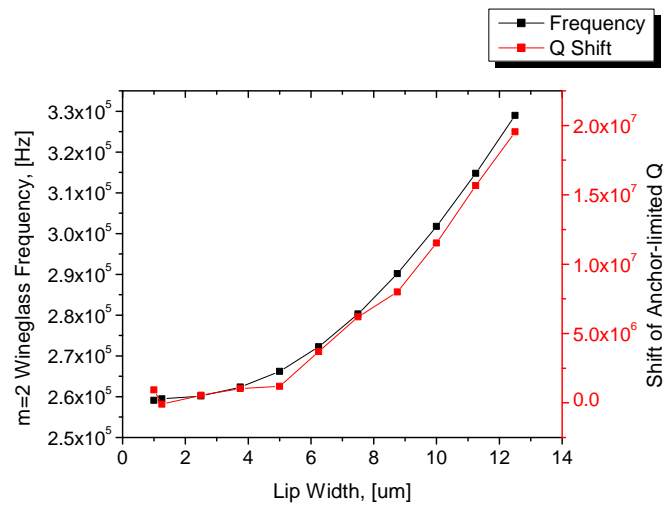


Figure 5.6: Frequency shift from a basic HSR for GOBLiTs with $R=250\mu\text{m}$, $t=2.5\mu\text{m}$, for silicon dioxide.

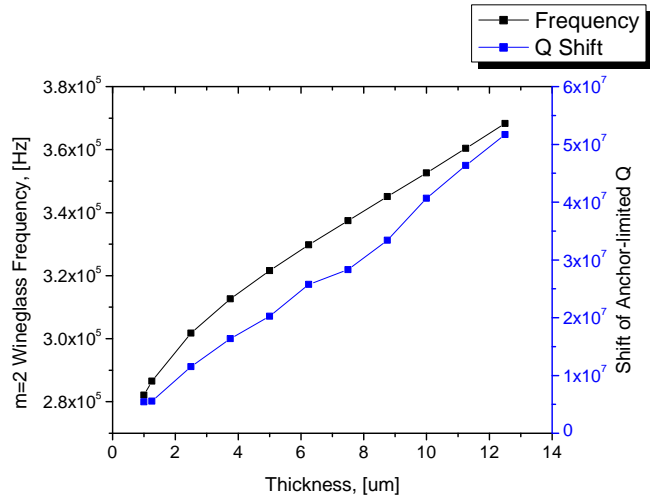


Figure 5.7: Frequency shift from a basic HSR for GOBLiTs with $R=250\mu\text{m}$, $w=10\mu\text{m}$, for silicon dioxide.

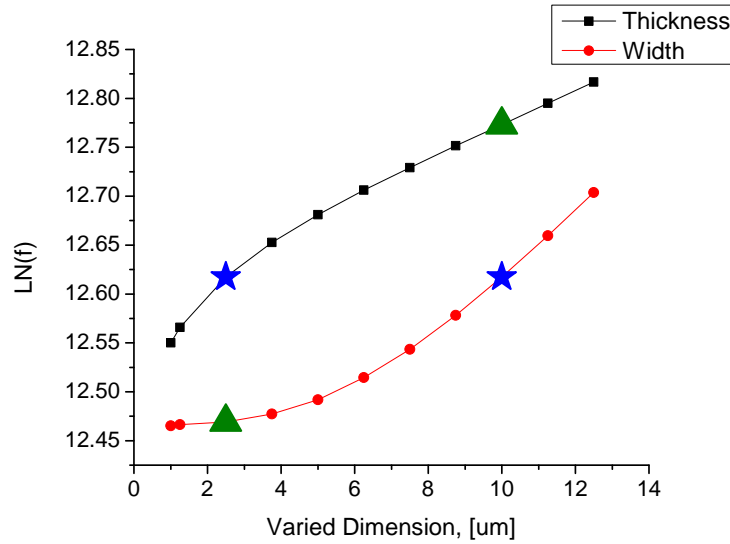


Figure 5.8: Plot of the natural log of frequency for various lip thicknesses and widths for power series analysis. Blue stars show points where the simulated geometry is the same. Green triangles show where data points where thickness and width of the lip are equal.

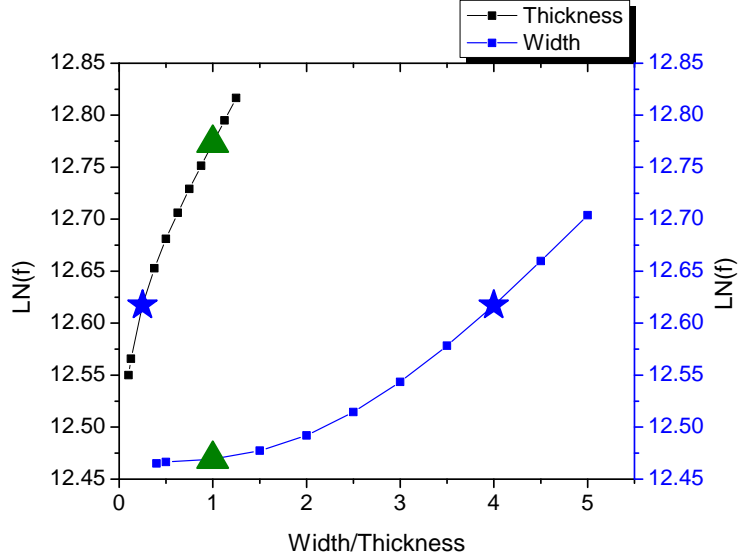


Figure 5.9: Plot of the natural log of frequency for various lip width:thickness ratios for power series analysis. Blue stars show points where the simulated geometry is the same. Green triangles show where data points where thickness and width of the lip are equal.

dicular dimension. We can approximate the lip of the GOBLiT to zeroth order to be a beam undergoing bending in the XY plane; thus if the lip is dominating the eigenfrequency calculation we expect the frequency of the GOBLiT to have an $x^{1.5}$ dependence on the width and square root dependence on the thickness of the lip. Fig. 5.6 shows the simulated frequency for various lip widths when the radius is $250 \mu\text{m}$ and the thickness is $2.5 \mu\text{m}$. Likewise, the effect of lip thickness is shown in Fig. 5.7, which shows the trend in resonant frequency for various lip thicknesses when the width is $10\mu\text{m}$.

To analyze the frequency dependence on both the width and thickness of the lip, we have to take both terms into account. By plotting the natural log of the frequency vs. the varied dimension we can see the exponential dependence as the slope of the plot, as shown in Fig. 5.8. The red line shows the case where width was varied; in this case, thickness was constant at $2.5\mu\text{m}$. The slope

is lower in the regime where thickness is greater than width, and increases as width becomes the dominant variable. Likewise, the black line shows the effect of varied thickness plotted with width constant at $10\mu\text{m}$, with higher slope in width dominated regimes. The green triangles show data points where thickness and width are equal; the blue stars show points where the geometry was the same (thickness = $2.5\mu\text{m}$, width = $10\mu\text{m}$). In the case where thickness was varied (black line), the slope hits an asymptote earlier on; this can be attributed to the fact that there is bending motion outside of the Z plane as well. The same data is plotted as width:thickness ratios in Fig. 5.9.

Both Figs. 5.6 and 5.7 also have plots of Q; these were calculated using a matched layer simulation such as that referenced in [23]. The matched layer method assumes that a substrate exists which is essentially infinite. In cases where the acoustic wavelength of the resonance is small in comparison to the actual substrate size, this is an acceptable modeling assumption to make. However, in the case of low frequency resonators such as we are modeling, the actual substrate is on the same order, or possibly smaller in some dimensions than a full acoustic wavelength. Thus the anchor loss simulations shown here are to be taken with a grain of salt. Professor Bindel, of Cornell, who has collaborated on simulations on this project is in the process of writing code which will be able to infer when this limit is reached, and until what point simulated data is still a viable source of intuition.

An observation of interest to the fabrication of wineglass mode resonators is the interaction between the azimuthal symmetry of anisotropy and the order of the wineglass mode resonance. An in depth paper on the topic has been submitted for review by Erdal Yilmaz ([24]), and the particular case of the effect of oxidation

rate anisotropy on frequency split in hemispherical shell resonators is studied in [21]. Put simply, devices with even order azimuthal anisotropy will have very small frequency split between odd order degenerate wineglass modes, and vice versa for odd order azimuthal anisotropy. Since we see even order anisotropy for HNA etching of $\langle 100 \rangle$ Si and odd order for $\langle 111 \rangle$ Si, we should be able to choose our Si substrate depending on which wineglass mode we want to use. However, the hexagonal shapes observed in $\langle 111 \rangle$ Si are not completely symmetrical, and a finite frequency split will be observed. The anisotropy in $\langle 100 \rangle$ Si is symmetrical, but since this shape will reduce $m = 3$ wineglass mode frequency split, and we expect greater displacement for the lower frequency $m = 2$ wineglass mode, we needed to explore the fabrication tools to reduce frequency splits for $m = 2$ wineglass modes.

5.1.2 Toroidal Lip Shape

The toroidal lip GOBLiT was a structure motivated by improving optical Q factors. However, intuition would tell us that it will also have some interesting effects on mechanical behavior of the device. By melting the lip down to a toroidal shape, rim width, and thus frequency, will be reduced. At the same time, increased stiffness with regards to Z axis motion of the lip should be increased. This allows us to have more effective mass at the lip, with fewer parasitic lip modes and lower frequency, which is important for gyroscope operation. SEM was used to measure the exact dimensions of a fabricated toroidal lip GOBLiT, as in Fig. 5.10. Simulating and plotting the spectrum of the eigenmodes found resulted in the initial spectrum shown in Fig. 5.11.

The desired wineglass modes in Fig. 5.11 are clearly spaced quite closely with

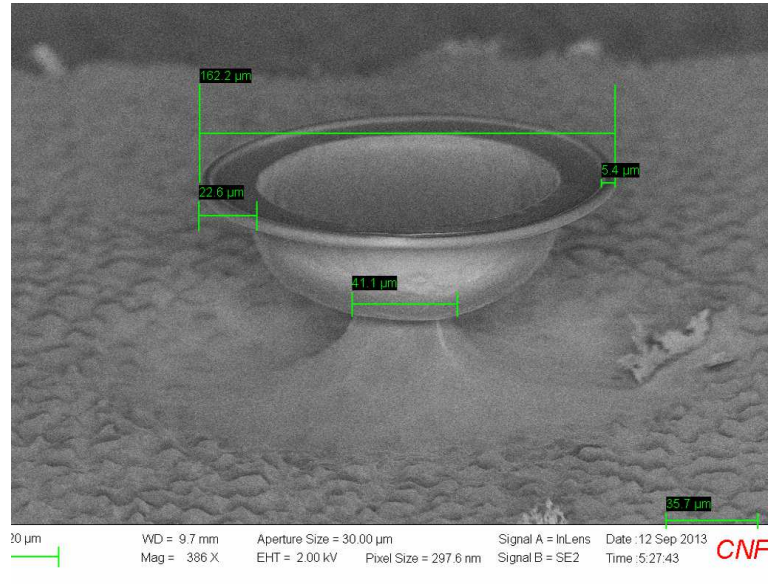


Figure 5.10: SEM of Toroidal Lip GOBLiT (TorLiT) with dimensions used for COMSOL simulation.

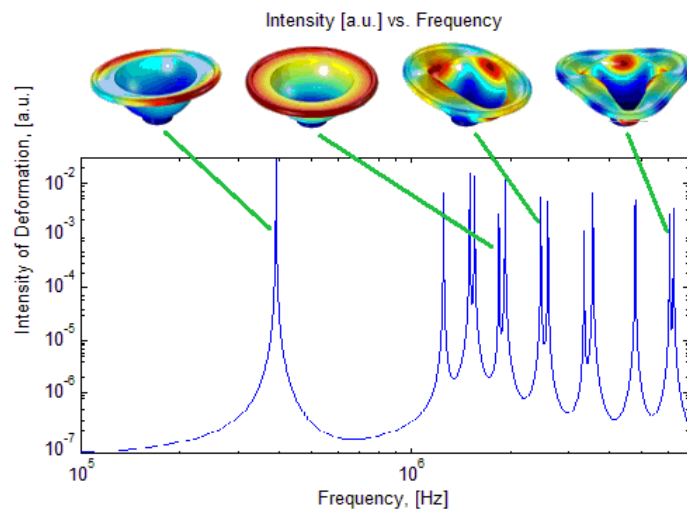


Figure 5.11: Simulated spectrum of fabricated TorLiT. Mode shapes were found using LDV, as is described in the Experimental Results section, and dimensional variables were then modified within the SEM measurement error range to match.

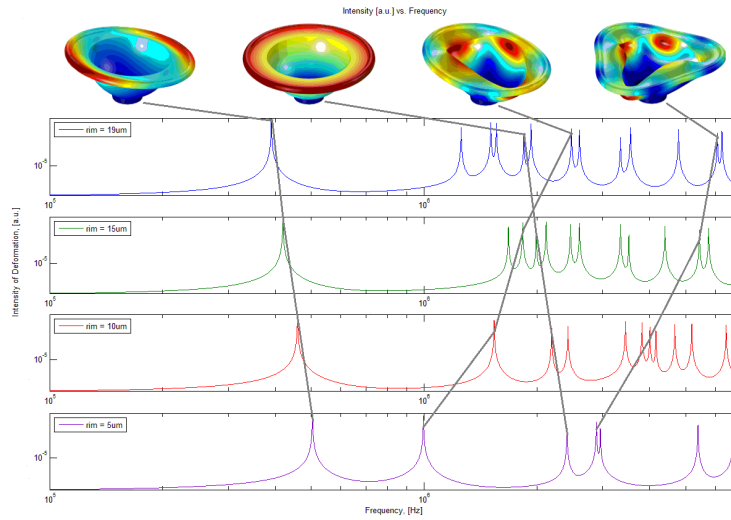


Figure 5.12: Simulated spectrums as lip width is reduced from the fabricated TorLiT value. Parasitic lip modes are forced to much higher frequencies as wineglass mode frequencies are reduced. Stem size was held constant at $12\mu\text{m}$.

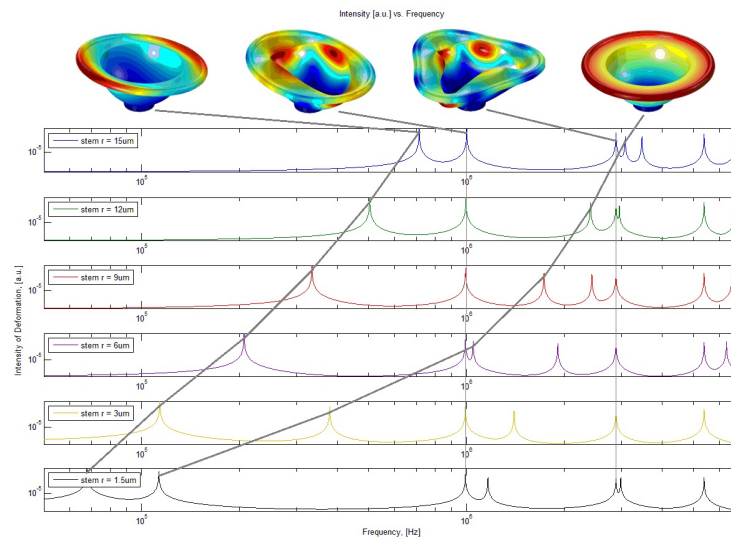


Figure 5.13: Simulated spectrums as stem size is reduced from the fabricated TorLiT value, assuming rim width is $5\mu\text{m}$. Wineglass modes show very little interaction with stem size, but radial and bowl tilting or extensional modes can be easily moved in relation.

other modes - parasitic lip flapping modes and bowl extensional modes. These modes, and their spacing to the desired wineglass modes, should be adjustable by changing the lip width (i.e. melting the toroid further), or the anchor stem width. Simulation studies of the effects of changing these parameters were performed, shown in Figs. 5.12 and 5.13. It is clear that the two parameters, lip width and stem size, can be used to easily adjust the mechanical spectra of the device.

5.2 Optical Modeling

Simulations were also performed to see the affect of structural parameters on the optical modes and coupling to the device. The variables of interest were the radius of the GOBLiT structure, and the thickness and width of the lip. Fig. 5.14 shows how the mode varies over radius and lip thickness. As radius is increased, the angle of incidence of the light as it reflects off the lip edge becomes more oblique. This results in spreading of the optical mode, further into the lip and away from the lip edge. If the lip width is not large enough, this can result in the optical mode spreading into the bowl of the GOBLiT, as shown in Fig. 5.15.

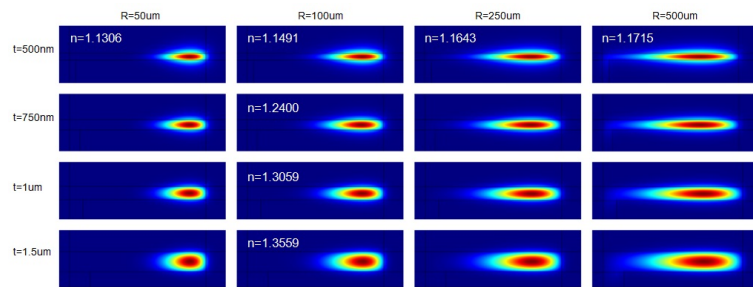


Figure 5.14: Simulated optical mode cross-sections for various GOBLiT radii and lip thicknesses. Lip width was adjusted as necessary to retain the mode in the lip.

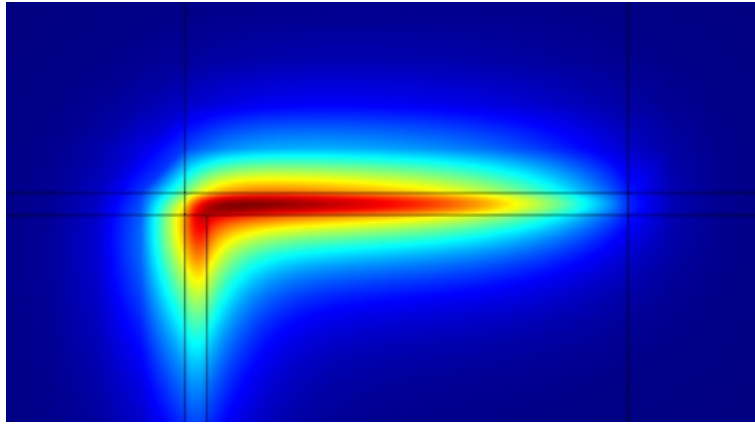


Figure 5.15: Simulated optical mode cross-section for a device structure in which the lip is not wide enough to contain the mode. $550\mu\text{m}$ radius, 300nm thickness, $6\mu\text{m}$ width.

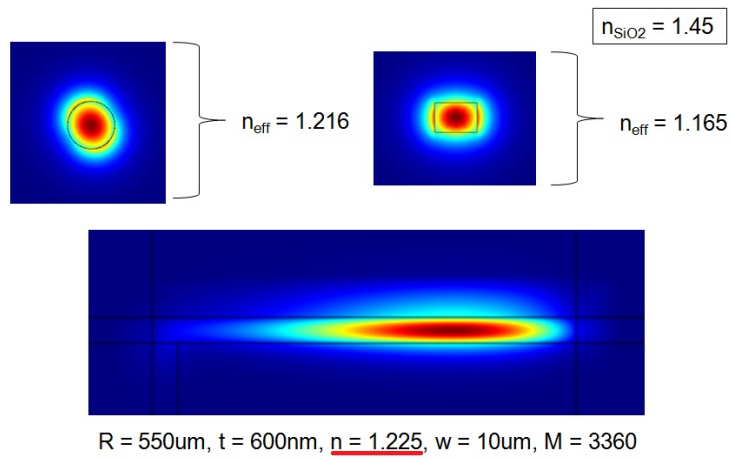


Figure 5.16: Simulated optical mode cross-sections for optical fiber taper and eventual integrated waveguides. A GOBLiT optical mode with good index matching is shown at bottom.

Lip thickness controls the proportion of optical mode which is squeezed outside the oxide lip structure, and thus shows a strong correlation to effective index of the mode. As noted in [25], the propagation constants between taper and the optical mode of the device need to match to achieve efficient excitation of the optical mode. For a system in which the losses are as yet unquantified, this means matching indices of refraction. Fig. 5.16 shows simulated optical mode cross-sections for an optical fiber taper and a waveguide structure. A possible lip geometry for a $550\mu\text{m}$ radius device which matches well to the taper is also shown.

5.3 Conclusion

In this chapter, both mechanical and optical simulation was covered. For the mechanical model, verification of the analytical equations and collaborators code was performed on the basic hemispherical shell resonator shape using COMSOL. The effect of lip geometry on the resonance frequency was also looked at, as well as the lip width and stem size effects on the toroidal-lipped GOBLiT. It was shown that melting the lip as much as possible to reduce the lip width will help remove parasitic lip flapping resonance modes from the desired wineglass mode spectrum. In optical simulations we saw that larger radius devices will have more spread out optical modes, and changing the shape of the lip is required to keep the optical mode at the edge of the lip where it is easily accessible by taper, as is achieved by the toroidal-lipped GOBLiT structure.

CHAPTER 6
EXPERIMENTAL RESULTS

6.1 Optical Transmission

The first step to characterization of a structure for use as an opto-mechanical device is to look at the optical transmission. Picking the wavelengths at which to pump and at which probe the device require knowledge of the optical quality factors and extinction ratios of the optical modes for a given input power.

Optical transmission of fabricated devices was tested using a setup as shown in Fig. 6.1. Polarization of the optical signal is controlled using the polarizer, while the two attenuators allow the power at the device to be changed while maintaining full-scale output at the photodetector (PD). Variable wavelength semiconductor lasers in the range of 1300 and 1550 nms were used. The light sent through the optical fiber interacts with the device by using a taper fiber scheme, such as that described in [25].

To create the fiber taper as shown in Figs.6.2 and 6.3, the plastic casing is first removed from a short length of single mode optical fiber and clamped onto two

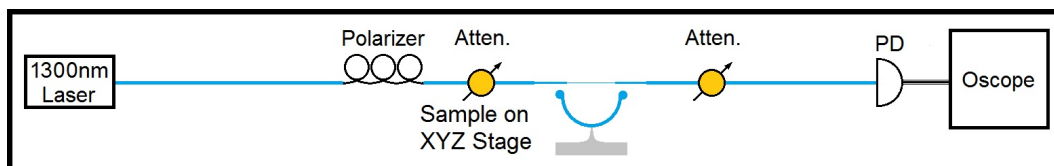


Figure 6.1: Coherent light from a semiconductor laser source is sent via optical fiber through a polarizer and attenuator to interact with the device via evanescent coupling from a tapered fiber section. The modified signal is then attenuated as needed for full scale detection at the avalanche photodiode, and detected via oscilloscope.

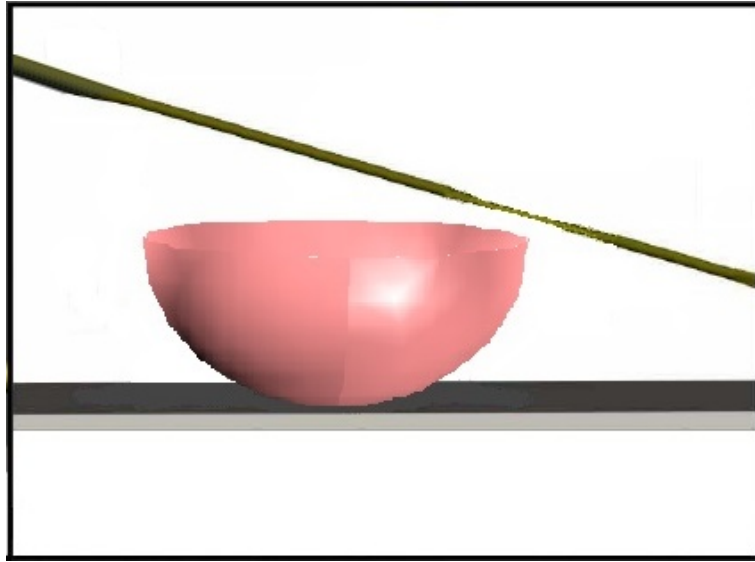


Figure 6.2: Diagram of a tapered fiber interacting with an optical device.

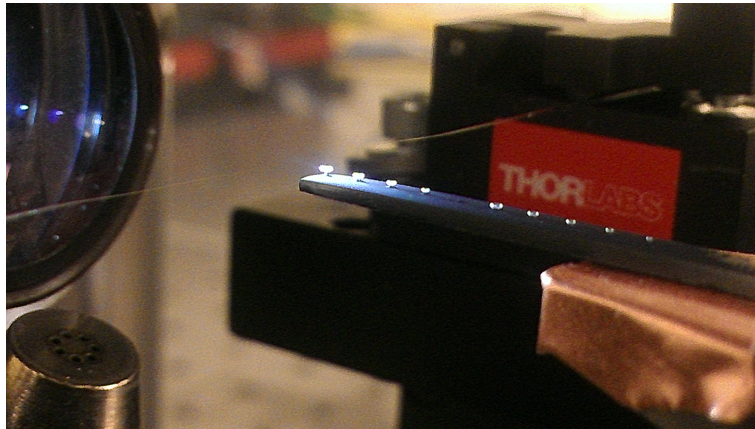


Figure 6.3: Picture of a pulled taper fiber, in the vicinity of GOBLiT devices.

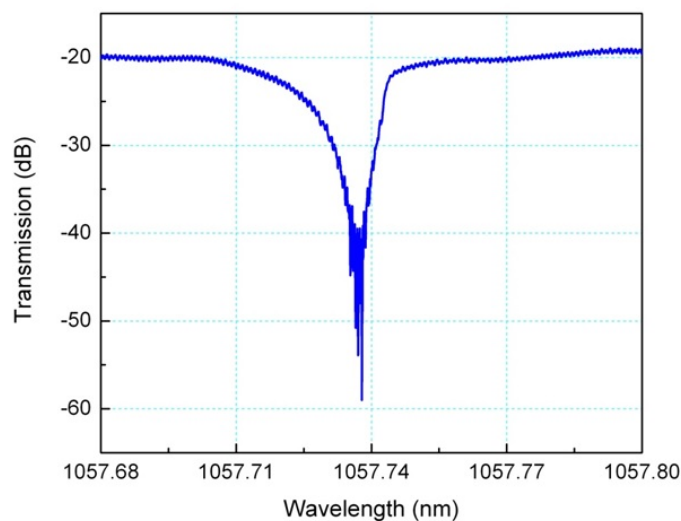


Figure 6.4: Transmission measurement of a $R = 42.5\mu\text{m}$ device measured with a 1065nm wavelength laser by collaborators at Army Research Labs. Quality factors were in the range of 850,000.

motor stages. A CW laser light is sent through the fiber and monitored via oscilloscope. Heating via a hydrogen torch and pulling via the motor stages are applied simultaneously. As the fiber stretches, it enters a multimode regime, seen on the oscilloscope as modulation of the transmission signal with increasing frequency as the taper is pulled. Once the taper again reaches single mode transmission, the pulling and heating are stopped. The motors are finally jogged in small steps to make the fiber taut.

The initial nitride devices fabricated showed fairly high optical Q's, though not extremely high due to roughness at the GOBLiT lip edge due to the RIE etch that defined the lip. Additionally, as device radius increased, optical quality factors dropped substantially due to prolonged exposure to HF during the release etch, as mentioned in the fabrication section.

Some of the smaller ($R = 42.5\mu\text{m}$) nitride devices were tested by collaborators

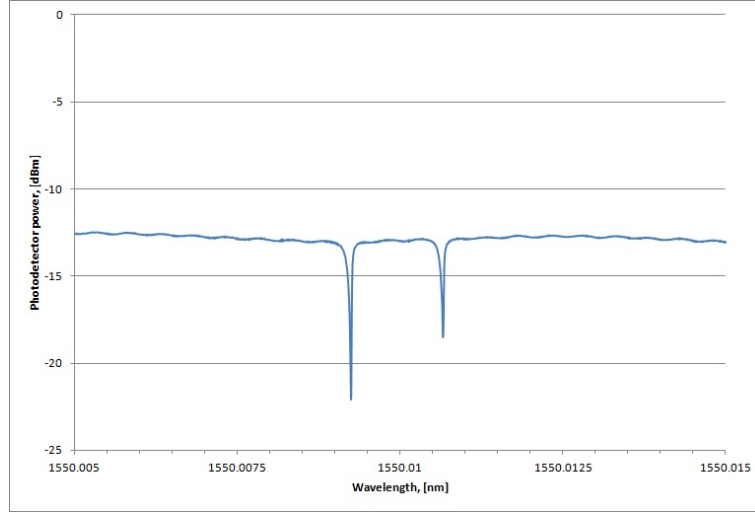


Figure 6.5: Optical Q measurement of $53.6E6$ for an oxide GOBLiT of radius $1000\mu\text{m}$.

at the Army Research Laboratory (ARL) while the setup at Cornell was not yet complete. These resulted in quality factors in the range of 850,000, as shown in Fig. 6.4. Cofabricated devices were later tested on the Cornell setup which showed much lower optical quality factors. This disparity was due to differences in the point at which the device was interrogated, as well as differences in coupling due to different taper geometries. (The ARL lab used a dimpled taper configuration, as in [26], which tend to ease integration with vacuum systems.)

A similar spatial dependence of coupling was found in the tested larger oxide GOBLiTs. When measured at the lip, these devices showed no discernible optical resonances. However, with careful coupling from under the lip, very high Q optical resonances were seen, such as that in Fig. 6.5. This is likely due to optical squeezing of the mode, causing it to move away from the edge of the lip, and is one of the reasons to move to a toroidal lip GOBLiT structure. The optical Q of a typical optical resonance mode of the fabricated TorLiT is shown in Fig. 6.6. It was such a mode that was then used to pick off the mechanical resonances of the device as

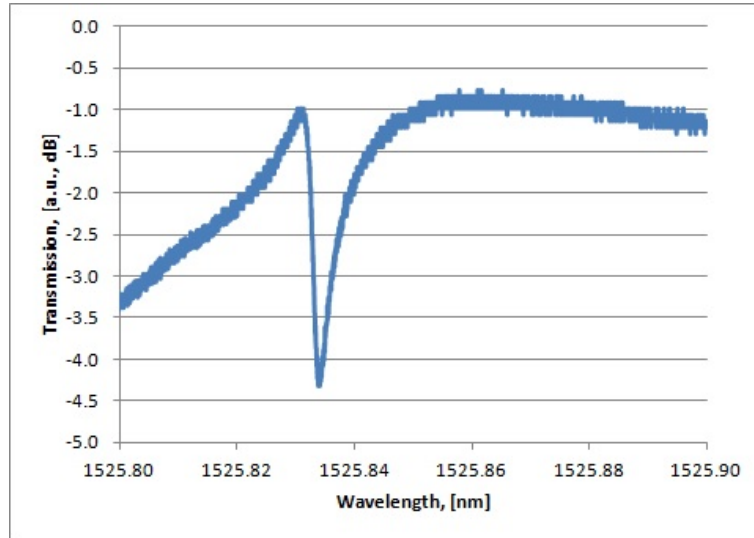


Figure 6.6: Optical Q measurement of a Toroidal Lipped GOBLiT of radius $60\mu\text{m}$ with $20\mu\text{m}$ lip and $2.5\mu\text{m}$ toroid minor radius.

shown in the section on Opto-Mechanical Pick-off.

One note must be made about the optical quality factors quoted in this section. All measurements here simply made use of the timestamp of the oscilloscope and an assumed relationship between the voltage and piezo modulation of the laser wavelength. Thus the values quoted are somewhat rough, and very large quality factors in particular may vary from the quoted values quite a bit. They are merely quantized in this instance as an idea of the optical quality factors achieved. To verify these measurements, a Mach-Zender Interferometer should be used.

6.2 Pump-probe

The small nitride GOBLiTs tested at ARL were also tested using a pump-probe setup. In such a scheme, two different wavelength laser sources are used to achieve both driving and sensing of the mechanical modes of the device. By amplitude

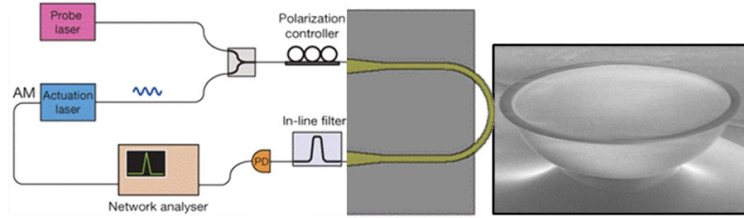


Figure 6.7: Diagram of setup for pump-probe measurements performed at ARL. The DUT was under 0.1 mTorr vacuum, and a dimpled optical taper was used for interrogation.

modulating one light source, gradient optical forces can be duly modulated to excite mechanical motion at the frequency of the amplitude modulation. By filtering out the amplitude modulated wavelength, the power at the photodetector will be due only to the sense wavelength. The modulation of the transmitted power of the sense wavelength, biased on the blue-detuned slope of an optical resonance, will then show the mechanical resonances. Fig. 6.7 shows the setup used to performed pump-probe measurements at ARL. The devices tested were kept at 0.1 mTorr pressure during testing.

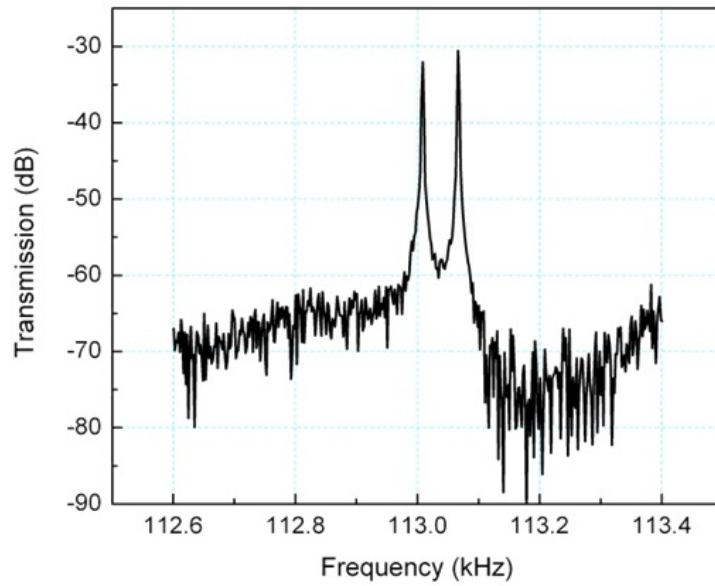


Figure 6.8: Pump-probe measurement of $m = 2$ wineglass mode of $42.5\mu\text{m}$ radius nitride GOBLiT, with mold formed on $\langle 111 \rangle$ Si.

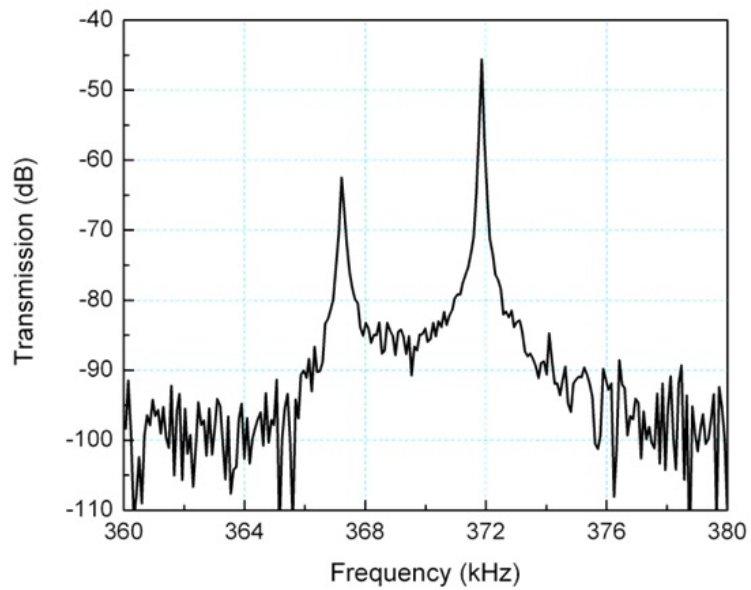


Figure 6.9: Pump-probe measurement of $m = 3$ wineglass mode of $42.5\mu\text{m}$ radius nitride GOBLiT, with mold formed on $\langle 111 \rangle$ Si.

Figs. 6.8 and 6.9 show the measured mechanical modes from the nitride GOB-LiT. One point of interest is the difference in frequency splitting between $m = 2$ and $m = 3$ wineglass modes. The measured resonator was formed from molds created using $\langle 111 \rangle$ silicon wafers, which would be expected to have hexagonal shaped anisotropy in the surface plane of the wafer. The fact that this leads to large splits in odd-order wineglass modes and small splits in even-order modes supports the assertions made in [24]. In cases where the angular separation of degenerate modes, $90^\circ/m$, matches the angular separation of perturbations, frequency splits are large; in cases where they do not match, frequency splits are small. The mechanical quality factor and frequency data for each of these measurements is summarized in Table 6.1.

Table 6.1: Summary of Pump-Probe Data

		m = 2		m = 3	
		Peak 1	Peak 2	Peak 1	Peak 2
Frequency, f	[kHz]	113.008	113.066	367	372
Frequency split, Δf	[Hz]	58		5k	
Quality factor, Q		565,320	566,804	230,450	3,620,000

6.3 LDV

One standard method of measuring mechanical resonances is the use of Laser Doppler Vibrometry. This technique uses the doppler shift of reflected coherent light to measure the velocity of the surface it is reflected off. For devices for which the integration of sensing elements is difficult, it is a good way to determine both the spectral response and mode shapes of mechanical resonances. The mechanical resonances are excited via a PZT thickness mode resonator glued to the bottom of the device substrate, as shown in Fig. 6.10. By focusing on one point and scanning the frequency of the PZT excitation, the mechanical resonance spectrum can be found. The mode shape of each of these resonances can then be determined by setting the PZT excitation at the resonance frequency and scanning the point of interrogation over the device surface.

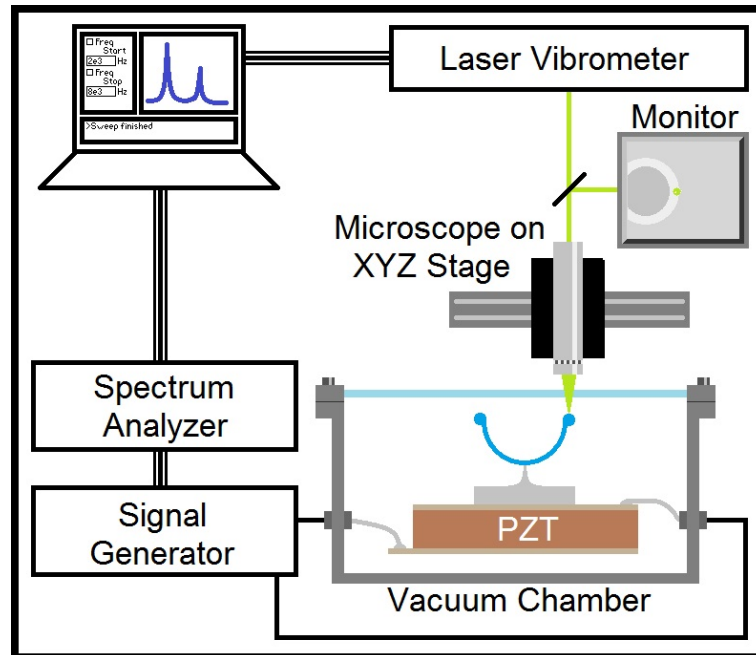


Figure 6.10: Diagram of LDV setup.

6.3.1 Air vs. Vacuum

Fig. 6.11 shows measurements of the same device taken in vacuum and air. The spectra shown are rather different, which has more to do with the actual point interrogated on the device than the pressure. Since the amplitude of the signal is proportional to the velocity of the surface the light is reflecting off, spectra can look very different depending on the point of interrogation.

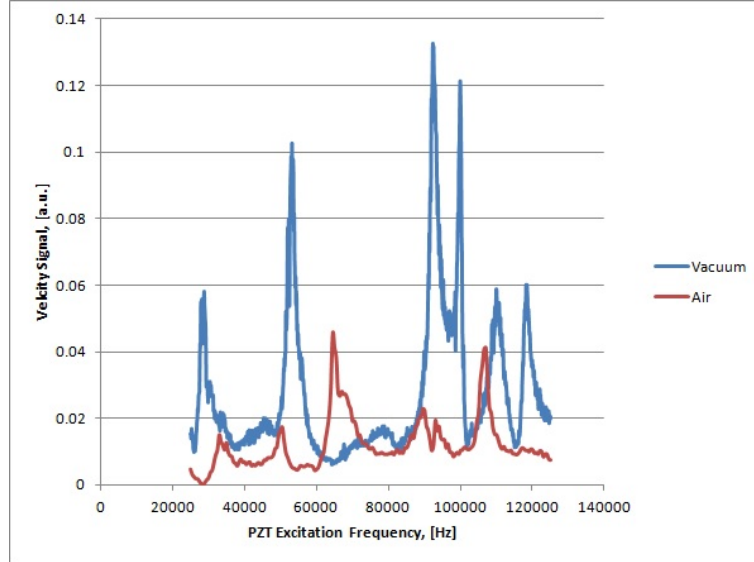


Figure 6.11: LDV measurements of oxide GOBLiT with $R = 120\mu\text{m}$ formed from SF_6 etched molds in vacuum and air.

Fig. 6.12 shows measurements in air and vacuum taken from the same point. The similarity in mechanical quality factor between the two shows that we are not limited by gaseous damping at this point. Such high mechanical energy losses are likely due to either anchor losses or roughness of the mold etch, which in this case was SF_6 . Since the device was already glued to the PZT sample, which had soldered on lead wires, and could not be put back in the XeF_2 etcher, further etching of the stem was not possible. However, devices with larger stem sizes as compared to device radius showed similar mechanical quality factors, leading to the belief that it was etch mold roughness that limited the mechanical Q. Fig. 6.13 shows an SEM of an SF_6 etch mold based device. The roughness on the bowl is very large, and could well be the reason for such low mechanical quality factors.

An LDV spectrum scan was also performed for the TorLiT device, shown in Fig. 6.14. There are clearly many closely spaced modes, and SEM measurements of dimensions are not precise enough to use simulation to determine which modes

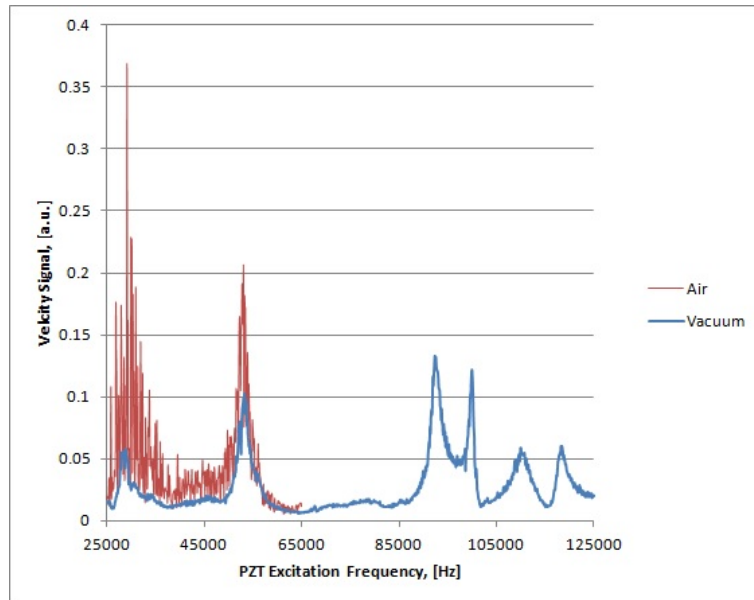


Figure 6.12: LDV measurements of oxide GOBLiT at same interrogation point in vacuum and air.

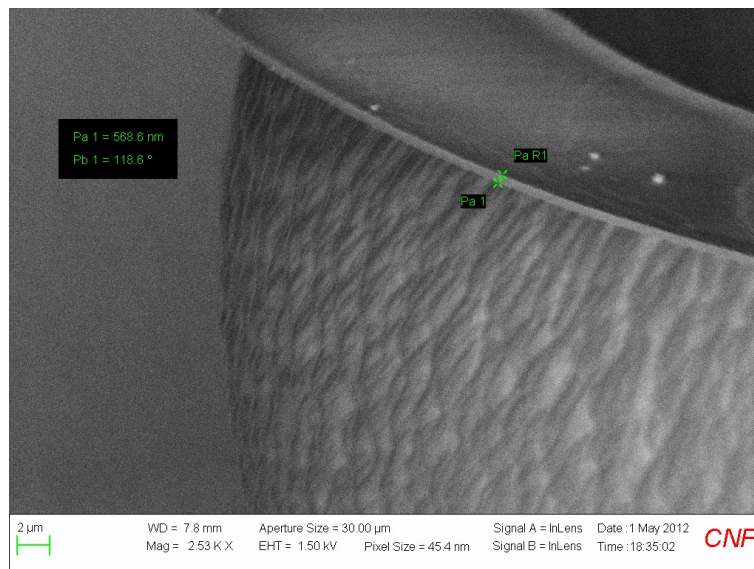


Figure 6.13: SEM showing the roughness of devices made using SF_6 etched molds. This could likely cause the low mechanical quality factors seen in measured devices.

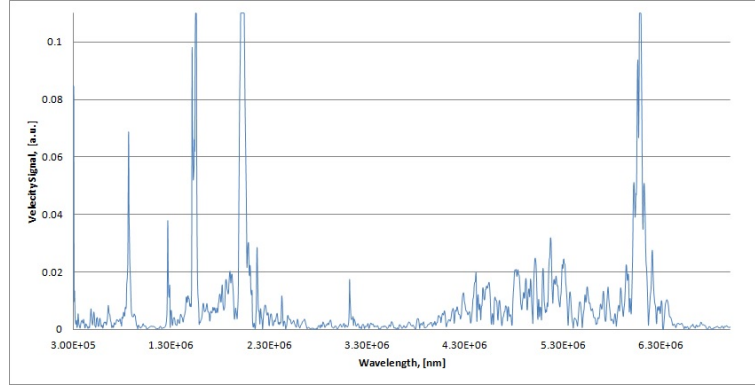


Figure 6.14: LDV spectrum for the TorLiT device, measured in vacuum. Clipping occurred due to higher sensitivity setting on LDV equipment.

correspond to which resonances. Thus a way to determine the mode shape for a given resonance is necessary.

6.3.2 2D Maps

Fig. 6.11 showed how the spectral response can vary based on the interrogation point; this can be used to identify mechanical resonance modes. By setting the PZT excitation frequency based on peaks found in the spectral response, and then scanning the interrogation point over the structure, a map of the mechanical mode can be made. Such 2D maps were used to identify the modes of the TorLiT structure. Figs. 6.15 and 6.16 show the $m = 2$ and $m = 3$ wineglass modes, found at 2.445 and 6.240 MHz respectively. Other modes, such as the $n = 3$ and $n = 4$ lip flapping modes shown in Figs. 6.17 and 6.18 were also found.

6.4 Opto-Mechanical Pick-off

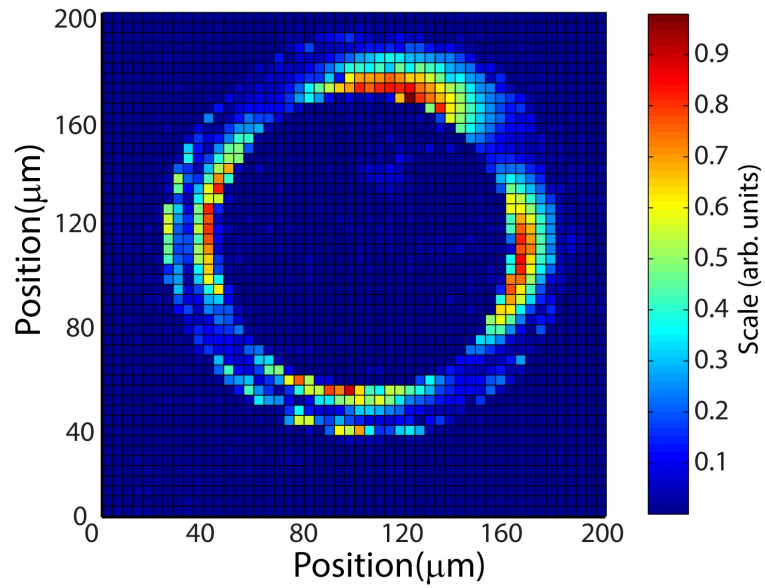


Figure 6.15: 2D LDV scan of $m = 2$ wineglass mode at 2.445MHz for Toroidal Lipped GOBLiT structure, used to identify mechanical modes within a crowded spectral response.

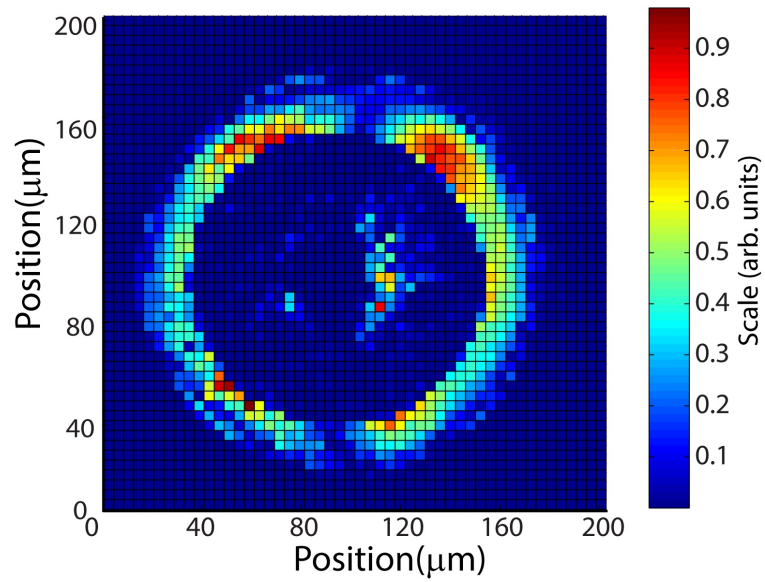


Figure 6.16: 2D LDV scan of $m = 3$ wineglass mode at 6.240MHz for Toroidal Lipped GOBLiT structure, used to identify mechanical modes within a crowded spectral response.

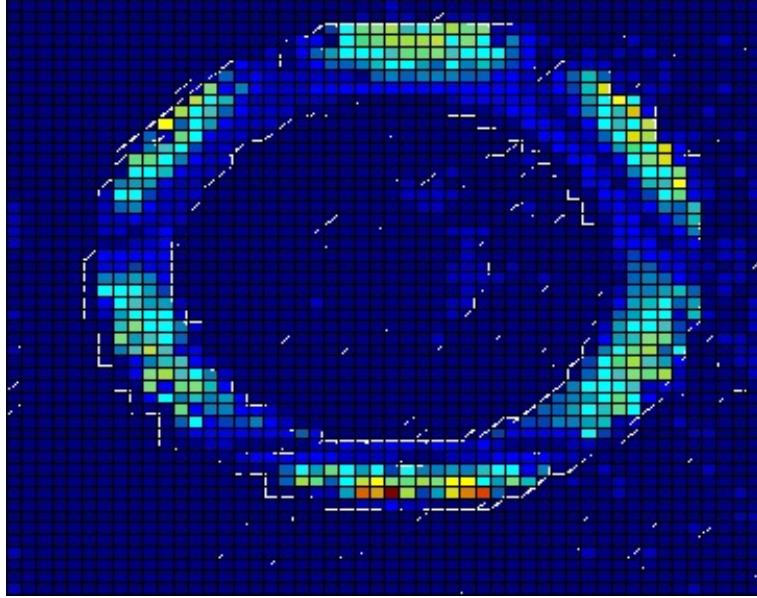


Figure 6.17: 2D LDV scan of $m = 3$ lip flapping mode at 2.14MHz for Toroidal Lipped GOBLiT structure.

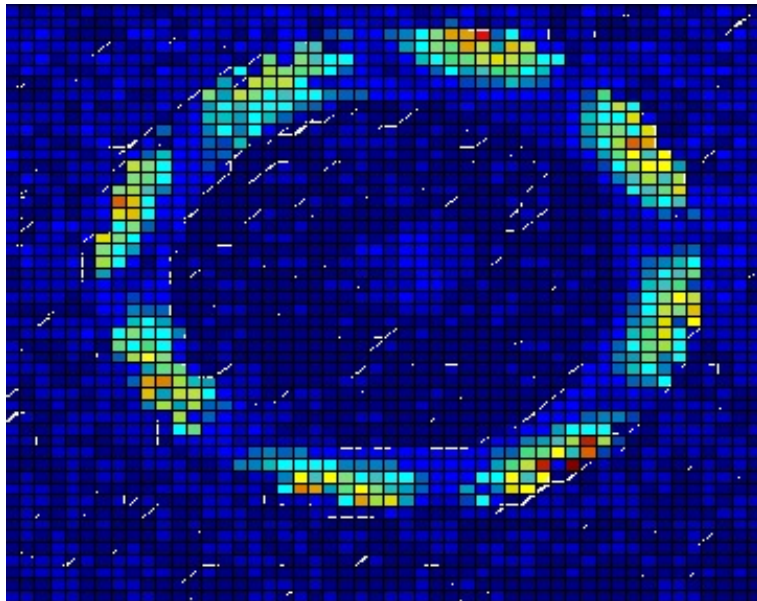


Figure 6.18: 2D LDV scan of $m = 4$ lip flapping mode at 3.145MHz for Toroidal Lipped GOBLiT structure.

Pick off of mechanical modes is also possible using an optical fiber taper, as shown in the pump-probe measurements performed at ARL. However, integration of optical fiber tapers with vacuum can be quite difficult, and requires decently large vacuum chambers to accommodate all the piezo stages needed to align the device with the taper. Since we did not have such a setup, we could not achieve sufficient opto-mechanical force to overcome damping for pump-probe techniques at atmospheric pressure.

Instead, we made use of the PZT already glued to the TorLiT sample for LDV measurements to excite motion, which was read off optically, as shown in the setup schematic in Fig. 6.19. The results of this measurement are shown in Fig. 6.20. It is particularly interesting to compare the LDV spectrum of the TorLiT structure with the opto-mechanical measurement made of the same device, as in Fig. 6.21. The two match quite well, showing that at the power levels used there is very little optical spring stiffening. The large opto-mechanical peak around 1 MHz which is not present in the LDV spectrum is the fundamental radial mode; this mode will have the strongest modulation of the optical transmission, but will not show up at all in the LDV measurement since it does not induce any significant velocity in the direction measured (normal to the XY plane). We saw that there was very

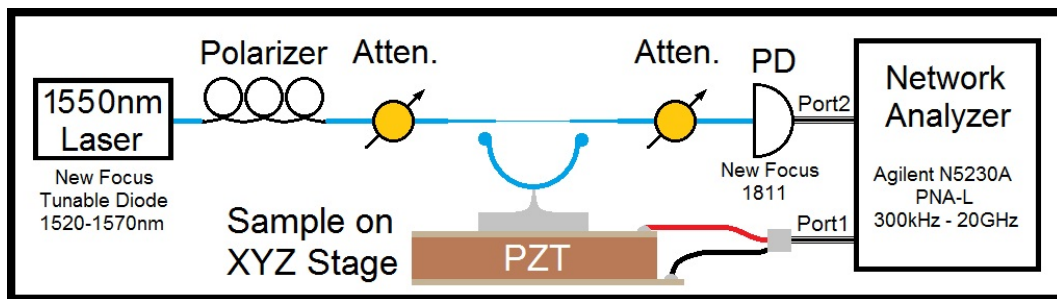


Figure 6.19: Schematic of setup for opto-mechanical measurements of the TorLiT structure. The PZT used for LDV measurements was used to excite motion.

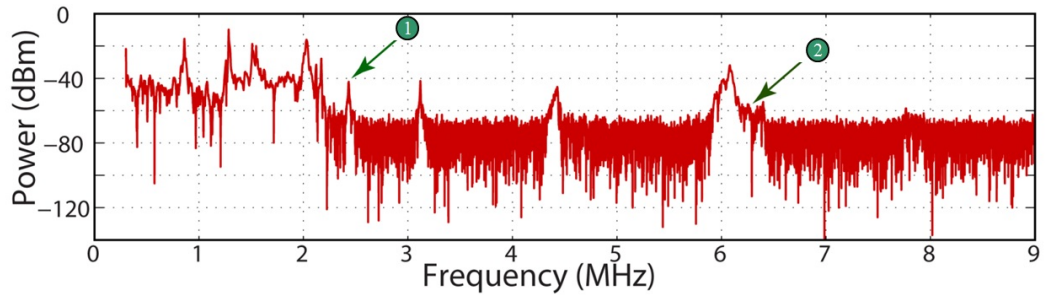


Figure 6.20: Opto-mechanical measurement for TorLiT structure. 1 denotes the $m = 2$ wineglass mode, and 2 denotes the $m = 3$ wineglass mode, as identified using 2D LDV scans.

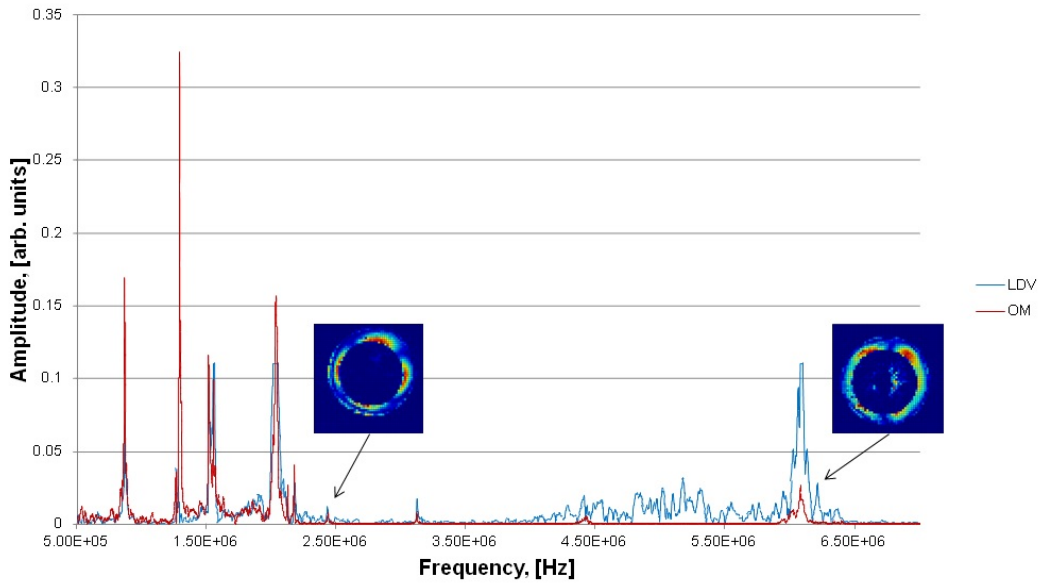


Figure 6.21: Comparison of mechanical measurements for the TorLiT structure. Blue is the LDV measurement, with light reflecting perpendicularly off the top surface of the lip, red is the opto-mechanical measurement, made at the edge of the toroidal lip.

little displacement of the rim in $m = 3$ wineglass mode from the 2D LDV plot, and we do not see a resonance at that frequency in the opto-mechanical measurement. However, this could also be due to interrogating at a nodal point in the $m = 3$ wineglass mode, assuming the frequency split between degenerate modes is large enough to push the other $m = 3$ wineglass mode into another peak (which is quite possible due to the use of $\langle 111 \rangle$ wafers for these devices). Simulation showed much cleaner spectra for TorLiT structures when the lip is further melted; such devices were created, measured and show the expected results. However, those results are part of an unpublished joint effort with Ajay Bhat, and will not be shown here. Please look for a future jointly authored work for details.

6.5 Conclusion

In this chapter, measurements were presented of some of the basic parameters of interest for using the GOBLiT and TorLiT structures for an opto-mechanical gyroscope. Transmission measurements showed optical quality factors as high as $53.6E6$ with careful coupling, albeit with several caveats as mentioned regarding the method of calculation for Q . The measured pump-probe results show the viability of an all optical transduction scheme, and also support the claims made as to the relationship between azimuthal order of perturbation and resonance mode. LDV results showed the limitation of mechanical quality factor due to roughness in the case of SF_6 etched mold devices, and in the case of the TorLiT structure, acted as both a spectral and mode-mapping tool. Opto-mechanical pick off of resonance modes was also shown for the TorLiT with piezo-actuation, and correlated well to results from LDV. The spectra of the TorLiT was crowded with parasitic modes, but devices with much cleaner spectra have been fabricated and will be presented

in a later co-authored paper. Verification of the optical and mechanical parameters required for the structure of an opto-mechanical gyroscope is performed.

CHAPTER 7

FUTURE WORK

7.1 Fabrication Work

One of the most obvious fabrication steps forward from this work is to reduce the thickness, and thus the frequency of the TorLiT structure. In fact, this has already been accomplished, and will be part of a future jointly authored work between the author and Ajay Bhat. The initial device thickness was chosen due to known laser melting power at $1.5\mu\text{m}$; for showing proof of concept it was easiest to maintain some known variables. The DEOS fabrication process also still shows promise, and with some work on the optimization of implantation doses and annealing and oxidation temperatures, could lead to some very promising structures with more evenly distributed mass. In terms of the feasibility of an OMG, the top priority of future work would be to integrate waveguides into the process flow. This is difficult enough for any 3D process, but the changing radius of the TorLiT makes it especially difficult. It may require fabricating waveguides on moveable platforms which can then be locked into place, or other such complexities. Eventual industrial application would also require a much more thorough study of the HNA etch uniformity over the whole wafer; tanks and stirring equipment to hold temperature and agitation variables constant would be necessary, as well as fine control of chemical mixtures.

7.2 Device Work

From a device standpoint, building up an optical taper setup in vacuum would be the next logical step. Such a system would take some time to build from available components, but is vital to pump-probe measurements. Once such a system is built, gyroscopic measurements would then require integration of the vacuum chamber with a rate table, which would need to be quite large to accommodate the entire optical portion of the setup. To truly measure the gyroscopic performance would also require more than one interaction point, and thus either optical tapers that could be independently positioned with respect to the DUT, or integrated waveguides as mentioned previously. Collaboration with Prof. Mukund Vengalattore to combine the GOBLiT or TorLiT structures with Bose-Einstein Condensate based atom interferometer gyroscopes has already begun, and hopes to combine the fast startup time of the OMG with the sensitivity and accuracy of the BEC gyro via shared optical modes. Please look forward to future publications on the topic from the OxideMEMS and Vengalattore groups.

APPENDIX A
CORIOLIS FORCE DERIVATION

This is an appendix covering the derivation of the Coriolis Force, for which I have borrowed heavily from [27]. Coriolis force is one of the so-called fictitious forces, together with centrifugal force, and is derived from translational physics by looking at them in a rotating frame of reference. From this point on we will use the convention of notating a term that is defined from a rotating frame of reference using *. Then, for any force as seen from an inertial frame of reference:

$$\mathbf{F} = m\mathbf{a} = m\mathbf{a}^* + m\mathbf{a}_{fic} \quad (\text{A.1})$$

To derive the Coriolis force, we first look at how to define one point from both a rotating and an inertial frame of reference. For some point P as shown in Fig. A.1, we define a vector from the origin of the inertial frame of reference as \mathbf{r} and a vector from the origin of the rotating frame of reference as \mathbf{r}^* . These two vectors are then related by:

$$\mathbf{r} = \mathbf{r}^* + \mathbf{h} \quad (\text{A.2})$$

If O^* rotates with time, \mathbf{r}^* will change (\mathbf{h} will not since the origin stays in the same point). Taking the derivative of each side of Eq. A.2 with respect to time,

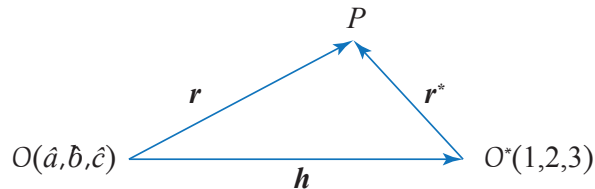


Figure A.1: We start by defining a point in both inertial and rotating frames of reference.

we find:

$$\frac{d\mathbf{r}}{dt} = \frac{d\mathbf{r}^*}{dt} + \frac{d\mathbf{h}}{dt} = \frac{d(r_1^*\hat{\mathbf{i}} + r_2^*\hat{\mathbf{j}} + r_3^*\hat{\mathbf{k}})}{dt} + \frac{d\mathbf{h}}{dt} \quad (\text{A.3})$$

We simplify this equation for further manipulation by rewriting the terms of the axes of O^* with the generalized notation $\hat{\mathbf{i}}$.

$$\frac{d\mathbf{r}}{dt} = \frac{dr_i^*}{dt}\hat{\mathbf{i}} + r_i^*\frac{d\hat{\mathbf{i}}}{dt} + \frac{d\mathbf{h}}{dt} \quad (\text{A.4})$$

Taking the derivative again, we arrive at:

$$\frac{d^2\mathbf{r}}{dt^2} = \frac{d}{dt} \left[\frac{dr_i^*}{dt}\hat{\mathbf{i}} + r_i^*\frac{d\hat{\mathbf{i}}}{dt} \right] + \frac{d^2\mathbf{h}}{dt^2} \quad (\text{A.5})$$

Expanding all terms:

$$\frac{d^2\mathbf{r}}{dt^2} = \frac{d^2r_i^*}{dt^2}\hat{\mathbf{i}} + 2\frac{dr_i^*}{dt}\frac{d\hat{\mathbf{i}}}{dt} + r_i^*\frac{d^2\hat{\mathbf{i}}}{dt^2} + \frac{d^2\mathbf{h}}{dt^2} \quad (\text{A.6})$$

Here we have an equation describing the acceleration of a point as seen from both inertial and rotating coordinate frames in terms of vectors from their origins. The left-hand side of the equation describes the acceleration as seen from the inertial frame of reference. The right-hand side terms can be explained as follows:

- First** The acceleration of the point as seen from the rotating coordinate frame.
- Second** The velocity of the point as seen from the rotating coordinate frame times the velocity of the rotating coordinate frame as seen from the inertial frame.
- Third** The position of the point as seen from the rotating frame times the acceleration of the frame as seen from the inertial frame.
- Fourth** Any translational acceleration of the origin of the rotating frame itself.

Eq. A.6 describes the general case of relating the acceleration of a point in an inertial versus a non-inertial frame of reference; we will now look at the particular case where the non-inertial frame is rotating with some angular velocity ω .

For some vector \mathbf{B} at rest in O^* and rotating with angular velocity $\boldsymbol{\omega}$ in O , the velocity of the vector as seen from the inertial frame is given by:

$$\frac{d\mathbf{B}}{dt} = \boldsymbol{\omega} \times \mathbf{B} \quad (\text{A.7})$$

This makes intuitive sense: for a vector that is rotating such that its base does not move and its tip describes a circle at some rate ω , we would describe the tangential speed of the tip as the distance from the center times the angular velocity, pointing in the direction defined by their cross product.

If we now take \mathbf{B} to be the axes of O^* , we can define how O relates to O^* :

$$\frac{d\hat{\mathbf{i}}}{dt} = \boldsymbol{\omega} \times \hat{\mathbf{i}} \quad (\text{A.8})$$

Additionally, let us define $\boldsymbol{\omega} = \omega \hat{\mathbf{n}}$. Then Eq. A.6 becomes:

$$\frac{d^2\mathbf{r}}{dt^2} = \frac{d^2r_i^*}{dt^2} \hat{\mathbf{i}} + 2 \frac{dr_i^*}{dt} \boldsymbol{\omega} \times \hat{\mathbf{i}} + r_i^* \boldsymbol{\omega} \times (\boldsymbol{\omega} \times \hat{\mathbf{i}}) + r_i^* \frac{d\omega}{dt} \hat{\mathbf{n}} \times \hat{\mathbf{i}} + \frac{d^2\mathbf{h}}{dt^2} \quad (\text{A.9})$$

Assuming that the origin of O^* is not moving and that there is no angular acceleration, we can drop the last two terms. Rewriting in terms of accelerations and velocities, and multiplying through by the mass, we arrive at our force equation:

$$\mathbf{F} = ma_i^* \hat{\mathbf{i}} + 2m\boldsymbol{\omega} \times v_i \hat{\mathbf{i}} + m\boldsymbol{\omega} \times (\boldsymbol{\omega} \times r_i^* \hat{\mathbf{i}}) \quad (\text{A.10})$$

In this case, \mathbf{F} is the force as seen from the inertial frame, O . However, in the case of gyroscopes, the observer is rotating with the mass; therefore it is more illuminating to look at the force as seen from the rotating coordinate system.

$$ma_i^* \hat{\mathbf{i}} = \mathbf{F} - 2m\boldsymbol{\omega} \times v_i \hat{\mathbf{i}} - m\boldsymbol{\omega} \times (\boldsymbol{\omega} \times r_i^* \hat{\mathbf{i}}) \quad (\text{A.11})$$

Now we finally see the Coriolis (2^{nd}) and centrifugal (3^{rd}) force terms that we expect.

APPENDIX B
OPTICAL SPRING EFFECT

This is an appendix covering the derivation of the optical spring effect. This derivation is based heavily on the supplementary section provided by J. Rosenberg in [13].

We begin this derivation by defining the rate of change of intracavity field for a given optical cavity:

$$\frac{da_p}{dt} = (-i\Delta_p - \frac{\Gamma_{tp}}{2})a_p - ig_{OM}xa_p + i\gamma|a_p|^2a_p + i\sqrt{\Gamma_{ep}}A_p \quad (\text{B.1})$$

It will be clearer for reference to explain each of these terms in a list:

- a_p The light field inside the cavity.
- Δ_p The detuning between the frequency of the input light and the resonance frequency of the optical cavity, defined as $\Delta_p = \omega_{p0} - \omega_p$ where ω_{p0} is the frequency of the optical resonance of interest and ω_p is the frequency of the input light.
- Γ_{tp} The photon decay rate of the loaded cavity for optical resonance of interest.
- g_{OM} The optomechanical coupling factor, defined as $d\omega_{p0}/dx$. This effectively states how sensitive the optical resonance frequency is to mechanical displacements, and will vary for different mechanical modes of resonance.
- x The mechanical displacement of the cavity structure, a function of time.
- γ A term describing the self-phase modulation introduced by the Kerr non-linearity of silicon dioxide. Please see [13] for more information.
- $\sqrt{\Gamma_{ep}}$ The photon escape rate of the external field (i.e. the escape rate from the taper or waveguide).

A_p The input field of the light wave, which is traveling in the taper or waveguide.

For our derivation we will assume the opto-mechanical effect to be dominant, such that the self-modulation due to the Kerr nonlinear effect can be ignored.

We now assume that the input light wave consists of a large constant field with a small modulated signal on top, $A_p = A_{p0} + \delta A_p(t)$. The intracavity field will then likewise be given by $a_p = a_{p0} + \delta a_p(t)$, and the equation for the intracavity field can be broken up into:

$$\frac{da_{p0}}{dt} = (-i\Delta_p - \frac{\Gamma_{tp}}{2})a_{p0} + i\sqrt{\Gamma_{ep}}A_{p0} \quad (\text{B.2a})$$

$$\frac{d\delta a_p}{dt} = (-i\Delta_p - \frac{\Gamma_{tp}}{2})\delta a_p - ig_{OM}x a_{p0} + i\sqrt{\Gamma_{ep}}\delta A_{p0} \quad (\text{B.2b})$$

Setting the left-hand side of Eq. B.2a equal to zero, we find a steady-state solution for the non-time varying portion of the intracavity field:

$$a_{p0} = \frac{i\sqrt{\Gamma_{ep}}A_{p0}}{\frac{\Gamma_{tp}}{2} + i\Delta_p} \quad (\text{B.3})$$

Since a photodetector actually measures power, not the field intensity, let us determine what the average power dropped into the cavity, P_{pd} , will be. We define:

$$P_{pd} = \Gamma_{op}|a_{p0}|^2 \quad (\text{B.4})$$

where $|a_{p0}|^2$ is the average intracavity energy and Γ_{op} is the intrinsic photon decay rate of the optical mode (i.e. non-loaded). However, since we have no easy way of measuring that power directly, we expand this equation to find the average dropped power in terms of the average input power, $P_{p0} = |A_{p0}|^2$. Multiplying a_{p0} and a_{p0}^* we obtain:

$$P_{pd} = \frac{\Gamma_{op}P_{p0}\Gamma_{ep}}{\Delta_p^2 + \left(\frac{\Gamma_{tp}}{2}\right)^2} \quad (\text{B.5})$$

Looking at this equation, we can say, to the zeroth order, that the ratio of modulated power to DC power dropped into the cavity is equal to the ratio of the input modulated power to input DC power:

$$\frac{\delta P_{pd}(t)}{P_{pd}} = \frac{\delta P_p(t)}{P_{p0}} \quad (\text{B.6})$$

where $\delta P_p = A_{p0}^* \delta A_p + A_p \delta A_{p0}^*$ is the input modulated power.

Going back to Eq. B.2b, we can take the Fourier transform to find the modulated intracavity field in the frequency domain. Using

$$\mathcal{F} \left[\frac{d\delta a_p}{dt} \right] = (i\Omega) \delta \tilde{a}_p \quad (\text{B.7})$$

we derive

$$(i\Omega) \delta \tilde{a}_p = \left(-i\Delta_p - \frac{\Gamma_{tp}}{2} \right) \delta \tilde{a}_p - ig_{OM} a_{p0} \tilde{x} + i\sqrt{\Gamma_{ep}} \delta \tilde{A}_p \quad (\text{B.8})$$

Rearranging terms we gain the equation

$$\delta \tilde{a}_p = \frac{ig_{OM} a_{p0} \tilde{x} - i\sqrt{\Gamma_{ep}} \delta \tilde{A}_p}{-i \left(\Delta_p + \Omega \right) - \frac{\Gamma_{tp}}{2}} \quad (\text{B.9})$$

In [13], there are some sign differences due to a different definition of the Fourier transform being used. This is to make the physical phenomena of blue detuning the laser with respect to the optical resonance lead to heating of the cavity, when Δ_p is defined as $\omega_p - \omega_{p0}$. However, in our case, flipping the sign in the definition of Δ_p has allowed us to use the standard definition of the Fourier transform.

We now have an equation that describes the spectral response of the cavity based on the spectrum of the input power and mechanical displacement of the structure. To determine the displacement of the structure, we will first have to take a look at the forces acting on the structure. For our device we will assume that the dominant force acting on the structure is the optical gradient force. The

optical gradient force, F_{og} , can be derived from the change in intracavity energy as the coupling to the cavity changes, as in [28]. If we define the intracavity energy to be $U_p = |a_{p0}|^2 = N\hbar\omega_p$, where N is the number of photons in the cavity, \hbar is the energy of each photon, and ω_p is their energy, we find:

$$F_{og} = -\left.\frac{dU_p}{dx}\right|_k = -\left.\frac{d(N\hbar\omega_p)}{dx}\right|_k = -N\hbar\left.\frac{d\omega_p}{dx}\right|_k = -\frac{1}{\omega_p}\left.\frac{d\omega_p}{dx}\right|_k U_p = -\frac{g_{OM}U_p}{\omega_p} \quad (\text{B.10})$$

Of course, we already know that there will be a portion of the intracavity field that is modulated, and similarly, we can break the optical gradient force into DC and modulated components: $F_{og} = F_{og0} + \delta F_{og}(t)$, where we define:

$$F_{og0} = -\frac{g_{OM}U_{p0}}{\omega_p}, U_{p0} = |a_{p0}|^2 \quad (\text{B.11a})$$

$$\delta F_{og}(t) = -\frac{g_{OM}\delta U_p}{\omega_p} = -\frac{g_{OM}}{\omega_p} [a_{p0}^*\delta a_p(t) + a_{p0}\delta a_p^*(t)] \quad (\text{B.11b})$$

We define $\delta U_p(t)$ this way by assigning to it the time varying terms of the expansion of $(a_{p0} + \delta a_p)(a_{p0}^* + \delta a_p^*)$. The small constant term $\delta a_p\delta a_p^*$ is ignored as negligible in the definition of U_{p0} .

We can now put Eq. B.9 into Eq. B.11b to find the modulated optical gradient force in terms of the structure's displacement, \tilde{x} . After much manipulation, this results in:

$$\begin{aligned} \delta \tilde{F}_{og} = & \frac{2g_{OM}^2|a_{p0}|^2\Delta_p}{\omega_p} \left[\frac{\left(\frac{\Gamma_{tp}}{2}\right)^2 + \Delta_p^2 - \Omega^2 - i\Gamma_{tp}\Omega}{\left[\left(\frac{\Gamma_{tp}}{2}\right)^2 + (\Delta_p - \Omega)^2\right] \left[\left(\frac{\Gamma_{tp}}{2}\right)^2 + (\Delta_p + \Omega)^2\right]} \right] \tilde{x} \\ & + i\frac{g_{OM}}{\omega_p} \sqrt{\Gamma_{ep}} \left[\frac{a_{p0}^*\delta \tilde{A}_p(\Omega)}{-i(\Delta_p + \Omega) - \frac{\Gamma_{tp}}{2}} + \frac{a_{p0}\delta \tilde{A}_p^*(-\Omega)}{-i(\Delta_p - \Omega) + \frac{\Gamma_{tp}}{2}} \right] \end{aligned} \quad (\text{B.12})$$

The first term of Eq. B.12 is the mechanical induced back-action, the second term gives the direct input modulation of the force.

We can describe the mechanical motion of the structure as:

$$\frac{d^2x}{dt^2} + \Gamma_m \frac{dx}{dt} + \Omega_m^2 x = \frac{1}{m_{eff}} (F_{og} + F_T) = \frac{1}{m_{eff}} (F_{og0} + \delta F_{og} + F_T) \quad (\text{B.13})$$

where Γ_m is the mechanical damping, Ω_m is the mechanical resonance frequency, and m_{eff} is the effective mass for the mechanical resonance mode under consideration. F_T refers to the thermal Langevin force responsible for brownian motion, the correlation function of which is given by:

$$\langle F_T(t)F_T(t + \tau) \rangle = 2m_{eff}\Gamma_m k_B T \delta(\tau) \quad (\text{B.14})$$

Returning to Eq. B.13, we can neglect all non-DC terms to find the static displacement of the structure, which we can determine in terms of the power dropped into the cavity using Eqns. B.11a and B.4.

$$x_0 = \frac{|F_{og0}|}{m_{eff}\Omega_m^2} = \frac{g_{OM}U_{p0}}{k_m\omega_p} = \frac{g_{OM}P_{pd}}{k_m\omega_p\Gamma_{op}} \quad (\text{B.15})$$

where $k_m = m_{eff}\Omega_m^2$ is the mechanical spring constant. It is clear from this equation that we can tune the static displacement using the average power dropped into the cavity. This in turn can be used to tune the cavity optical resonance.

At this point, we will define some new terms to reduce the length of our equations. The first of these is $f_{og}(\Omega)\tilde{x}$, which we will define as the mechanically induced backaction term of Eq. B.12:

$$f_{og}(\Omega)\tilde{x} = \frac{2g_{OM}^2|a_{p0}|^2\Delta_p}{\omega_p} \left[\frac{\left(\frac{\Gamma_{tp}}{2}\right)^2 + \Delta_p^2 - \Omega^2 - i\Gamma_{tp}\Omega}{\left[\left(\frac{\Gamma_{tp}}{2}\right)^2 + (\Delta_p - \Omega)^2\right] \left[\left(\frac{\Gamma_{tp}}{2}\right)^2 + (\Delta_p + \Omega)^2\right]} \right] \tilde{x} \quad (\text{B.16})$$

Then we can look at Eq. B.13 in the frequency spectrum by taking the Fourier transform of each term to get:

$$-\Omega^2\tilde{x} - i\Gamma_m\Omega\tilde{x} + \Omega_m^2\tilde{x} = \frac{1}{m_{eff}} \left(\delta\tilde{F}_{og} + \tilde{F}_T \right) \quad (\text{B.17})$$

If we define $\delta\tilde{F}_{og} = f_{og}(\Omega)\tilde{x} + \tilde{f}_{input}$ where \tilde{f}_{input} is the direct input modulation (second term of Eq. B.12), we can rearrange terms to arrive at:

$$\tilde{x} \left(\Omega_m^2 - \Omega^2 - i\Gamma_m\Omega - \frac{1}{m_{eff}}f_{og}(\Omega) \right) = \frac{\tilde{f}_{input} + \tilde{F}_T}{m_{eff}} \quad (\text{B.18})$$

We will lump all the frequency terms on the left-hand side of Eq. B.18 into one term for ease of reference:

$$\mathcal{L}(\Omega) = \left(\Omega_m^2 - \Omega^2 - i\Gamma_m\Omega - \frac{1}{m_{eff}}f_{og}(\Omega) \right) \quad (\text{B.19})$$

So we now have:

$$\tilde{x} = \frac{\tilde{F}_T + \tilde{f}_{input}}{m_{eff}\mathcal{L}(\Omega)} \quad (\text{B.20})$$

Eq. B.19 shows us clearly how the mechanically induced back-action term of the optical gradient force creates an optical spring stiffening/softening effect: by incorporating the real and imaginary terms of $f_{og}(\Omega)$ with Ω_m and Γ_m respectively we find:

$$\mathcal{L}(\Omega) = (\Omega'_m)^2 - \Omega^2 - i\Gamma'_m\Omega \quad (\text{B.21})$$

What makes the optical spring effect truly interesting is that it leads not only to spring stiffening/softening, but also modifies the mechanical damping of the structure.

Let us now expand the \tilde{F}_T term. We already defined the autocorrelation function in Eq. B.14, but we want to find the PSD of the thermal mechanical displacement from that. We can use the relationship between the autocorrelation function and the PSD of a function to find this. For the autocorrelation of a function f given as $\mathbb{R}_x(\tau)$, it's PSD, $\mathbb{S}_x(\Omega)$ is defined as:

$$\mathcal{F} [\mathbb{R}_x(\tau)] = \mathbb{S}_x(\Omega) \quad (\text{B.22})$$

Then if we have $\mathbb{R}_x(\tau) = \langle F_T(t)F_T(t + \tau) \rangle$, the PSD of F_T is given by:

$$\mathbb{S}_x(\Omega) = \int_{-\infty}^{\infty} 2m_{eff}\Gamma_mk_BT\delta(\tau)e^{-2\pi i\Omega\tau}d\tau = 2m_{eff}\Gamma_mk_BT \quad (\text{B.23})$$

However, this is the PSD of the Langevin force, not the displacement. We find the displacement PSD by shaping Eq. B.23 with the transfer function $H(\Omega) = \frac{1}{m_{eff}\mathcal{L}(\Omega)}$ as:

$$\mathcal{S}_x(\Omega) = |H(\Omega)|^2 \mathbb{S}_x(\Omega) = \frac{2\Gamma_m k_B T}{m_{eff} |\mathcal{L}(\Omega)|^2} \quad (\text{B.24})$$

BIBLIOGRAPHY

- [1] G. Barenboim and J. A. Oteo, “One pendulum to run them all,” *European Journal of Physics*, vol. 34, no. 4, p. 1049, 2013. [Online]. Available: <http://stacks.iop.org/0143-0807/34/i=4/a=1049>
- [2] I. Prikhodko, S. Zotov, A. Trusov, and A. Shkel, “Foucault pendulum on a chip: angle measuring silicon mems gyroscope,” in *Micro Electro Mechanical Systems (MEMS), 2011 IEEE 24th International Conference on*, 2011, pp. 161–164.
- [3] J. A. Gregory, J. Cho, and K. Najafi, “Mems rate and rate-integrating gyroscope control with commercial software defined radio hardware,” in *Solid-State Sensors, Actuators and Microsystems Conference (TRANSDUCERS), 2011 16th International*, 2011, pp. 2394–2397.
- [4] A. A. Trusov, “Overview of mems gyroscopes: History, principles of operations, types of measurements,” University of California Irvine, MicroSystems Laboratory, Mechanical and Aerospace Engineering, Tech. Rep., May 2011. [Online]. Available: <http://http://www.alexandertrusov.com/uploads/pdf/2011-UCI-trusov-whitepaper-gyros.pdf>
- [5] S. Zotov, I. Prikhodko, A. Trusov, and A. Shkel, “Frequency modulation based angular rate sensor,” in *Micro Electro Mechanical Systems (MEMS), 2011 IEEE 24th International Conference on*, 2011, pp. 577–580.
- [6] M. Vagner, “Mems gyroscope performance comparison using allan variance method,” in *STUDENT EEICT 2011, Proceedings of the 17th Conference*, 2011, pp. 199–203.
- [7] D. Rozelle, “The hemispherical resonator gyro: From wineglass to the planets (aas 09-176),” in *19th AAS/AIAA Space Flight Mechanics Meeting, 2009, Savannah GA.*, Feb 2009, pp. 1157–1178.
- [8] S. V. Joubert, M. Y. Shatalov, and T. H. Fay, “Rotating structures and Bryan’s effect,” *American Journal of Physics*, vol. 77, no. 6, pp. 520–525, 2009. [Online]. Available: <http://link.aip.org/link/?AJP/77/520/1>
- [9] D. Senkal, I. Prikhodko, A. Trusov, and A. Shkel, “Micromachined 3-d glass-blown wineglass structures for vibratory mems applications,” in *Technologies for Future Micro-Nano Manufacturing*, August 2011, pp. 166–169.

- [10] Q. Unterreithmeier, E. Weig, and J. Kotthaus, “Universal transduction scheme for nanomechanical systems based on dielectric forces,” *Nature Letter*, no. 458, pp. 1001–1004, 2009. [Online]. Available: <http://dx.doi.org/10.1038/nature07932>
- [11] J. C. Knight, G. Cheung, F. Jacques, and T. A. Birks, “Phase-matched excitation of whispering-gallery-mode resonances by a fiber taper,” *Opt. Lett.*, vol. 22, no. 15, pp. 1129–1131, Aug 1997. [Online]. Available: <http://ol.osa.org/abstract.cfm?URI=ol-22-15-1129>
- [12] E. J. Loper, D. D. Lynch, and K. M. Stevenson, “Projected performance of smaller hemispherical resonator gyros,” in *PLANS '86 - Position Location and Navigation Symposium*, 1986, pp. 61–64.
- [13] J. Rosenberg, L. Qiang, and O. Painter, “Static and dynamic wavelength routing via the gradient optical force.” *Nature Photonics*, vol. 3, no. 8, pp. 478 – 483, 2009. [Online]. Available: <http://search.ebscohost.com.proxy.library.cornell.edu/login.aspx?direct=true&db=aph&AN=43471826&site=eds-live>
- [14] W. C. Hui, “How to prevent a runaway chemical reaction in the isotropic etching of silicon with hf/hno3/ch3cooh or hna solution,” in *Device and Process Technologies for MEMS, Microelectronics, and Photonics III*, vol. 5276, 2004, pp. 270–279. [Online]. Available: <http://dx.doi.org/10.1117/12.522944>
- [15] M. Madou, *Fundamentals of Microfabrication and Nanotechnology*. CRC Press, 2011. [Online]. Available: <http://books.google.com/books?id=yf47YAAACAAJ>
- [16] H. Hashimoto, S. Tanaka, K. Sato, I. Ishikawa, S. Kato, and N. Chubachi, “Chemical isotropic etching of single-crystal silicon for acoustic lens of scanning acoustic microscope,” *Japanese Journal of Applied Physics*, vol. 32, no. Part 1, No. 5B, pp. 2543–2546, 1993. [Online]. Available: <http://jjap.jsap.jp/link?JJAP/32/2543/>
- [17] M. Vangbo and Y. Bcklund, “Precise mask alignment to the crystallographic orientation of silicon wafers using wet anisotropic etching,” *Journal of Micromechanics and Microengineering*, vol. 6, no. 2, p. 279, 1996. [Online]. Available: <http://stacks.iop.org/0960-1317/6/i=2/a=011>
- [18] C. P. Ho, J. D. Plummer, J. D. Meindl, and B. E. Deal, “Thermal oxidation of heavily phosphorusdoped silicon,” *Journal of The Electrochemical*

- Society*, vol. 125, no. 4, pp. 665–671, 1978. [Online]. Available: <http://jes.ecsdl.org/content/125/4/665.abstract>
- [19] D. Armani, T. Kippenberg, S. Spillane, and K. Vahala, “Ultra-high-q toroid microcavity on a chip,” *Nature Letter*, vol. 421, pp. 925–928, 2003. [Online]. Available: <http://dx.doi.org/10.1038/nature01371>
- [20] C. Hwang, “Some experiments on the vibration of a hemispherical shell,” *Journal of Applied Mechanics*, vol. 33, pp. 817–824, 1966. [Online]. Available: <http://dx.doi.org/10.1115/1.3625188>
- [21] L. Sorenson, P. Shao, and F. Ayazi, “Effect of thickness anisotropy on degenerate modes in oxide micro-hemispherical shell resonators,” in *Micro Electro Mechanical Systems (MEMS), 2013 IEEE 26th International Conference on*, 2013, pp. 169–172.
- [22] F. I. Niordson, “The spectrum of free vibrations of a thin elastic spherical shell,” *International Journal of Solids and Structures*, vol. 24, no. 9, pp. 947 – 961, 1988. [Online]. Available: <http://www.sciencedirect.com/science/article/pii/0020768388900431>
- [23] P. Steeneken, J. Ruigrok, S. Kang, J. van Beek, J. Bontemps, and J. Koning, “Parameter extraction and support-loss in mems resonators,” *Proceedings Comsol conference 2007, Grenoble*, p. 725, 2007, arXiv:1304.7953v1.
- [24] E. Yilmaz and D. Bindel, “Effects of imperfections on solid-wave gyroscope dynamics,” in *IEEE Sensors 2013, Baltimore, MD.*, Nov 2013.
- [25] J. C. Knight, G. Cheung, F. Jacques, and T. A. Birks, “Phase-matched excitation of whispering-gallery-mode resonances by a fiber taper,” *Opt. Lett.*, vol. 22, no. 15, pp. 1129–1131, Aug 1997. [Online]. Available: <http://ol.osa.org/abstract.cfm?URI=ol-22-15-1129>
- [26] C. P. Michael, M. Borselli, T. J. Johnson, C. Chrystal, and O. Painter, “An optical fiber-taper probe for wafer-scale microphotonic device characterization,” *Opt. Express*, vol. 15, no. 8, pp. 4745–4752, Apr 2007. [Online]. Available: <http://www.opticsexpress.org/abstract.cfm?URI=oe-15-8-4745>
- [27] J. M. Feliz-Teixeira, “Apparently Deriving Fictitious Forces,” University of Porto, Department of Physics/Engineering, Tech. Rep., June 2011. [Online]. Available: http://paginas.fe.up.pt/~feliz/e-paper31_deriving-fictitious-forces-revised.pdf

- [28] M. L. Povinelli, M. Loncar, M. Ibanescu, E. J. Smythe, S. G. Johnson, F. Capasso, and J. D. Joannopoulos, "Evanescent-wave bonding between optical waveguides," *Opt. Lett.*, vol. 30, no. 22, pp. 3042–3044, Nov 2005. [Online]. Available: <http://ol.osa.org/abstract.cfm?URI=ol-30-22-3042>